Summer 2017

Biomedical applications of mesoporous silica particles

Cicily J. Ronhovde
University of Iowa

BIOMEDICAL APPLICATIONS OF MESOPOROUS SILICA PARTICLES

by
Cicily J. Ronhovde

A thesis submitted in partial fulfillment
of the requirements for
the Doctor of Philosophy degree in Chemistry
in the Graduate College of
The University of Iowa

August 2017

Thesis Supervisor: Professor Sarah C. Larsen

Graduate College
The University of Iowa
Iowa City, Iowa

CERTIFICATE OF APPROVAL

PH.D. THESIS

This is to certify that the Ph.D. thesis of

Cicily J. Ronhovde

has been approved by the Examining Committee for the thesis requirement
for the Doctor of Philosophy degree in Chemistry
at the August 2017 graduation.

Thesis Committee: _____
Sarah C. Larsen, Thesis Supervisor

_____
M. Lei Geng

_____
Gary W. Small

_____
Johna Leddy

_____
Aliasger K. Salem

I dedicate this work to my family, by blood and choice, for their support and encouragement throughout my doctoral journey.

"You may encounter many defeats, but you must not be defeated. In fact, it may be necessary to encounter the defeats, so you can know who you are, what you can rise from, how you can still come out of it."

-Maya Angelou

"One mind can think only of its own questions; it rarely surprises itself."

-Orson Scott Card, *Ender's Shadow*

ACKNOWLEDGEMENTS

I have been very fortunate in the relationships and collaborations that have contributed to the work presented in this thesis. Foremost, I would like to thank my thesis supervisor, Professor Sarah Larsen, for her guidance toward the completion of my degree as well as career preparation. By encouraging my involvement in mentorship, you facilitated a safe space for me to explore and develop my teaching skills. Thank you for persuading me to step outside of my comfort zone and take on that first research mentoring role. The research-adjacent opportunities you've urged me to pursue have been invaluable to my growth as an educator far beyond the classroom.

I would like to acknowledge Professor Lei Geng for the scientific training I received under his direction. I gained a love spectroscopy from you, and you taught me a great deal about careful experimental design and critical scientific assessment of results. The process was sometimes painful, but the outcome was always beneficial. Thank you also for your staunch support through a difficult time in my graduate journey.

I would also like to thank a number of my peers who aided me in my research and provided friendship and advice. I am grateful to former and current members of the Dr. Lei Geng Research Group – Claudiu Brumaru, Yan Hu, and Rachel Seuer – and the Dr. Sarah Larsen Research Group – Paul Mueller, Shani Egodawatte, Majid Nada, Alaa Al Minshid, and Sanjaya Jayalath. Special thanks to Angie Morris Thorn for her collaboration on the toxicity studies and to Sean Lehman for being a sounding board for both professional and personal topics. Additionally, I would like to thank the undergraduate and high school researchers whom I had the great privilege to mentor,

John Baer, Kasey Coleman, Maria Castro, Hunter Thompson, and Jesse Gray. I truly appreciate all of your enthusiasm for chemistry and your contribution to this research.

Finally, I would like to extend my deepest gratitude to a number of faculty and staff in the Chemistry Department for their varied assistance and support. Janet, Sharon, and Lindsay, I came to you with questions on a wide range of topics, and even if you didn't have the answer at your fingertips, you were always willing to search it out for me. To the instructors for whom I was a teaching assistant, particularly Assistant Professor Scott Shaw and Associate Professor Betsy Stone, I am grateful for the example you provided as teachers and as teaching mentors. And to the teaching laboratory support staff, Brian Morrison and Deb Williard, thank you so much for your practical and personal encouragement when I was frustrated.

From the very bottom of my heart, thank you all.

ABSTRACT

Mesoporous silica particles are of significant interest for biomedical applications due to their good general biocompatibility compared to other nanoparticle matrices such as quantum dots, high specific surface areas up to 1000 m^2/g, and extreme synthetic tunability in terms of particle size, pore size and topology, core material, and surface functionalization. For one application, drug delivery, mesoporous silica nanoparticles (MSNs) of two pore structures, MCM-41 – parallel, hexagonally ordered pores approximately 3 nm in diameter – and wormhole (WO) – interconnected, disordered pores also approximately 3 nm in diameter – were synthesized with particle diameters under 100 nm. Additionally, a magnetic Fe_3O_4 nanoparticle core was incorporated into Fe_3O_4-core WO-MS-shell particles. The particles were loaded with doxorubicin, a chemotherapeutic, and the drug release into phosphate buffered saline (PBS, 10 mM, pH 7.4) at 37 °C was monitored by fluorescence spectroscopy. The data were fit to three models: Korsmeyer-Peppas, first order exponential release, and Weibull. The Korsmeyer-Peppas model provided useful information concerning the kinetics and mechanism of drug release from each MSN type. A small but statistically significant difference in the release kinetics was found due to the different pore topologies. A much larger kinetic effect was observed due to the inclusion of an iron oxide core. Applying a static magnetic field to the Fe_3O_4-core WO-MS shell particles did not have a significant impact on the doxorubicin release. This is the first time that the effects of pore topology and iron oxide core have been isolated from pore diameter and particle size for these materials.

In vitro cell studies were conducted to determine the cytotoxicity of the bare and doxorubicin-loaded materials against three cancerous cell lines – A549 human lung carcinoma cells, HEC50CO human endometrial cancer cells, and CT26 mouse colon cancer cells. The MCM-41 and WO MSNs generally displayed similar toxicities within each cell line, and the Fe_3O_4-core WO-MS shell particles were less toxic. Doxorubicin-loaded particles generally displayed greater toxicity than bare MSNs, but the A549 cells were very resistant to all concentrations of MSNs tested.

For another biomedical application, tissue phantom development, mesoporous silica particles with approximately 10 µm diameters and C_{18} surface functionalization were evaluated for their use as a substrate for optical tissue phantoms. Tissue phantoms are synthetic imitations of biological material, and C_{18}-modified silica provides a substrate that is simple to load with optically active biological molecules. The molecules are then hydrophobically trapped to maintain a clear optical boundary between the biological loading within the particle and an aqueous suspension gel. Several preparation techniques were evaluated for the dispersal of hydrophobic particles in aqueous media, and qualitative analysis indicated that surfactant coating of the outer surface could fully disperse the hydrophobic particle while maintaining the clear optical boundary. A novel analysis was developed to provide a single numerical indicator of clustering for a quantitative assessment of particle dispersal in tissue phantoms.

PUBLIC ABSTRACT

Mesoporous silica (MS) is composed of silicon and oxygen and has pores between 2 and 50 nanometers and large surface-area-to-volume ratios. MS particles can be synthesized relatively easily with a variety of pore structures and chemical surface modifications allowing researchers to tailor these particles to a specific purpose.

Mesoporous silica nanoparticles (MSNs) have diameters smaller than a few hundred nanometers and have many useful properties – including biocompatibility and small size – that make them ideal for drug delivery, the transportation of a drug to reduce side effects. Doxorubicin is an anti-cancer drug that, among other side effects, has a high risk of heart damage. MSNs of two pore structures – MCM-41: straight, parallel pores, and WO: interconnected, disordered pores – were synthesized. These MSNs were loaded with doxorubicin, and the release into a buffer simulating physiological conditions was measured to determine the effect of the pore structure. These studies are crucial to finding the ideal architecture to optimize drug delivery.

MS particles were also used generate tissue phantoms, synthetic materials that mimic the properties of biological tissue for developing new diagnostic techniques. For spectroscopic tissue phantoms, MS particles with 10 nm pores, 10 µm diameters, and a hydrophobic coating were used to encapsulate fluorescent molecules. However, when suspended in water-based agar, the particles aggregated. Various dispersal methods were attempted. One method, which coated the particles' outer surface with soap molecules, allowed easy dispersal of particles. A new analysis was developed to assign a value between 0 and 1 to the particle dispersal.

TABLE OF CONTENTS

LIST OF TABLES

LIST OF FIGURES

CHAPTER 1: INTRODUCTION AND BACKGROUND

1.1. Mesoporous Silica Nanoparticles

1.1.1. Silica

Silicon and oxygen are the two most abundant elements in the earth's crust and are frequently found bonded in the form of silicon dioxide (SiO_2) also known as silica. Silica is composed of an extended, interconnected network of silicon atoms covalently bonded with four oxygen atoms in a tetrahedral arrangement [1]. The SiO_2 network can develop in a crystalline arrangement to form a material such as quartz or an amorphous arrangement in a material such as glass (Figure 1-1).

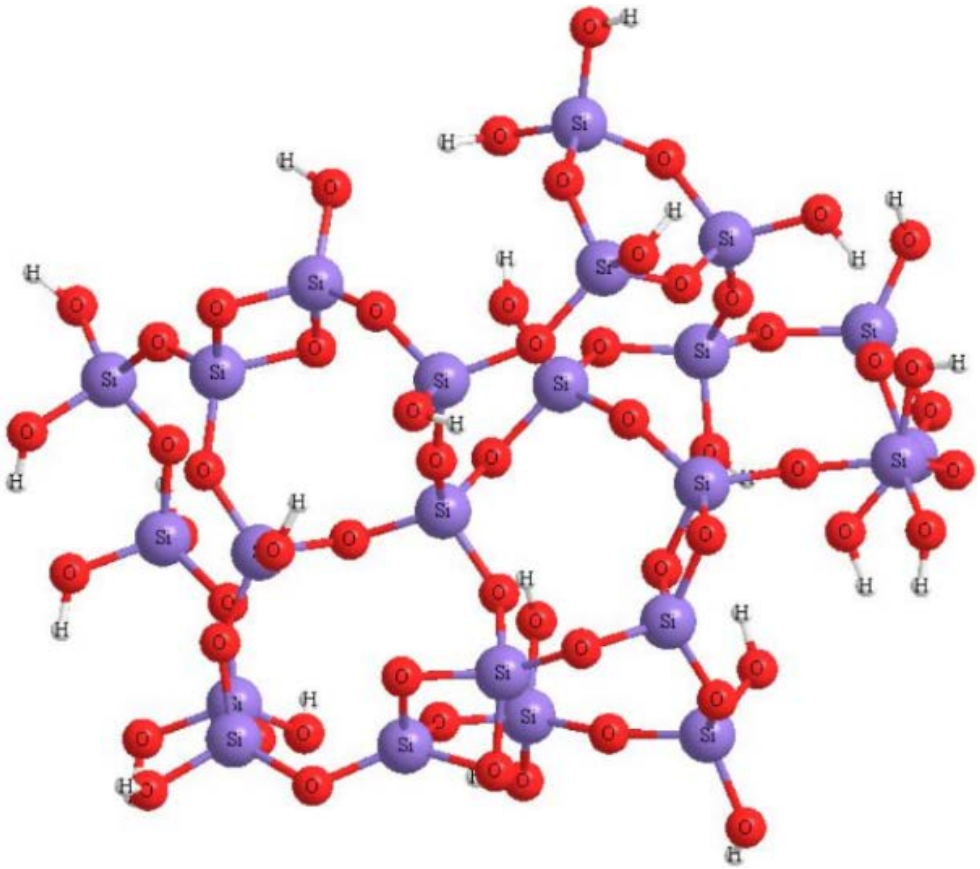

Figure 1-1. Ball and stick model of silica in an amorphous arrangement.

1.1.2. Silica Nanoparticles

Amorphous silica can be synthesized as spheres on the nanometer scale via a base-catalyzed sol-gel process, a bottom-up approach developed nearly 50 years ago [2]. This synthesis method utilizes an organosilane precursor – such as tetramethylorthosilicate (TMOS) or tetraethylorthosilicate (TEOS), represented as $Si(OR)_4$ where R represents either a methyl (CH_3) or ethyl (CH_2CH_3) moiety – which undergoes hydrolysis and condensation reactions:

$$\text{Hydrolysis: } Si(OR)_{4(aq)} + 2H_2O_{(l)} \rightarrow Si(OH)_{4(aq)} + 4R\text{-}OH_{(l)}$$

$$\text{Condensation: } (HO)_3Si\text{-}OH_{(aq)} + HO\text{-}Si(OH)_{3(aq)} \rightarrow (HO)_3Si\text{-}O\text{-}Si(OH)_{3(sol)} + H_2O_{(l)}$$

The initial condensation of two hydrolyzed organosilane molecules nucleates the formation of small colloidal particles, a state termed the "sol" phase. These colloidal particles continue to condense into discrete, solid particles, termed the "gel" phase. Control over the diameter of the resulting particles is achieved via a combination of the concentration of the organosilane – the thermodynamic component – and the concentration of the base catalyst – the kinetic component. In general, this sol-gel method produces highly homogeneous particle diameters with lower base-to-organosilane concentration ratios resulting in smaller particles.

1.1.3. Mesoporous Silica

In addition to the formation of solid particles, silica particles can also be synthesized in a variety of porous structures. Mesopores, defined as pores with diameters between 2 and 50 nm, are formed by directing the condensation of the silica source around a template (Figure 1-2). The template is composed of micelles of a

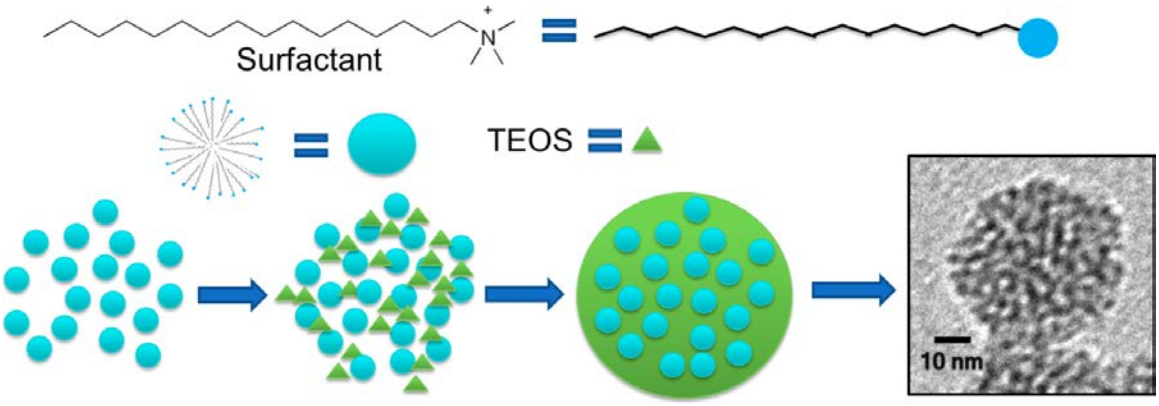

Figure 1-2. Schematic detailing the formation of cetyltrimethylammonium bromide (CTAB) surfactant micelles, the condensation of the organosilane TEOS into a particle around the micelles, and a transmission electron microscopy image of a resulting mesoporous silica nanoparticle.

surfactant such as cetyltrimethylammonium bromide (CTAB). Although the mechanism is not completely understood, in this process, surfactant molecules self-assemble into micelles. The identity and concentration of the surfactant determines the shape of the micelles – spherical or rod-like – as well as their association and orientation to one another – ordered or disordered. With the micelles in an equilibrium state, the silica condenses around the surfactant. After the particles have formed, the surfactant is removed via calcination or solvent extraction, and the mesoporous silica product is obtained.

1.1.4. Properties of Mesoporous Silica Nanoparticles (MSNs)

Mesoporous silica materials were first developed for catalytic applications around 25 years ago [3]. However, these materials have a number of advantageous properties for a diverse range of applications including healthcare and environmental remediation. Silica is generally stable and non-toxic, and the surface is easily functionalized with a wide variety of moieties. The silica surface has an abundance of

silanol groups (Si-OH), exhibiting between 4 and 5 Si-OH units/nm^2 [4]. The surface silanols sample a variety of environments leading to a range of pKa values between approximately 2.5 and 6.5 [5], and the deprotonated silanol ($Si-O^-$) contains a highly nucleophilic oxygen. Therefore, nearly any desired functional group X can be covalently bonded to the surface through the reaction of surface silanols with a trialkoxysilane molecule ($X-Si-(OR)_3$). This surface functionalization can be used to optimize the surface interactions to the desired application or to mitigate unfavorable interactions. Additionally, the silica surface can be covalently modified with a wide range of biomolecules – including proteins, such as enzymes or antibodies, polysaccharides, and nucleic acids – to facilitate specific biological reactions or interactions.

Although non-porous silica can be functionalized, the porous nature of mesoporous silica provides a significant advancement. Essential to the efficiency of majority of applications is the extremely high specific surface areas, often greater than 1000 m^2/g, which translate to enhanced surface-mediated processes such as large adsorption capacities or expedited catalysis. Additionally, mesoporous silica encompasses a wide range of pore dimensions and topologies that are attainable through simple adjustments to the synthetic conditions. Adjustments to pore shape and size are particularly useful for tuning the release of an adsorbed molecule in an application such as drug delivery. The MSN pore topologies utilized in this thesis are MCM-41 and wormhole (WO). MCM-41 silica has parallel, hexagonally ordered pores and WO silica has disordered, interconnected pores. Both the MCM-41 and WO structures have approximately 3 nm pore diameters.

Another useful modification to MSNs is the incorporation of a metal oxide core such as magnetite (Fe_3O_4). Magnetite nanoparticles are superparamagnetic; they have no magnetic attraction between particles until an external magnetic field is applied. Synthetically, imbedding an Fe_3O_4 core is simple to achieve. Magnetite nanoparticles approximately 10 nm in diameter are suspended in the reaction mixture containing the surfactant micelle template. Upon addition of the organosilane precursor, silica condenses around both the Fe_3O_4 particles and the template [6]. These core-shell particles, denoted core@shell, e.g. Fe_3O_4@MS, integrate the features of the mesoporous silica shell with the magnetic property of the Fe_3O_4 core. This combination can be used in conjunction with a static magnetic field to direct or sequester the materials; or an oscillating magnetic field can be applied, inducing a vibration into the sample, which can be used to raise the temperature of the local environment and/or to stimulate the release of an adsorbate.

1.2. Drug Delivery Applications of MSNs

Beginning approximately 15 years ago with the first investigation of mesoporous silica nanoparticles for the adsorption and release of ibuprofen, interest in the use of MSNs as drug delivery system (DDS) substrates has emerged and increased enormously [7-9]. MSNs have been investigated for the delivery of a variety of drugs including non-steroidal anti-inflammatories such as ibuprofen and aspirin [10, 11], antibiotics such as vancomycin [12, 13], and chemotherapeutics such as doxorubicin and methotrexate [14, 15]. Due to the porosity, MSNs are able to encapsulate a drug molecule of interest which has a two-fold advantage. First, the loaded drug molecule is isolated from the

bloodstream which may protect it from enzymatic degradation prior to reaching the target site, enabling lower doses to be more efficacious [16]. Second, the encapsulation can prevent interactions of the therapeutic agent with non-target cells, reducing side effects that may occur from non-specific administration of a drug [17].

1.2.1. Drug Loading

The loading is generally achieved by soaking the MSNs in a solution of the drug to allow adsorption interactions between the drug and the particle surface. These interactions usually involve hydrogen bonding and electrostatic attractions. Often the surface is modified to enhance this interaction, particularly for drug molecules that are poorly water soluble [18-20]. Occasionally, drug loading is achieved via covalent attachment with the particle surface [21, 22]. Loading capacities are highly variable based on the particular drug and which surface functionalization, if any, is utilized. While modified surfaces and covalent attachment of the drug can result in loading levels up to several hundred milligrams per gram (mass of drug per mass of particle) [11, 23], drug loading on bare silica surfaces is often below 50 mg/g [19, 24, 25]. However, depending on the treatment of interest, the higher loading levels may not be necessary due to the increased therapeutic efficacy of DDSs.

1.2.2. Passive Targeting

Once a drug has been loaded into the DDS substrate, non-specific administration of the drug carrier into the bloodstream translates to specific treatment at the impacted site by targeting the drug carrier to the region of interest. If the drug carrier is quickly directed to and maintained at the target location, the highest concentration of drug

released will be in close proximity to, most significantly impact, that location. Accumulation of a drug delivery system is primarily a function of blood flow, a passive process, hence the term “passive targeting.” For tumorous cancers, passive targeting with nanoparticle drug delivery systems can be extremely effective because intravenous administration of a suspension of nanoparticle drug carriers will result in particle accumulation in neoplastic tissue [26]. This is due to the enhanced permeability and retention (EPR) of cancerous tissue; the interconnected vasculature and impaired circulation prevents blood flow from effecting the passive removal large molecules and nanoparticles from the tumor [27]. Passive targeting can be enhanced through the use of a magnetic DDS such as Fe_3O_4@MS via the application of a static magnetic field at the target site which attracts and retains magnetic DDSs [28-30].

1.2.3. Active Targeting

For non-localized ailments and treatment of drug-resistant diseases, passive targeting is augmented with active targeting in order to achieve cellular uptake of the DDS. Active targeting is achieved through modification of the DDS surface with target-specific ligands to tune the interaction with corresponding receptors expressed on the outer membrane of the target cells. Common targeting ligands include antibodies, amino acid chains, and nucleic acids. Due to the high metabolic rate, cancer cells express many receptors, e.g. epidermal growth factor receptor, at a higher rate than healthy cells [26]. Drug delivery carriers, then, can be modified with epidermal growth factor to target cancer cells. Upon interaction between the growth factor on the DDS and the receptor on the cancer cell membrane, the cell initiates receptor-mediated

endocytosis, internalizing the DDS [31]. A similar targeting scheme can be used for treatment of Gram negative bacterial infections with epsilon-poly-L-lysine functionalized MSNs [32]. Drug release from endocytosed DDSs is particularly effective because intracellular concentrations are much higher than can be achieved by drug diffusion across the cellular membrane [33].

1.2.4. Controlled Drug Release

During the targeting process, while a DDS circulates in the bloodstream, a variety of controlled release mechanisms can be employed to prevent premature release of the payload. The most basic form of release is to simply allow dissolution of the drug. This method of release is strongly dependent on the solubility of the drug. A hydrophilic drug molecule would dissolve rapidly in the bloodstream and the use of a drug delivery system may not provide an advantage over non-specific administration [16, 34]. However, this method could be useful for a hydrophobic drug molecule that would not dissolve until it came into contact with a non-polar environment. *In vitro* studies have shown that the phospholipids of a cellular membrane can induce release of hydrophobic drugs during the endocytosis of the drug carrier particle [35]. In the dissolution controlled delivery of drugs, particle geometry – size, shape, pore structure – is of primary consideration for possible impact on release kinetics. Cellular uptake is known to be impacted by particle size and shape [36, 37], as is the drug release profile [34, 38]. Additionally, pore structure has been shown to influence the release kinetics [23, 39]. Therefore, it is possible for dissolution-mediated drug delivery to be controlled primarily through particle structure.

The incorporation of a magnetic core provides additional formats for controlled drug release via stimuli response. The application of an oscillating magnetic field at radio frequencies (15-300 Hz) can stimulate the release of a loaded drug by inducing vibration of the particles [40, 41]. This method could be useful for effecting the release of low loading amounts or poorly soluble drugs. On the opposite end of the spectrum, the magnetic core can also facilitate the stimulated release of highly soluble drugs. The drug loaded into the magnetic DDS can be trapped in the pores either by pore capping with a thermal responsive tether such as double stranded DNA [42] or by a particle coating with a thermal degradable polymer such as poly(ethyleneimine)-b-poly(N-isopropylacrylamide) (PEI/NIPAM) [43, 44]. Upon application of an alternating magnetic field, the fast vibration of the core generates a localized heating effect; cap tether or polymer coating melts, opening the pore to solution and allowing release of the payload. Interestingly, due to the promoted release as a result of the core vibration, the drug released induced by the magnetic field is greater than that induced by a corresponding increase in ambient temperature [44].

1.2.5. Magnetic MSNs for Synergistic Therapy and Theranostics

Among the myriad advantages imparted by the inclusion of a magnetic core in an Fe_3O_4@MS drug delivery system is multi-functionality. In addition to the stimulating release of either hydrophobic or hydrophilic drugs, applying an alternating magnetic field can provide synergistic therapy. At oscillation frequencies in the hundreds of Hertz, the Fe_3O_4 cores not only generate heat – inducing hyperthermia at the target site [45] – but they also generate reactive oxygen species (ROS) [46], both of which induce cell

death. For antimicrobial or anticancer treatments, these additional avenues of killing cells confer a substantial enhancement in the overall treatment effectiveness [47].

Magnetic drug delivery platforms have also been investigated for theranostic applications, the combination of therapy and diagnostic medicine. Of particular interest is the contribution to medical imaging. Several studies have validated the use of Fe_3O_4@MS particles as contrast agents for magnetic resonance imaging [29, 48-51]. The Fe content of the core impacts the transverse relaxation rate ($1/T_2$) of tissue more than the longitudinal relaxation rate ($1/T_1$) leading to an increased image contrast on par with current commercial contrast agents. The theranostic combination of treatment and imaging can revolutionize cancer therapy by allowing for imaging-guided therapy [51].

1.3. Toxicity of Mesoporous Silica Nanoparticles

Because a fundamental motivation for drug delivery development is the reduction of side effects, the host matrix into which the drug is loaded must be evaluated for this potential. Given that the DDS is likely to be administered intravenously, non-specific interactions that occur while circulating in the bloodstream before it reaches the target site play a role in determining what side effects, if any, result. Additionally, specific interactions with the target cells determine the therapeutic efficacy. Many approaches are taken in order to assess the side effect potential and therapeutic efficacy of a DDS to evaluate its potential for continued development. The two most common approaches are *in vitro* cell studies to determine cytotoxicity and *in vivo* animal studies to gauge overall biocompatibility and specific immunotoxicity.

In vivo animal studies are often the best measure of general toxicity and determination of serious side effects. However, given the wide range of mesoporous silica nanoparticle synthesis procedures and the resulting physical characteristics, general statements about the toxicity of mesoporous silica as a class of materials are limited. Based on a compilation of studies of nanoparticles composed of inorganic materials, a few toxicity generalities can be linked to individual physical characteristics [52, 53].

It has been shown that particles with anionic surfaces (e.g. silica with deprotonated silanol groups) are generally less toxic than cationic gold and polystyrene nanoparticles, which cause hemolysis and blood clotting [17]. However, this general toxicity is highly dependent on application method. In mice, subcutaneous injection of colloidal mesoporous silica of 150 nm particle diameters and 3 nm pore diameters at doses as high as 1200 mg/kg produced no observable effect, but intraperitoneal and intravenous injections resulted in significant distress and death requiring doses to be lowered to 40 mg/kg for a non-fatal result [54]. Particle size also plays an important role. In immunological studies, mesoporous silica of particle diameters between 30 and 100 nm produced an inflammatory response in both mice and rat models for all applications methods, intradermal, intraperitoneal, and intravenous [55].

In vitro cells studies provide a narrower point of inquiry and provide additional refinement to the correlation between physical characteristics and toxicity. For example, the phase composition of the nanoparticle is highly indicative of cytotoxicity with crystalline silica (quartz) being more toxic than amorphous silica [53], nonporous

silica being more toxic than mesoporous silica [56], and bare silica being more toxic than amine-modified silica [34].

Cell studies are also useful to indicate therapeutic efficacy of the loaded DDS versus the free drug in solution. Because of the debilitating side effects of the majority of chemotherapeutics, the evaluation of DDS materials for cancer therapy is one of the largest areas of DDS research. In the evaluation of a new chemotherapeutic drug delivery material, a variety of cancerous cell lines are employed. Common cell lines include the A549 human lung cancer cell line, HeLa human cervical cancer, and MCF-7 human breast cancer cell line which also has a multiple-drug-resistant variation MCF-7/ADR.

MCM-41 particles with 100 nm diameters were evaluated for drug delivery of the cancer drug curcumin [57]. Results indicated significantly higher efficacy against both A549 and MCF-7 than the free drug while the loaded DDS was non-toxic to healthy CHO Chinese hamster ovary cells. In another study, Fe_3O_4@MS particles with 60 nm diameters were evaluated for drug delivery of the cancer drug doxorubicin [51]. While the DDS displayed significant dose dependent toxicity toward HeLa cells, healthy COS7 monkey kidney cells were relatively unaffected. The capability of overcoming drug resistance was demonstrated in a study of 180 nm diameter mesoporous silica particles loaded with doxorubicin [16]. Although this DDS had similar toxicity to free doxorubicin against the drug sensitive MCF-7 cell line, the cell viability of the drug-resistant MCF-7/ADR was significantly reduced by the drug-loaded DDS versus free doxorubicin. Cellular uptake of the DDS particles facilitates higher concentrations of the drug within

the cytoplasm than would generally be achieved via diffusion of the free drug across the cell membrane. The combination of generally low cytotoxicity against healthy cells and the corresponding high cytotoxicity against diseased cells make mesoporous silica nanoparticles of continued interest in the development of chemotherapeutic drug delivery systems.

1.4. Thesis Overview

The work described in this thesis was focused on two areas: drug delivery with mesoporous silica nanoparticles and hydrophobic mesoporous silica particles for tissue phantom construction. The uniting point is the use of mesoporous silica for biomedical applications. Chapter 1 describes the fundamental characteristics of mesoporous silica. Chapter 1 also gives an overview of the use of mesoporous silica nanoparticles in drug delivery including loading, targeting, and controlled release. Additionally, the application of core-shell particles to medical therapy and diagnostics is described. Finally, Chapter 1 provides a short summary of the toxicity of mesoporous silica nanoparticles.

Chapter 2 describes the synthesis of sub-100 nm mesoporous silica nanoparticles of two pore topologies, MCM-41 and WO, and the incorporation of an Fe_3O_4 nanoparticle core into particles of each pore structure. The characterization of the particles to determine size and shape as well as surface area, pore diameter, and pore volume is described. Chapter 3 describes the evaluation of three synthesized MSNs, MCM-41, WO, and Fe_3O_4@WO for the drug delivery of doxorubicin. The assessment of the degradation of doxorubicin under the experimental conditions was crucial

determining a model with which to fit the data to retrieve kinetic and mechanistic information. The effect of pore topology and presence of an iron oxide core are discussed. Chapter 4 described the cytotoxicity studies of the three MSNs – both bare and loaded with doxorubicin – against three cancerous cell lines. These studies are used to provide a general idea of biocompatibility of the bare MSN and therapeutic efficacy of the drug-loaded MSN.

Chapter 5 describes the use of hydrophobic, C_{18}-modified, mesoporous silica particles for fluorescent tissue phantoms. Several methods were attempted to disperse the hydrophobic particles in aqueous media. Confocal fluorescence microscopy was used to evaluate the incorporation of particles into the phantom body and observe clustering. Chapter 6 describes the quantitative analysis of the tissue phantom images tracing the development of a single numerical indicator of clustering based on the pair correlation function. The developed metric is contrasted with a simpler, but less powerful method of cluster analysis.

Chapter 7 provides a summary of the results of the studies described in the thesis along with some potential avenues of inquiry based on the results within the current status of the research field.

CHAPTER 2: SYNTHESIS AND CHARACTERIZATION OF MESOPOROUS SILICA MATERIALS

2.1. Structures of Mesoporous Silica Nanoparticles for Biomedical Applications

Mesoporous silica nanoparticles (MSNs) have a number of advantageous physical characteristics which make them attractive for biomedical applications. These properties include tunable pore sizes between 2 – 50 nm diameters, synthetic control over a variety of structures and surface functionalizations, large specific surface areas (≥ 1000 m^2/g), and very good biocompatibility compared to many other possible solid matrices such as quantum dots [58]. Specifically for drug delivery applications, synthetic tunability of MSNs permits the optimization of particle-drug pairings to improve the effectiveness and reduce side effects of a chosen drug. Two common and easily synthesized pore structures, Mobil Crystalline Material 41 (MCM-41) and "wormhole" (WO) mesoporous silica, were utilized in this research study. MCM-41 silica has parallel, hexagonally ordered pores approximately 3 nm in diameter and WO silica has disordered, interconnected pores with a similar 3 nm pore diameter.

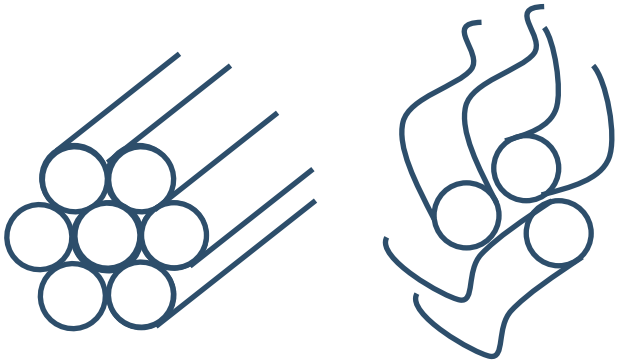

Figure 2-1. Schematic representations of MCM-41 pore structure (left) and WO pore structure (right).

Additionally, a magnetic nanoparticle Fe_3O_4 core may be incorporated into the MSN structure, which can allow magnetic direction of the location of the drug carrier – and therefore, the drug – to a target area within the body. A magnetic core could also impart multi-functionality to the particles, allowing for their use as a contrast agent for magnetic resonance imaging [51, 59], or to enhance treatment at the target site by stimulating drug release or inducing hyperthermia as a result of radio frequency heating [44, 45].

Particle accumulation inside target cells is essential to drug delivery and other theranostic applications. Several studies have shown that the cellular uptake of MSNs tends to be higher for sub-100 nm particles than for larger particles [19, 27, 36, 37, 60, 61]. Many of these studies indicate a "sweet spot" for cellular uptake of MSNs with particle diameters around 50 nm. Thus, the target size of the particles synthesized for this study was 50 nm. By necessity, the inclusion of Fe_3O_4 cores into the MSNs increases the particle size. However, sub-100 nm core-shell particles can still be achieved. In this study, a series of MSNs with pore diameters of 3 nm and sub-100 nm particle sizes were synthesized with and without an iron oxide core.

2.2. Synthesis of MSNs

MSNs are synthesized by condensation of a silica source such as tetraethylorthosilicate (TEOS) in the presence of micellar concentrations of a surfactant, typically cetyltrimethylammonium bromide (CTAB). The micelles form a template around which the silica condenses. After particle condensation, the surfactant template is removed via solvent extraction or high temperature calcination to leave the porous

silica material. In MSN particle synthesis, it is well established that the relative concentrations of the silica precursor TEOS and base (NaOH) contribute to resulting particle size; specifically, decreasing relative concentration of base results in smaller particles [19]. Additionally, the inclusion of a small organic amine such as trienthanolamine (TEA) can be incorporated to further reduce particle size [6]. In order to achieve, sub-100 nm particle sizes, the concentrations of TEOS and NaOH as well as the inclusion of TEA were systematically varied until the resulting particles matched expectations. A final component of the synthesis, the surfactant used as the pore template, was rigorously maintained as constant because both the identity and concentration of the surfactant influence the resulting pore structure [62].

2.2.1. Synthesis of MCM-41 MSNs

MCM-41 silica nanoparticles with approximately 50 nm diameters were synthesized by dissolving 0.5 g cetyltrimethylammonium bromide (CTAB) and 110 mg NaOH in 250 mL Millipore water (18.2 MΩ cm). The solution was stirred at room temperature for 2 hours, then 375 uL of triethanolamine (TEA) was added. Immediately after adding the TEA, the solution was heated to 80 °C, and, while stirring, 2.5 mL of tetraethylorthosilicate (TEOS) was added. The reaction was allowed to proceed at 80 °C for 2 hours. The suspension was cooled, the material separated by centrifugation, and washed in triplicate with water. The samples were dried overnight, then the template was removed by calcination in air at 600 °C for 6 hours. The relative amounts of TEOS and NaOH were varied to control particle size. The range of synthesis conditions attempted by varying the amounts of NaOH and TEOS is shown in Table 2-1.

Table 2-1. Synthesis reactant conditions indicated as molar ratios. Asterisk (*) indicates the sample for which the synthesis conditions are described. Dagger (†) indicates synthesis a double-scale synthesis.

Sample	TEOS/CTAB	TEOS/NaOH	TEOS/TEA
MCM-41-A*	8.2	4.2	4.0
MCM-41-B	8.2	4.5	4.0
MCM-41-C	8.2	5.0	4.0
MCM-41-D	8.2	5.2	4.0
MCM-41-E	8.2	5.6	4.0
MCM-41-F	8.2	6.1	4.0
MCM-41-G	12.2	6.3	5.9
MCM-41-H	9.8	5.1	4.8
MCM-41-I	7.3	3.8	3.6
MCM-41-J	6.5	3.4	3.2
MCM-41-K†	8.2	4.2	4.0

2.2.2. Synthesis of WO MSNs

Wormhole silica nanoparticles with approximately 50 nm diameters were provided by Paul Mueller, PhD. WO particles were synthesized according to a previously described procedure [63]. In brief, 50 mL 25% aqueous cetyltrimethylammonium chloride (CTAC), 50 mL absolute ethanol, and 300 mL Millipore water (18.2 MΩ cm) were stirred for 10 minutes at room temperature. Triethanolamine (20 mL, TEA) was added, and the solution was stirred at room temperature for one hour. The solution was then heated to 60 °C. While stirring, 30 mL of tetraethylorthosilicate (TEOS) was added at a rate of about 2 mL/minute and the reaction was allowed to proceed at 60 °C for 2.5 hours. The suspension was cooled, the material separated by centrifugation, and washed in triplicate with water. The samples were dried overnight and then calcined in air at 600 °C for 6 hours.

2.2.3. Synthesis of Magnetic Fe_3O_4@WO (mWO) MSNs

Fe_3O_4@WO nanoparticles with approximately 75 nm diameters were synthesized according to a 1-pot procedure described previously [6]. Briefly, 200 mL Millipore water (18.2 MΩ cm) was purged with nitrogen gas for 30 minutes. $FeCl_2 \cdot 4H_2O$ (0.17 g) and $FeCl_3 \cdot 6H_2O$ (0.27 g) were dissolved while continuing to purge the solution. After the iron salts were completely dissolved, 900 uL concentrated NH_3 (29%) was added, and the mixture was allowed to continue purging for 30 minutes. An aqueous solution of CTAC (25%, 16 mL) was added, and the suspension was mixed for an additional 15 minutes. Under mechanical stirring at 500 rpm, the mixture was heated to 60 °C and 4.0 mL TEOS was added. The reaction was allowed to proceed at 60 °C for 2 hours. The suspension was cooled, the material separated by centrifugation, and washed in triplicate with water. The material was suspended in ethanol and magnetically separated. The samples were dried overnight then calcined in air at 600 °C for 6 hours.

2.2.4. Synthesis of Magnetic Fe_3O_4@MCM-41 (mMCM-41) MSNs

Fe_3O_4 nanoparticles with approximately 10 nm diameters were synthesized according to a previously published procedure [64]. Briefly, 30 mL Millipore water (18.2 MΩ cm) water was purged with nitrogen gas for 30 minutes. $FeCl_2 \cdot 4H_2O$ (3.0 g) and $FeCl_3 \cdot 6H_2O$ (7.2 g) were dissolved while continuing to purge the solution. After the iron salts were completely dissolved, the reaction was heated to 80 °C while maintaining N_2 atmosphere. Aqueous NH_3 (29%, 15 mL) was added to raise the pH to 10. Immediately upon addition of the NH_3, Fe_3O_4 condensed out of solution as a black precipitate. The particles were aged 2.5 hours at 80 °C. The suspension was cooled, and the material was

separated by centrifugation. The precipitate was washed with water and ethanol and dried for 48 hours at 80 °C to obtain Fe_3O_4 powder.

The Fe_3O_4 cores were coated with MCM-41 silica according to a previously published procedure [40]. Briefly, Fe_3O_4 cores (625 µg/mL) were sonicated in an aqueous solution of cetyltrimethylammonium bromide (CTAB, 11.5 mM) and sodium hydroxide (NaOH). Under mechanical stirring at 500 rpm, the suspension was heated to 80 °C and TEOS was added. The reaction was allowed to proceed at 60 °C for 2 hours. The suspension was cooled, the material separated by centrifugation, and washed in triplicate with water. The material was suspended in ethanol and magnetically separated. The samples were dried overnight then calcined in air at 600 °C for 6 hours. The range of synthesis conditions attempted by varying the sonication time and concentrations of NaOH and TEOS is shown in Table 2-2.

Table 2-2. Synthesis reactant conditions indicated as molar ratios. Asterisk (*) indicates literature conditions. Dagger (†) indicates a 2/3-scale synthesis.

Sample	Sonication time (min)	TEOS/CTAB	TEOS/NaOH
mMCM-41-A*	30	8.2	3.2
mMCM-41-B	120	8.2	3.2
mMCM-41-C†	120	8.2	3.2
mMCM-41-D	120	8.2	4.7
mMCM-41-E	30	4.1	1.6
mMCM-41-F	30	5.2	2.6
mMCM-41-G	30	6.5	2.6
mMCM-41-H	120	6.5	2.6

2.3. Characterization of Nanomaterials

Silica nanomaterials were characterized using electron microscopy and nitrogen adsorption isotherms. TEM images were acquired using a JEOL JEM-1230 transmission

electron microscope. Nitrogen adsorption experiments were conducted using a Nova 1200 Nitrogen Adsorption Instrument (Quantachrome). Approximately 100 mg of particle was dried at 120 °C under vacuum overnight. A seven-point BET isotherm and a 50-point adsorption/desorption isotherm in a liquid nitrogen bath were obtained using pure nitrogen gas as the adsorbate. Surface area was calculated using BET (Brunauer–Emmett–Teller) method using the seven-point BET isotherm. Pore diameter and volume were calculated using BJH (Barrett–Joyner–Halenda) method, using the desorption portion of the 50-point isotherm.

2.4. Results and Discussion

Synthesis of MCM-41 MSNs was achieved via a range of synthesis conditions. Due to the 50 nm desired particle diameters, the highly ordered MCM-41 pore structure was difficult to attain. Because the absolute concentration of surfactant is the primary condition used to control the formation of the template and the resulting pore structure, the concentration of CTAB was maintained constant across all trials. The initial synthesis conditions (Table 2-1, Sample MCM-41-D) resulted in average particle diameters of approximately 100 nm with 40% relative standard deviation in the size (Figure 2-1A). These particles were larger than desired, particle shapes were not spherical, and the polydispersity of particle sizes was unfavorable. Additionally, while the porosity can be clearly seen, the characteristic striations or hexagonal pattern of the MCM-41 topology is absent. Several variations of the synthesis conditions produced large, non-spherical particles and poor MCM-41 structure. While lowering the

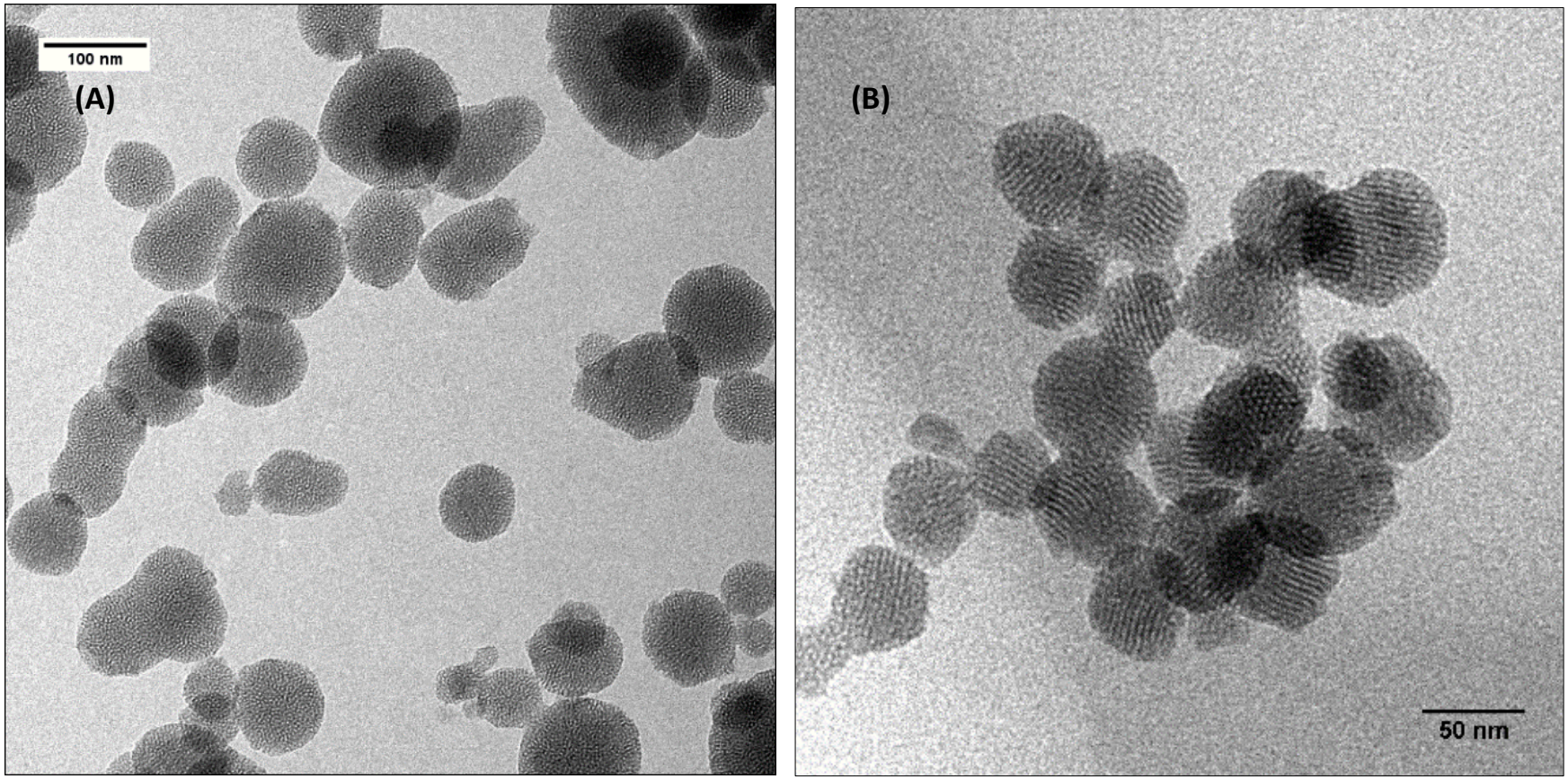

Figure 2-2. TEM images of (A) MCM-41-D showing particle sizes of 103 nm (± 42%) and (B) MCM-41-A showing particle sizes of 52 nm (± 23%). Error indicates relative standard deviation of 50 particles measured from multiple images.

concentration of TEOS (MCM-41-G through -J) did not improve the results, lowering the concentration of NaOH produced samples with smaller particle sizes (MCM-41-A through -C). Of particular interest for further use, synthesis conditions for MCM-41-A resulted in particles approximately 50 nm in diameter with a much more consistent 23% relative standard deviation (Figure 2-2B). The image of MCM-41-A also displays the distinctive striations indicative of ordered, parallel pore topology of MCM-41.

WO MSNs with approximately 50 nm diameters were characterized as provided. The TEM image (Figure 2-3) shows particle dimensions in the desired size range and distribution, 45 (± 22%). Additionally, the particle morphologies are approximately spherical and the variegated appearance of the pores indicates the wormhole topology. An additional sample of WO-MSN with a particle diameter of 78 nm and an iron oxide core (Fe_3O_4@WO) was prepared. A TEM image Fe_3O_4@WO MSNs is presented in Figure 2-4. The dark spots at the centers of the particles show the incorporation of Fe_3O_4.

The synthesis of Fe_3O_4@MCM-41 MSNs with particle diameters below 100 nm was attempted via a variety of synthetic conditions. Literature conditions produced oblong particles with large aggregates of Fe_3O_4 incorporated near the surface of the particle (Figure 2-5). Systematically increasing the sonication time to disperse Fe_3O_4 aggregates and reducing the TEOS/NaOH concentration ratio produced particles that were more spherical in shape and had smaller diameters (Figure 2-6). Additionally, the Fe_3O_4 nanoparticles were incorporated as smaller aggregates near the center of the particles. However, a sufficiently small sample of Fe_3O_4@MCM-41 MSNs has not yet

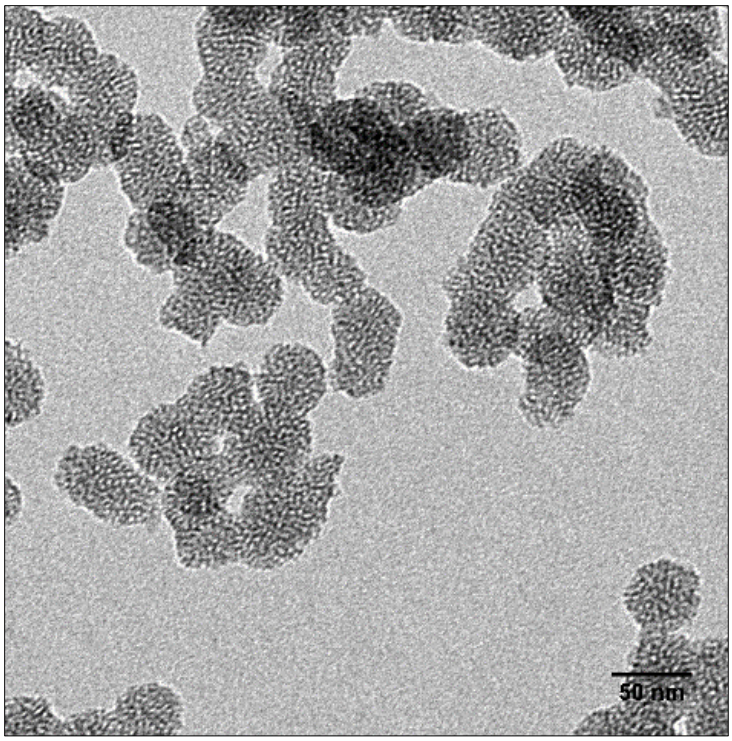

Figure 2-3. TEM image of WO MSNs synthesized by Paul Mueller, PhD, showing particle sizes of 45 nm (± 22%). Error indicates relative standard deviation of 50 particles measured from multiple images.

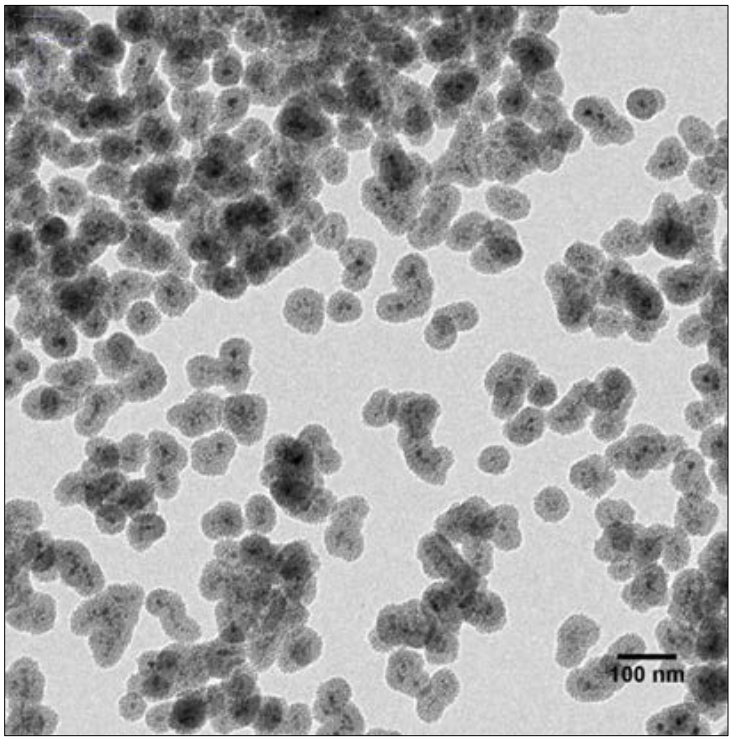

Figure 2-4. TEM image of mWO MSNs showing particle sizes of 78 nm (± 28%). Error indicates relative standard deviation of 50 particles measured from multiple images.

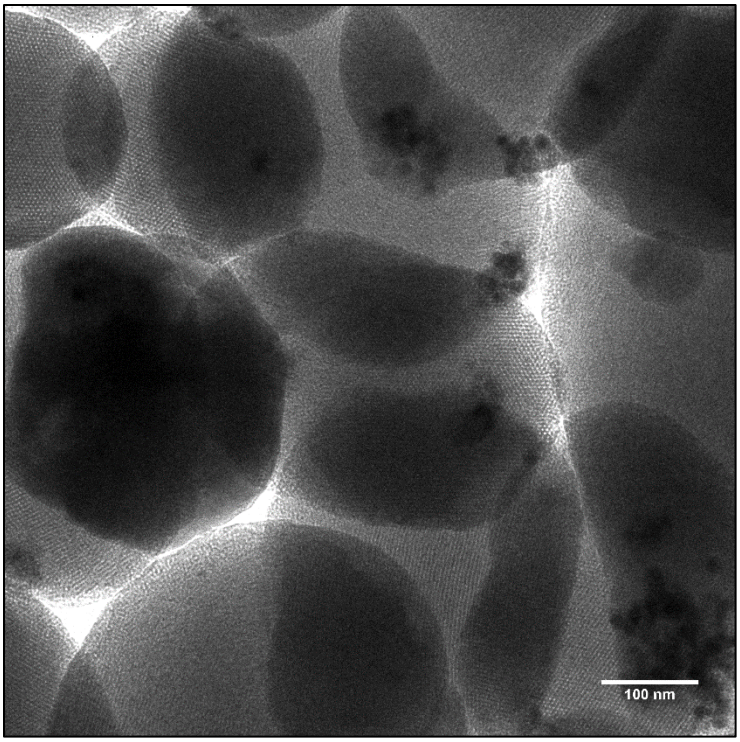

Figure 2-5. TEM image of mMCM-41-A MSNs showing Fe_3O_4 aggregates incorporated at the edges of oblong particles much larger than 100 nm in diameter.

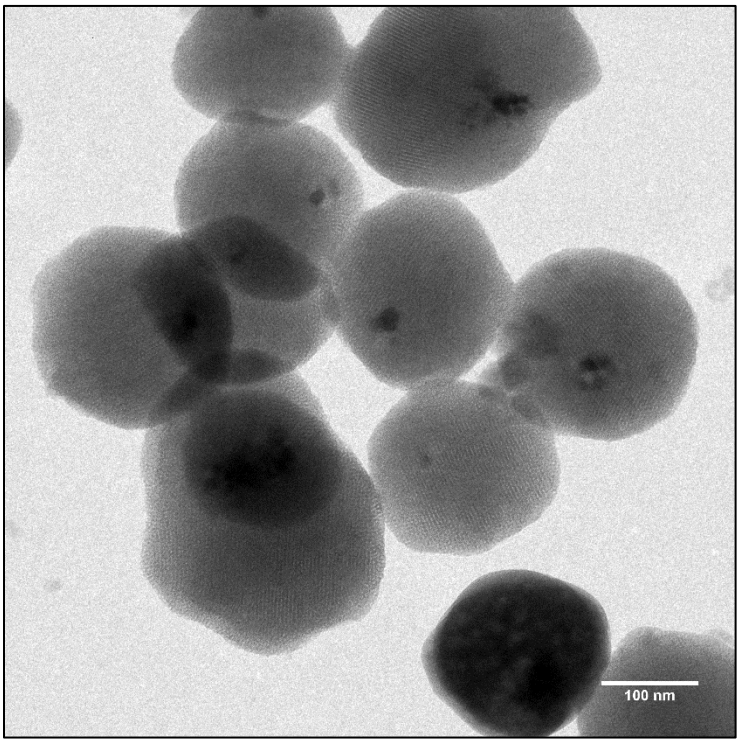

Figure 2-6. TEM image of mMCM-41-H MSNs showing smaller, more centrally located Fe_3O_4 aggregates incorporated into rounder particles slightly larger than 100 nm in diameter.

been synthesized. The MSNs chosen for subsequent use in the drug delivery studies (50 nm MCM-41 and WO and 75 nm mWO) are listed in Table 2-3.

The nitrogen adsorption-desorption isotherms (Figure 2-7) show the hysteresis at the relative pressure (P/P_0) of 0.3-0.5 typical of MSNs with pore diameters approximately 3 nm. The surface areas of MCM-41 and WO are 1016 and 944 m^2/g, respectively, with the mWO surface area reduced relative to the parent material to 615 m^2/g. This reduction of surface area with the incorporation of a solid (non-porous) nanoparticle core is typical of what has been observed previously [64, 65]. The results of the characterization studies are summarized in Table 2-3.

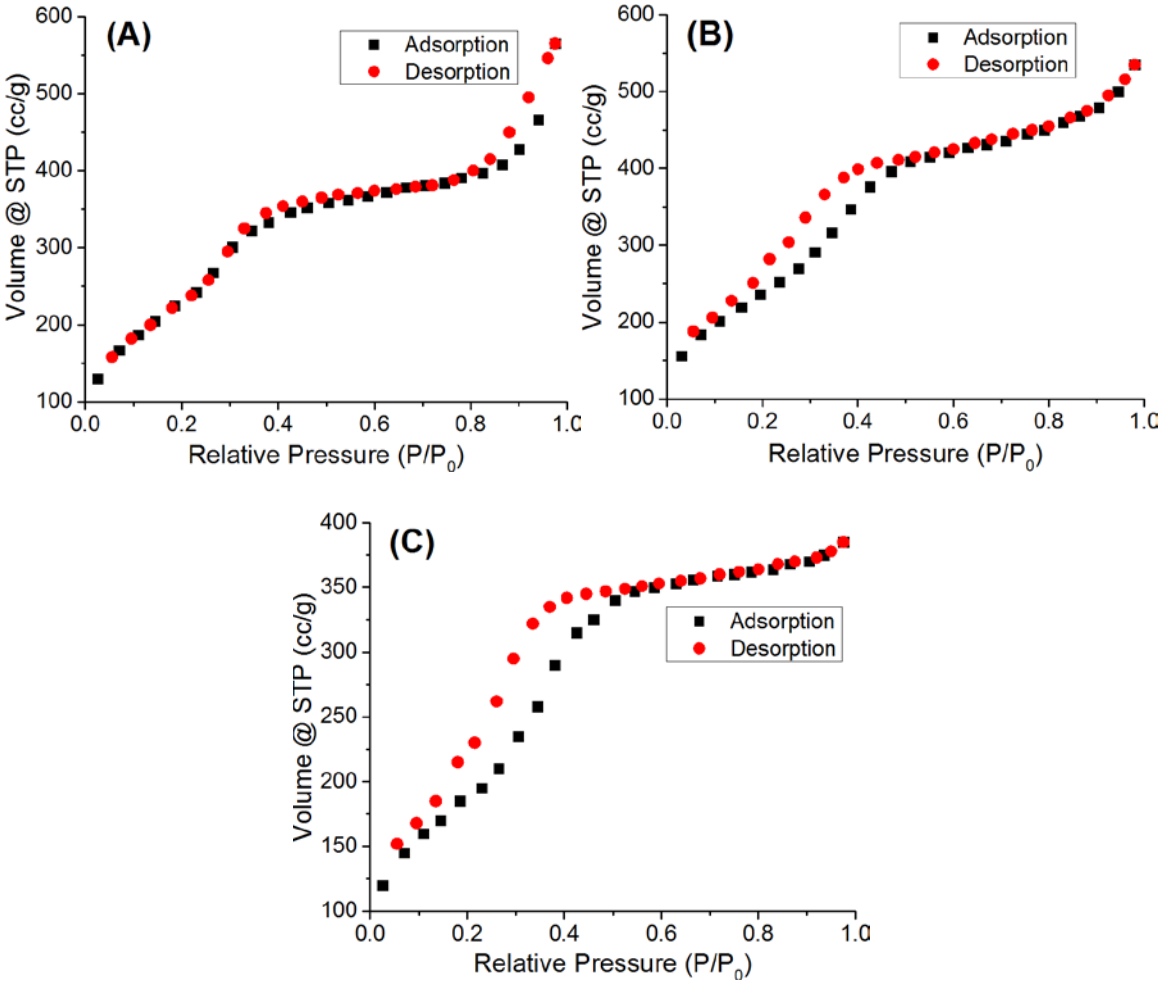

Figure 2-7. Fifty-point N_2 adsorption-desorption isotherms for MSNs: (A) MCM-41, (B) WO, and (C) mWO.

Table 2-3. Characterization and loading results of each MSN sample. The relative standard deviation (RSD) in diameter is based on measurements of n ≥ 50 particles.

Sample	Diameter[a] (nm, ± RSD)	Surface Area[b] (m2/g)	Pore Diameter[b] (nm)	Pore Volume[b] (cc/g)
MCM-41	52 (± 23%)	1016	3.16	0.35
WO	45 (± 22%)	944	3.12	0.33
Fe3O4@WO	78 (± 28%)	615	3.14	0.31

a Determined from TEM
b Measured by N_2 adsorption

2.5. Conclusions

Sub-100 nm MSNs of two pore structures, MCM-41 and WO, and a core-shell structure, mWO, were synthesized by varying the concentrations of NaOH and TEA to achieve the desired diameter. Core-shell mMCM-41 MSNs were synthesized with particle diameters larger than desired. The no-core particles had extremely high surface areas near 1000 m^2/g, and the inclusion of an Fe_3O_4 nanoparticle core in the mWO structure reduced the surface area to approximately 600 m^2/g. The MSNs were appropriate for subsequent use in drug delivery studies allowing us to investigate the effect of pore topology and iron oxide core on the loading and delivery of a model drug molecule.

CHAPTER 3: LOADING AND RELEASE OF DOXORUBICIN

3.1. Mesoporous Silica Nanoparticles for Drug Delivery Applications

Within the last 15 years, interest in the use of mesoporous silica nanoparticles (MSNs) as a substrate for drug delivery has emerged and increased enormously [7-9]. MSNs have been used for delivery of a variety of drugs including non-steroidal anti-inflammatory drugs such as ibuprofen and aspirin [7, 10], antibiotics such as vancomycin [12], and chemotherapeutics such as doxorubicin and methotrexate [15, 66]. Controlled delivery of the guest drug has been investigated through the variation of structural elements such as particle shape (disk-like, spherical, irregular) and pore size [16, 34], as well as through particle modification such as organic functionalization of the silica surfaces and the application of various pore-capping or particle coating procedures [12, 67-69].

Several studies have compared the effect of various ordered pore structures on the loading and release of drug molecules [18, 23, 40, 70, 71], but few have directly juxtaposed ordered and non-ordered topologies. Moreover, the previous comparisons of ordered and non-ordered porous silica materials did not isolate the effect of pore topology because the particle size and/or pore diameter were also varied in these studies [11, 72]. The study reported here controls for pore diameter and particle size. Additionally, although many drug delivery materials with Fe_3O_4 cores have been investigated, none have yet compared no-core particles to core-shell particles. This study provides the comparison to elucidate the effect of the Fe_3O_4 core on both drug loading and drug release.

Doxorubicin is a common chemotherapy treatment for a wide variety of cancers, including lung, breast, and ovarian cancers as well as lymphoma and leukemia. Doxorubicin is of particular interest for targeted drug delivery because the common method of administration, intravenous infusion of the drug in saline solution, carries a high risk of damage to the heart as well as lowering white blood cell and platelet production [73]. Using MSNs as a drug delivery system for doxorubicin may mitigate whole-body effects by constraining therapeutic concentrations to the target site. Doxorubicin can interact with the bare silica surface via a number of hydrogen bonding and electrostatic interactions (Figure 3-1), obviating the need for surface functionalization to facilitate loading.

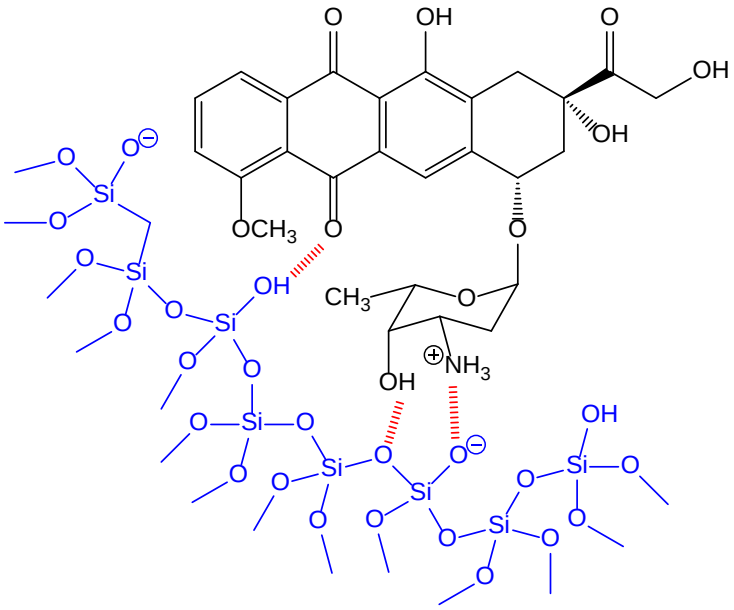

Figure 3-1. Molecular structure of doxorubicin (black) showing some of the hydrogen boding and electrostatic interactions (red dotted lines) possible with a bare silica surface (blue).

In order to determine the optimal particle structure to pair with doxorubicin in a drug delivery system, a series of three MSNs were considered – MCM-41, WO, and Fe_3O_4@WO. Each of these MSNs has an approximate 3 nm pore size with different pore

topologies, and in the case of Fe_3O_4@WO particles, iron oxide nanoparticle cores. WO silica has disordered, interconnected pores, and MCM-41 has parallel, hexagonally ordered pores. The loading and release of doxorubicin was investigated using these materials to isolate and evaluate the effects of pore topology and presence of a magnetic core on the amount of drug loaded and the kinetics of release. During the course of this study, the degradation of doxorubicin as monitored by fluorescence spectroscopy was also investigated because it is critical to an accurate determination of drug delivery kinetics.

3.2. Loading of Doxorubicin

Samples of MCM-41, WO, and Fe_3O_4@WO particles were loaded with doxorubicin by suspending 300 mg of particles in 5.0 mL of an aqueous solution of doxorubicin (1.35 mg/mL). The mixture was alternately sonicated for 15 minutes then refrigerated for 12 hours over the course of 3 days. The loaded material was separated by centrifugation and washed once with water. The supernatant and wash were collected. The loaded material pellet was suspended in 1.0 mL of absolute ethanol and dried overnight at 60 °C. The loading of doxorubicin into the particles was determined by fluorescence spectroscopy. Doxorubicin has intrinsic fluorescence (Figure 3-1) that is particularly advantageous for detection because, in contrast with absorbance spectroscopy, no other components of the loading system contributes to the fluorescent signal. Additionally, the technique is incredibly sensitive and can be used to detect the presence of doxorubicin down to nanomolar concentrations.

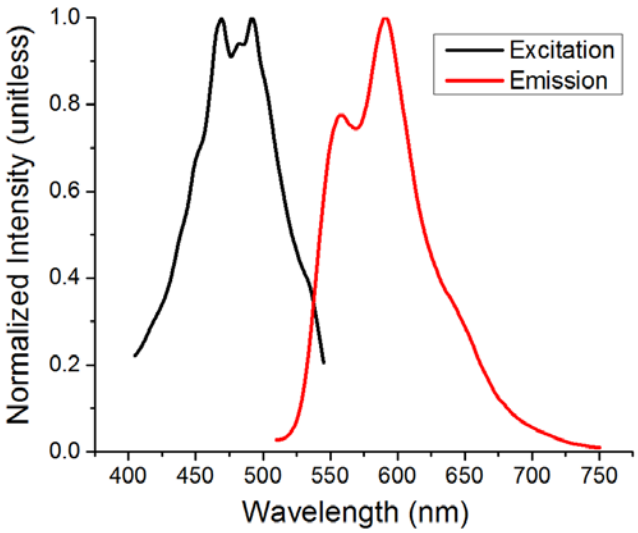

Figure 3-2. Fluorescence spectra of doxorubicin showing an excitation peak at 491 nm and an emission peak at 591 nm.

The collected supernatant and wash were analyzed using a FluoroMax-4 Spectrofluorometer (HORIBA). The loading was determined by two methods

$$Loading\ \left(\frac{mg\ dox}{g\ particle}\right) = \frac{m_{dox,orig} - m_{dox,super+wash}}{m_{particle}} \qquad \textit{Equation 3-1}$$

where $m_{dox,orig}$ is the mass of doxorubicin in the original 5.0 mL aliquot of solution, $m_{dox,super+wash}$ is the mass of doxorubicin remaining in the supernatant and wash, and $m_{dox,orig}$ is the mass of particles used. The results of this loading procedure for each sample is presented in Table 3-1.

Table 3-1. Loading results for each particle sample. Associated errors represent the standard deviation of n ≥ 3 trials.

Particle	Loading (mg/g)	Loading (μg/m^2)
MCM-41	14 (± 1)	14 (± 1)
WO	16 (± 2)	17 (± 3)
Fe_3O_4@WO	15 (± 1)	24 (± 2)

The doxorubicin loading of approximately 15 mg/g reported here is consistent with previous studies of doxorubicin on bare silica surfaces where the loading capacity

ranges between 10 and 40 mg/g [19, 24, 25]. Also, although the surface area of the Fe_3O_4@WO is reduced by about 30% compared to the parent WO (Table 2-3), the loading of doxorubicin per mass of particle was similar to the parent. When normalized to the surface area, the loading of doxorubicin into Fe_3O_4@WO particles, 24 μg/m^2, is significantly higher than the 17 μg/m^2 loading for the parent WO MSN ($p = 0.0180$). This suggests that the presence of the Fe_3O_4 core increases the loading, perhaps due to an enhanced interaction between doxorubicin and the Fe_3O_4 surface.

3.3. Fluorescence Detection of Doxorubicin

Fluorescence spectroscopy is an advantageous analysis technique due to the specificity and sensitivity of analyte detection – particularly for measuring extremely small amounts of doxorubicin. The ability to detect and quantify minute concentrations of doxorubicin allows for simple maintenance of perfect sink conditions, where the concentration of drug in solution does not inhibit additional dissolution, during drug release. However, doxorubicin is susceptible to photo, chemical, and thermal degradation and is known to degrade quite rapidly upon exposure to heat, light, and hydrolytic conditions [74], which significantly impacts the fluorescent signal. Initial release experiments conducted at physiological temperature and pH using phosphate buffered saline (PBS, 10 mM, pH 7.4) at 37 °C indicated that the fluorescent signal of doxorubicin undergoes significant decay, and, because of the potential impact on the measured release profiles, the degradation warranted further investigation. Very few studies in the literature have reported corrections for doxorubicin degradation, and clearly, this should be accounted for when using fluorescence for detection.

The degradation of doxorubicin under the release conditions was determined by spiking 100 mL of PBS at 37 °C with 100 µL of the doxorubicin solution (1.35 mg/mL). The solution was quickly agitated to homogeneity and an initial 1.0 mL aliquot removed. The container was then covered with aluminum foil to prevent photodegradation, and the solution was shaken at 200 rpm and incubated at 37 °C. Additional 1.0 mL aliquots were taken at time intervals and analyzed by fluorescence spectroscopy. The data were converted to percent by defining the fluorescence signal of the initial aliquot as 100%. The results are shown in Figure 3-3. These data show that, over the course of 24 hours, the fluorescence intensity of doxorubicin decays by approximately 50%.

In order to account for this degradation in the results obtained from release experiments, the degradation data were fit to the first order exponential decay model

$$D_t = D_0 * exp(-kt) \qquad \textit{Equation 3-2}$$

where D_t is the percent decayed fluorescence signal at time t in minutes, D_0 is the percent fluorescence signal of the initial aliquot, and k is the rate constant. The result of this fit is the line

$$D_t = 0.94\ (\pm\ 0.01) * exp\{[-5.2\ (\pm\ 0.5)] \cdot 10^{-4} * t\} \qquad \textit{Equation 3-3}$$

where the errors in the fitted parameters are indicated by the values in parentheses. Equation 3-3 is shown as the overlaid red fit line in Figure 3-3.

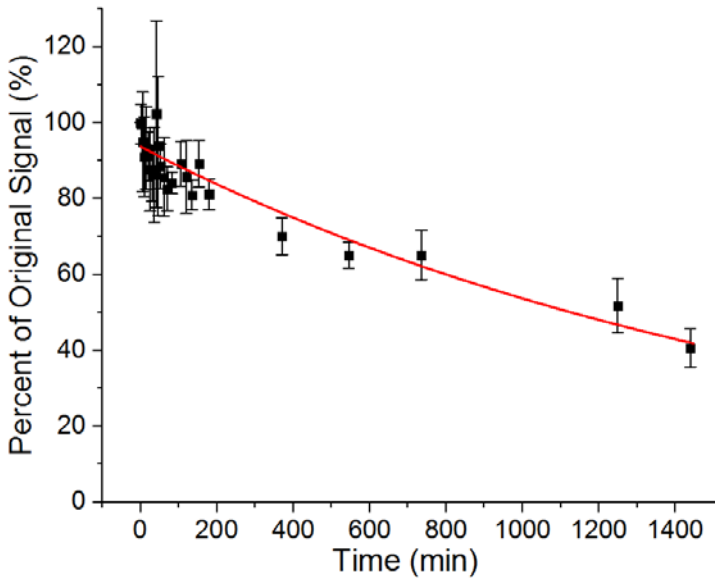

Figure 3-3. Decay of the fluorescence signal of doxorubicin in 10 mM PBS (pH 7.4) at 37 C. Data are averaged with error bars representing the standard deviation of n = 4 trials. The exponential decay fit line (D_t) is shown in red. The adjusted R^2 of fit is 0.583.

3.4. Release of Doxorubicin

The release of doxorubicin from the no-core particles was determined by suspending 50 mg of loaded particles in 100 mL of PBS (10 mM, pH 7.4) at 37 °C; to achieve complete suspension of the Fe_3O_4@WO particles, the procedure was scaled down to 30 mg of particle in 60 mL of PBS in the same container. The suspension was quickly agitated, and an initial time point was taken by removing three 1.0 mL aliquots. The removed volume was replaced with 3.0 mL of PBS at 37 °C. The container was covered with aluminum foil, and the suspension was shaken and incubated at 37 °C. The shaking rate was 200 rpm for the no-core particles and 220 rpm for the Fe_3O_4@WO particles. Additional 1.0 mL aliquots were taken in triplicate at time intervals and the removed volume replaced with PBS at 37 °C. The application of a static magnetic field to

the release of doxorubicin from Fe_3O_4@WO was achieved by fixing a neodymium magnet to the exterior of the release container for the duration of the experiment.

Each aliquot was centrifuged to remove any suspended particle and analyzed by fluorescence spectroscopy. The data were corrected for degradation using the equation

$$M_t = M_{m,t}/D_t \qquad \textit{Equation 3-4}$$

where M_t is the corrected amount of doxorubicin released at time t in minutes, $M_{m,t}$ is the measured amount of doxorubicin released at that time, and D_t is the percent decay of the measured signal at that time as determined by Equation 3. After correcting for the decay of the fluorescence signal, the release of doxorubicin from each particle type was normalized to the total doxorubicin available to the system, yielding a percent-based release for each particle type to facilitate comparisons. Over the course of 24 hours, less than 25% of the loaded drug was released from the particles, and, in each case, the majority of drug release occurred within the first 5 hours.

3.4.1. Kinetic Modeling

To elucidate the release mechanism and kinetics of the drug release, the data were fit to three models: Korsmeyer-Peppas, first order kinetic release, and Weibull models. The first approach is the Korsmeyer-Peppas release model [75]

$$\frac{M_t}{M_\infty} = kt^n \qquad \textit{Equation 3-5}$$

where M_t is the corrected amount of doxorubicin released at time t in minutes, M_∞ is the total amount of doxorubicin in the loaded particles, k is a complex kinetic parameter indicative of the host-guest pair, and n is a parameter that is characteristic of the host

shape and drug transport mechanism. The second approach is the first order kinetic release model

$$\frac{M_t}{M_\infty} = 1 - exp(-kt) \qquad \textit{Equation 3-6}$$

where k is the first order kinetic release constant. The third approach is the purely empirical use of the Weibull function [76, 77]

$$\frac{M_t}{M_\infty} = 1 - exp(-at^b) \qquad \textit{Equation 3-7}$$

where a and b are constants. The fit results are shown in Figure 3-4 and Table 3-2. As can be seen in Figure 3-4, the first order kinetic release model, Equation 3-6 (blue dashed line), shows the poorest overall conformity to the data in every case. For the relatively fast release from the MCM-41 and WO samples, Equation 3-6 overestimates the release at early time points and significantly underestimates the release at later time points. For the slower release profiles of doxorubicin from Fe_3O_4@WO with and without the applied magnetic field, the first order kinetic release model underestimates the release at both early and late time points while overestimating the release in the intermediate.

The Korsmeyer-Peppas and Weibull models, both conform more closely to the release data of all four samples, sometimes resulting in nearly identical fit lines (Figure 3-4B and C). The Weibull model a parameters are similar for the drug release from

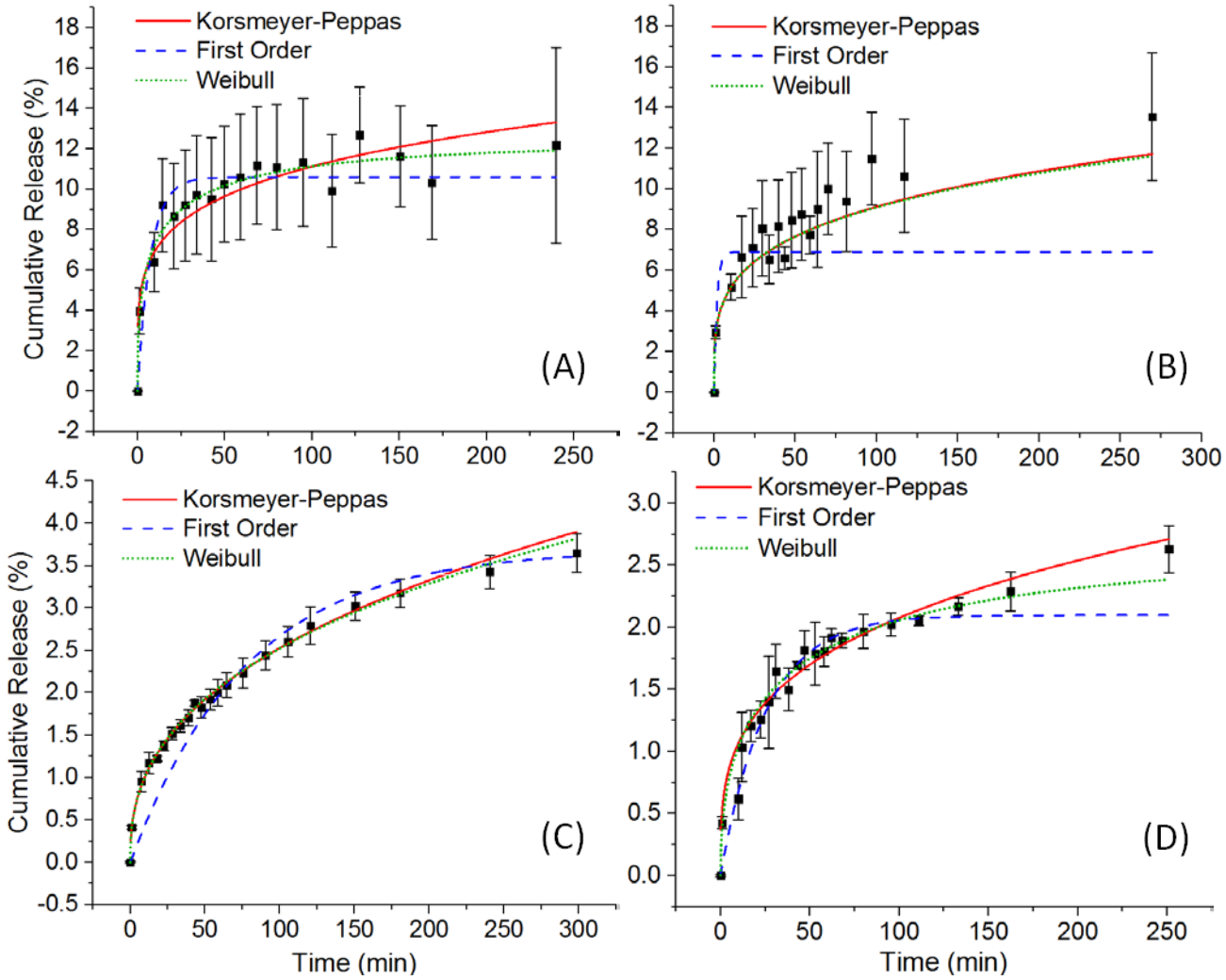

Figure 3-4. Fittings of Equations 3-5 (red solid), 3-6 (blue dashed), and 3-7 (green dotted) for the release of doxorubicin from MCM-41 (A), WO (B), Fe_3O_4@WO (C), and Fe_3O_4@WO with applied magnetic field (D). Error bars indicate standard deviation of n ≥ 3 trials.

Table 3-2. Fitted parameters, their associated errors, and two indicators of fit (adjusted R^2 and reduced χ^2) for the modeling of each data set.

		MCM-41	WO	Fe_3O_4@WO	Fe_3O_4@WO (applied magnet)
Korsmeyer-Peppas	k	4.3 (± 0.3)	2.8 (± 0.1)	0.43 (± 0.01)	0.41 (± 0.04)
	n	0.20 (± 0.01)	0.25 (± 0.01)	0.384 (± 0.006)	0.35 (± 0.02)
	Adj. R^2	0.907	0.937	0.976	0.938
	Red. χ^2	0.157	0.382	0.670	1.827
First Order	k	0.13 (± 0.03)	0.5 (± 0.1)	0.0128 (± 0.0002)	0.039 (± 0.004)
	Adj. R^2	0.969	0.955	0.930	0.961
	Red. χ^2	0.432	1.493	0.048	3.834
Weibull	a	0.34 (± 0.03)	0.30 (± 0.02)	0.20 (± 0.01)	0.16 (± 0.01)
	b	0.41 (± 0.06)	0.45 (± 0.08)	0.41 (± 0.01)	0.48 (± 0.03)
	Adj. R^2	0.955	0.988	0.965	0.968
	Red. χ^2	0.095	0.388	0.638	0.730

MCM-41 and WO as are the a term fits for the release from Fe_3O_4@WO with and without an applied magnetic field. The b parameter fits are relatively consistent across all four systems. The a terms for the WO and Fe_3O_4@WO, 0.30 (± 0.02) and 0.20 (± 0.01), respectively, are significantly different ($p < 0.05$). However, the conclusions we can draw from this comparison are limited to the general observation that the release of doxorubicin from Fe_3O_4@WO is much slower than that from WO. Although the Weibull model parameters have been shown to correlate with physically relevant parameters from other models [77], the application of the Weibull model is purely empirical.

While the Weibull fit parameters do not have intrinsic physical meaning, the Korsmeyer-Peppas model parameters contain information about kinetics and drug transport mechanism. Therefore, the Korsmeyer-Peppas model provides a basis for comparison across pore topologies, presence of an Fe_3O_4 core, and application of a magnetic field. The two fitted parameters for Equation 3-5 are the kinetic parameter k and exponential term n. For a spherical drug carrier, the exponent n should theoretically fall between 0.43 and 0.85 with the lower bound indicating release by Fickian diffusion and the upper bound indicating release by Case-II transport (matrix swelling and/or erosion) [76]. While there are no theoretical bounds for the k parameter, comparing the fit values of this quantity can elucidate differences between drug transport matrices.

3.4.2. Effect of Pore Topology

A visual inspection of the doxorubicin release profiles from the MCM-41 and WO particles show the high degree of variability of drug release from each of these particles

(Figure 3-5). The extent of overlap of the error bars renders a time-point by time-point comparison insufficient to determine the effect of pore topology. However, the kinetic fitting incorporates the spread of data within each time point as well as over the course of the entire experiment. This spread is reflected in the errors associated with each fitted parameter. Consequently, comparisons of the fitted parameters are reliable.

The comparison of the doxorubicin release profiles from MCM-41 and WO particles shows a statistically significant difference (p = 0.0012) in the fit of the k parameter in the Korsmeyer-Peppas model, 4.3 (± 0.3) and 2.8 (± 0.1), respectively. The k term is indicative of the host-guest pair, and the significant difference between these fitted values signifies a kinetic distinction between the drug release from MCM-41 and that from WO MSNs. Both MCM-41 and WO particles are small (approximately 50 nm)

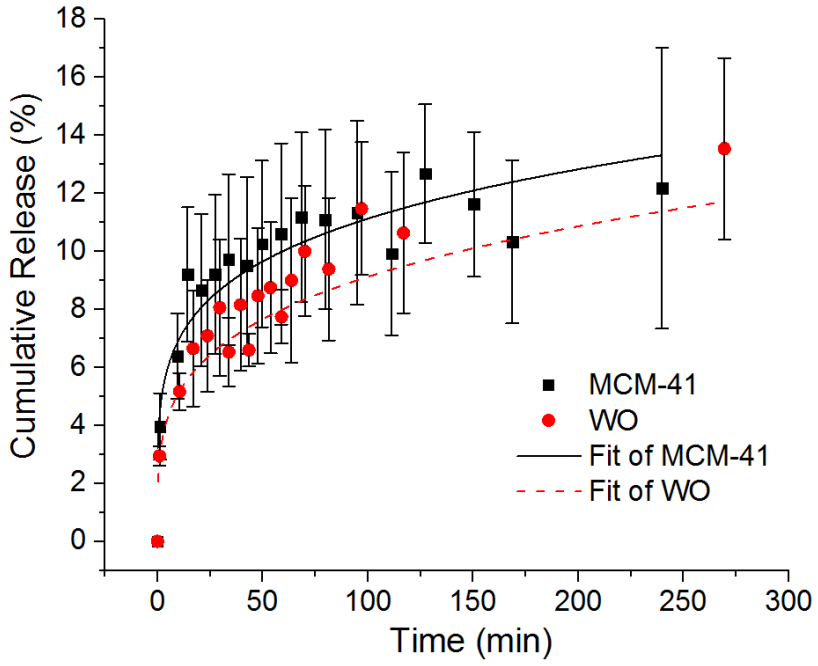

Figure 3-5. Comparison of the release of doxorubicin from MCM-41 and WO particles into PBS (10 mM, pH 7.4, 37 °C). Data are averaged with error bars representing the standard deviation of n ≥ 3 trials. The solid and dotted lines show the Korsmeyer-Peppas fits to the respective data sets with fit parameters listed in Table 3-2.

and spherical, and at the 5 hour mark, each releases approximately the same amount of doxorubicin (approximately 12%). However, the k term fits reveal that the pore structure has a small but statistically significant effect, observable in the faster initial release of doxorubicin from the MCM-41 particles versus the slightly slower but more sustained release from the WO particles.

The literature generally agrees that pore diameter has a strong impact on release kinetics; larger pores increase the release rate [16, 39]. Researchers are somewhat more divided on the issue of pore structure, with individual studies generally evaluating two or more ordered pore topologies. One study of two MCM-41-like structures that contained either radially oriented or entirely parallel pores indicated that pore structure has relatively little effect on the release profile [40]. However, another study of two differently-ordered pore structures, MCM-41 and MCM-48, showed that the cubic pore structure of the MCM-48 decreased the release rate, likely due to the longer mean free path of a drug molecule through the particle to reach the bulk solution [10]. This assessment of ordered and non-ordered pore structures of the same pore diameter shows the same trend as the MCM-41/MCM-48 comparison, with the three-dimensional disordered WO structure delaying release.

The n terms for MCM-41 and WO are 0.20 and 0.25, respectively, both below the theoretical lower bound of 0.43. According to the Peppas model for spherical particles, the n parameter should fall between 0.43 and 0.85 for the limiting cases of Fickian diffusion and Case II transport, respectively [75]. However, the n term fit values for MCM-41 and WO are smaller than the 0.43 lower bound, a result often seen in drug

delivery studies using sub-100 nm particles [21, 24, 78]. In a study of particle size distribution on the kinetics of drug release [79], Ritger and Peppas found that variation in particle sizes resulted in accelerated drug release at early time points due to diffusion from particles smaller than the mean size and delayed release at later time points due to diffusion from particles larger than the mean size. The combined effect of a distribution of particle sizes leads to a decrease in n. Therefore, when placed in context with the approximately 25% relative standard deviation in particle size for each MSN sample reported here (ref to CH 2 table), the low fit values for each n term are expected. Consequently, the fit values of 0.20 and 0.25 for MCM-41 and WO, respectively, indicate that the mechanism of drug release from both of these MSNs is controlled by Fickian diffusion.

3.4.3. Effect of Fe_3O_4 Core

Fe_3O_4-core particles are much denser than the 50 nm WO MSNs and are not as easily suspended in the release media. After the short, initial agitation (shaking by hand) which achieved homogeneity for the first aliquot, the Fe_3O_4@WO particles settled to the bottom of the release container, even under the vigorous shaking conditions (200 rpm) that fully dispersed the parent WO MSNs. To fully suspend the Fe_3O_4@WO particles, a slightly higher agitation rate (220 rpm) was employed with 60% of the original release volume. The effect of incomplete suspension of particles can be clearly seen in the release profiles obtained from each stirring rate (Figure 3-6).

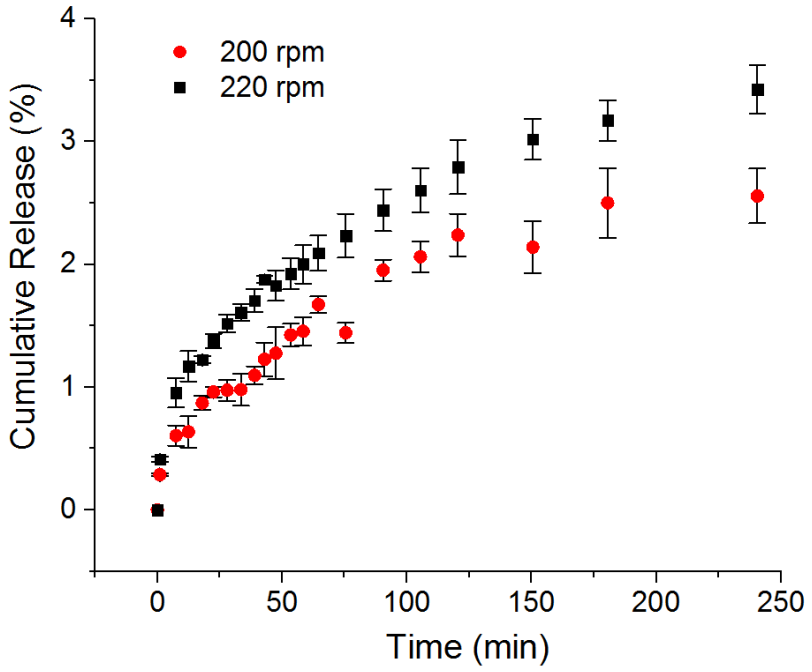

Figure 3-6. Doxorubicin release from Fe_3O_4@WO without complete agitation (red circles) and with complete agitation (black squares). Error bars indicate standard deviation of n = 3 trials.

By ensuring both the Fe_3O_4-core and parent WO MSNs were fully suspended for the duration of the release experiment, the general effect of including an Fe_3O_4 core on the release of doxorubicin can be seen in the obvious differences between release profiles (Figure 3-7). Overall, much less doxorubicin is released from the particles with an Fe_3O_4 core, with release only reaching approximately 3% at 300 minutes, a quarter of the approximately 12% release from WO particles. This reduced release is reflected primarily in the k term fits of 0.43 (± 0.01) and 2.8 (± 0.1) for the release from Fe_3O_4@WO and WO, respectively. The difference between the two k parameter fits is statistically significant ($p < 0.0001$), indicating a considerably slower initial release of doxorubicin from the Fe_3O_4 core particles.

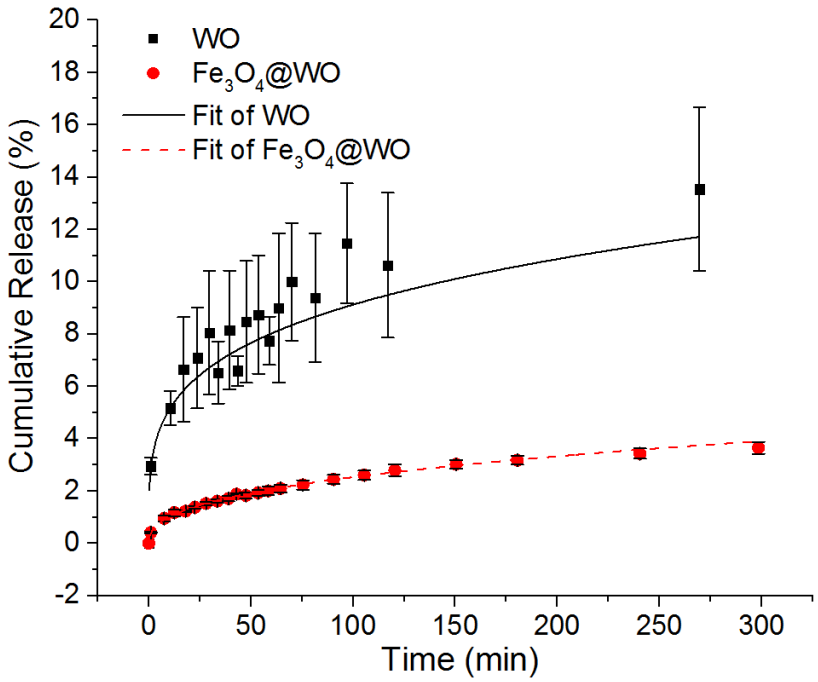

Figure 3-7. Comparison of the release of doxorubicin from WO and Fe_3O_4@WO particles into PBS (10 mM, pH 7.4, 37 °C). Data are averaged with error bars representing the standard deviation of n ≥ 3 trials. The solid and dotted lines show the Korsmeyer-Peppas fits to the respective data sets with fit parameters listed in Table 3-2.

The presence of the iron oxide core disrupts the release relative to the parent material. This is perhaps not surprising since the solid iron oxide cores are expected to have an impact on the diffusion and mean free path of doxorubicin through the particles. The fact that the kinetic profile changes so dramatically could also reflect the enhanced interaction between the core shell particles and the doxorubicin relative to the parent WO MSN. The n term fit is 0.38, which, like the Korsmeyer-Peppas fit of the release from WO particles, is below the lower theoretical bound, indicating diffusion controlled drug release from MSNs of varying radii. This comparison of cored and non-cored materials has not been reported in the literature previously and is of great importance when designing multifunctional materials for drug delivery and theranostic applications.

3.4.4. Effect of a Static Magnetic Field

The additional consideration of using an Fe_3O_4 core for targeted drug delivery via magnetic direction was investigated with the application of a static magnetic field to the release conditions. The magnetic field had only a small impact on the release of doxorubicin. At the 5-hour mark, there is less than 1% difference between the cumulative release from Fe_3O_4@WO with and without the applied magnetic field (Figure 3-8). The Korsmeyer-Peppas model fits correspondingly show very little variation. As

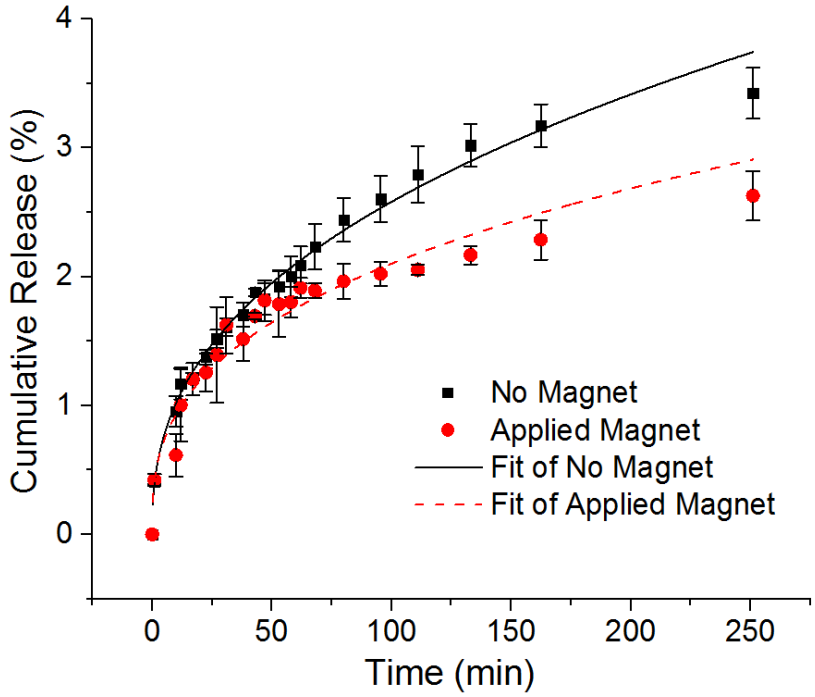

Figure 3-8. Comparison of the release of doxorubicin from WO and Fe_3O_4@WO particles into PBS (10 mM, pH 7.4, 37 °C). Data are averaged with error bars representing the standard deviation of n ≥ 3 trials. The solid and dotted lines show the Korsmeyer-Peppas fits to the respective data sets with fit parameters listed in Table 3-2.

determined by the similar fit parameters of 0.43 (± 0.01) and 0.41 (± 0.04) for the drug release from Fe_3O_4@WO with and without the application of a magnet, a static magnetic field has very little effect ($p > 0.05$, not significant). This result is consistent with another study of drug release from Fe_3O_4@SBA-15 (silica with mesopores

approximately 6 nm in diameter). As long as the drug does not contain a metal center (e.g. cisplatin), the static magnetic field has little influence on the drug release [41]. Consequently, magnetic localization is a viable possibility for targeted drug delivery.

3.5. Conclusions

Doxorubicin was loaded into each of three MSN samples – MCM-41, WO, and Fe_3O_4@WO. Although the loading per mass was similar across all MSN samples (approximately 15 mg/g), taking into account the reduced surface area of the Fe_3O_4@WO resulted in a significantly higher loading per surface area indicating a stronger interaction between doxorubicin and the Fe_3O_4@WO relative to the parent WO.

The release was monitored by fluorescence spectroscopy with corrections made for degradation. The release profiles were compared using the Korsmeyer-Peppas model. The exponential n term fits indicated a diffusion-controlled drug release mechanism for each sample. The kinetic parameter fits for drug release from MCM-41 and WO show a slight yet statistically significant trend toward faster release from the MCM-41 pore structure. This study is the first report of a comparison between ordered and disordered pore structures of the same pore diameter. The difference in release profiles indicates the necessity of tailoring pore topology as a fundamental step during development of drug delivery system in order to achieve the desired release profile.

A much more pronounced difference was observed in the kinetic parameter fits for the drug release from WO and Fe_3O_4@WO indicating a significantly slowed release due to the presence of the Fe_3O_4 core. This is the first report of the effect of

incorporating Fe_3O_4 cores on drug loading and release. The application of a static magnetic field to the Fe_3O_4@WO had very little effect on drug release. This expected result confirms the viability of Fe_3O_4@WO MSNs for targeted drug delivery via magnetic localization. Overall, presence of the iron oxide core had a greater impact on loading and release than did the pore topology. The Fe_3O_4 nanoparticle core lead to a higher loading per surface area and a much slower release. Ultimately, these results could be used to design and optimize drug delivery systems based on mesoporous silica nanoparticles.

CHAPTER 4: CYTOTOXICITY OF MESOPOROUS SILICA MATERIALS

4.1. Toxicity and Drug Delivery

One of the primary goals of drug delivery is to reduce system-wide side effects due to non-specific interactions of the therapeutic agent [9, 80]. This is attempted by sequestering the drug inside a host matrix with release only at the target site [81]. The host, then, rather than the drug, is subject to non-specific interactions until it reaches the target site. Therefore, an important consideration in the evaluation of a drug delivery system is the inherent toxicity of the host [52, 53, 58]. Toxicity is generally evaluated in two ways – *in vivo* animal studies to assess the biocompatibility and screen for serious side effects, and *in vitro* cell culture studies to determine specific interactions with healthy and diseased cell lines. Of particular interest for drug delivery of chemotherapeutics, encapsulation of a drug has been shown to enhance the therapeutic efficacy of treatment increasing cytotoxicity against target cells versus the free drug in solution, particularly for multiple-drug-resistant cancers [16, 33, 82]. Consequently, cytotoxicity studies are an essential step for evaluating DDSs for continued development.

In this study, due to the clinical application of doxorubicin to many different cancers, three cancerous cell lines – A549, HEC50CO, and CT26 – were selected for evaluating cytotoxicity *in vitro*. The A549 cell line is derived from a human pulmonary adenocarcinoma that is widely used for studies of lung cancer chemotherapeutics as well as toxicology of environmental pollutants and drug delivery carriers [83-86]. The HEC50CO cell line is derived from a human endometrial carcinoma and is representative

the type II cancer which is estrogen-independent and more clinically aggressive [87, 88]. The CT26 cell line is derived from a murine colon carcinoma that is often used in preclinical evaluations of new chemotherapeutics [89, 90].

Toxicity studies were conducted for MCM-41, WO, and Fe_3O_4@WO MSNs with each of these cell lines. Cytotoxicity is evaluated by treating cells with a range of concentrations of the suspended DDSs, and cell viability is assessed versus an untreated control sample. The free drug in solution was utilized as a positive control and to evaluate the effectiveness of comparable concentrations of the free and DDS-encapsulated drug.

4.2. Methods

4.2.1. Cell Culture Maintenance

Cell cultures for A549 and CT26 cell lines were maintained in RPMI-1640 medium (Gibco, Life Technologies), and HEC50CO cell cultures were maintained in DMEM medium (Gibco). All media were supplemented with 10% fetal bovine serum, 1% sodium pyruvate, 1% HEPES (4-(2-hydroxyethyl)-1-piperazineethanesulfonic acid) buffer (Gibco), and 0.1% gentamycin sulfate (IBI Scientific).

4.2.2. Nanoparticle Treatment

Cell lines were seeded into 96-well plates at 10,000 cells per well and incubated at 37 °C and 5% CO_2 for 24 hours. Nanoparticles at concentrations of 5, 50, 100, 300, and 500 µg/mL were suspended in complete media corresponding to each cell line by sonicating for 60 seconds with a probe sonicator (Fisher Scientific). Solutions of free doxorubicin at each concentration 5-500 µg/mL were also prepared in each medium as a

positive control. The culture medium was removed and the cells were treated with 200 µL of nanoparticle suspension or free doxorubicin solution, and a control was performed with 200 µL of fresh medium. The treated cells were incubated at 37 °C and 5% CO_2 for 24 hours.

4.2.3. Cell Viability via MTS Assay

The particle/free doxorubicin treatment volume was removed and replaced with 100 µL of fresh medium. Each well was spiked with 20 µL of MTS reagent (3-(4,5-dimethylthiazol-2-yl)-5-(3-carboxymethoxyphenyl)-2-(4-sulfophenyl)-2H-tetrazolium), and the cell cultures were incubated at 37 °C and 5% CO_2 for 4 hours. The 96-well plates were centrifuged for 20 minutes at 500 *g*. The supernatant was collected and the absorbance was measured at 490 nm. A blank well with medium and MTS regent was used to correct all absorbance values. Percent relative cell viability was calculated by normalizing the absorbance from the treated cells to the absorbance from the control cells.

4.3. Results and Discussion

4.3.1. Concentration Dependence of Toxicity on A549 Cells

The cell viability of the A549 cell line upon treatment with MCM-41 and WO MSNs is shown in Figure 4-1. The cell viability was generally consistent around 80% for all concentrations, 50 to 500 µg/mL, for both bare and doxorubicin-loaded MSNs. None of the nanoparticle treatments reduced the cell viability by more than 30 percent up to 500 µg/mL. Additionally, for doxorubicin alone, toxicity below 300 µg/mL was negligible. At treatment concentrations of 100 µg/mL and below, comparisons of the effects of

treatment with bare and doxorubicin-loaded WO and MCM-41 particles showed no significant differences within each concentration level. However, at the highest concentration of 500 µg/mL, doxorubicin-loaded WO particles showed a 15 percent reduction in cell viability versus bare WO particle ($p = 0.0073$). Additionally, significant differences of approximately 10 percent cell viability were observed between doxorubicin-loaded WO and MCM-41 at both 300 µg/mL and 500 µg/mL treatment levels ($p = 0.0065$ and 0.0125, respectively). Also, although the effect is not as pronounced as for free doxorubicin, doxorubicin-loaded WO particles showed a slight concentration dependence, with an approximate 18 percent reduction in cell viability between the 5 and 500 µg/mL concentrations ($p = 0.0003$, Figure 4-1).

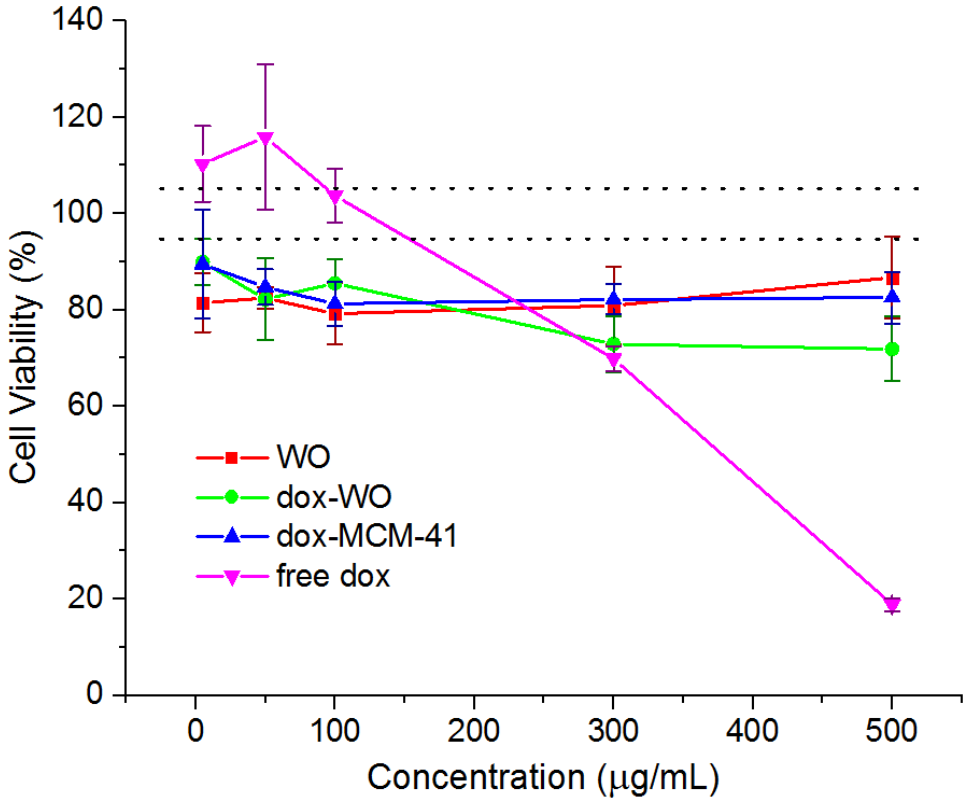

Figure 4-1. Toxicity against A549 cell line of bare and dox-loaded WO and MCM-41 particles. Error bars indicate standard deviation of 6 trials. Dotted lines denote standard deviation of the control.

The cytotoxicity against A549 cells of bare and doxorubicin-loaded Fe_3O_4@WO MSNs and Fe_3O_4 nanoparticles not coated in silica is shown in Figure 4-2. Similar to the MCM-41 and WO MSN treatments, the cell viability of A549 remained high with no nanoparticle treatment, 5 to 500 µg/mL At the lowest concentration, uncoated Fe_3O_4 nanoparticles reduced cell viability by 25 percent versus Fe_3O_4@WO ($p = 0.0003$), but neither the toxicity of Fe_3O_4 nor Fe_3O_4@WO is dose dependent (Figure 4-2). Similar to the doxorubicin-loaded WO particles, the doxorubicin-loaded Fe_3O_4@WO showed a

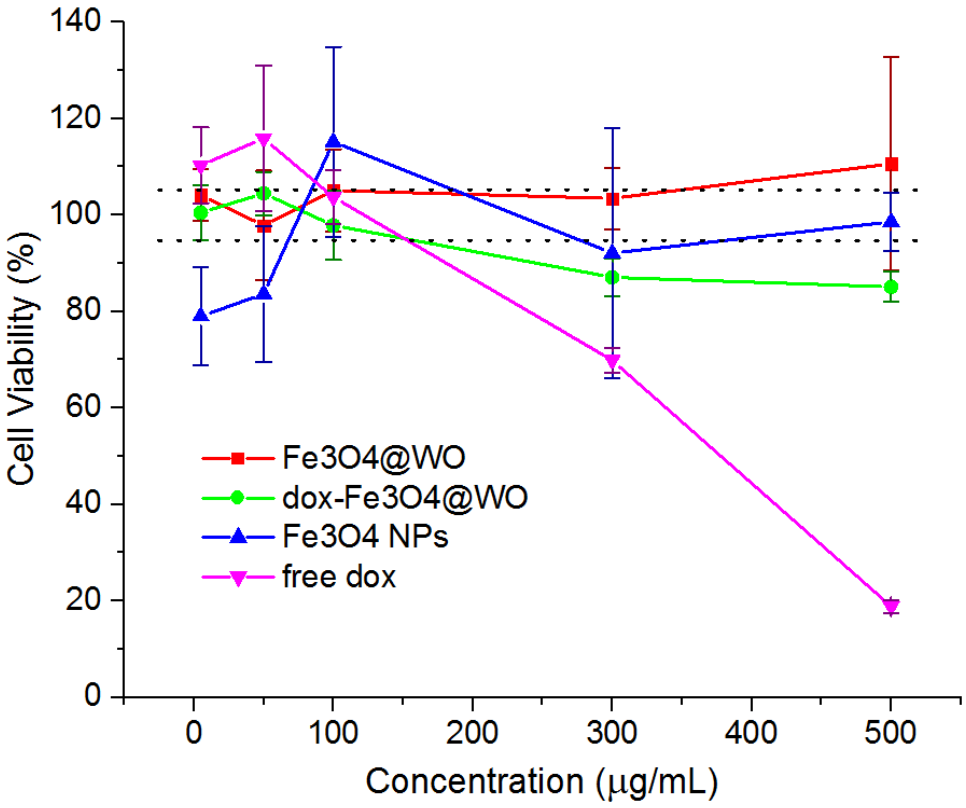

Figure 4-2. Toxicity against A549 cell line of bare and dox-loaded Fe_3O_4@WO particles and uncoated Fe_3O_4 particles. Error bars indicate standard deviation of 6 trials. Dotted lines denote standard deviation of the control.

slight concentration dependence, inducing an approximately 15 percent reduction in cell viability between the 5 and 500 µg/mL concentrations ($p = 0.0002$, Figure 4-2).

The low toxicity against A549 cells of the unloaded WO and Fe_3O_4@WO is consistent other studies of no-core and core-shell MSNs of similar sizes [91, 92]. Additionally, MCM-41 particles display similar toxicity to WO particles [57, 83]. The low toxicity of the doxorubicin-loaded particles is likely due to the reduced concentration of doxorubicin released from the particles versus the free doxorubicin positive control. Based on loading experiments, the particle treatments are composed of less than 1% doxorubicin by mass. Based on release studies, less than 25% of the loaded doxorubicin in each particle type is released, compounding the effect and resulting in estimated doxorubicin concentrations of approximately 0.5 to 1.5 µg/mL (Table 4-1) for the 500 µg/mL. It is likely that the sonication used to fully suspend the particles also stimulated release, so a maximum concentration can be calculated by assuming 100% release, resulting in doxorubicin concentrations of approximately 7 or 8 µg/mL.

Table 4-1. Summary of the range of possible doxorubicin concentrations administered to cells for the 500 µg/mL treatment level based on particle loading amount and 24 hour release percentages for each particle type.

Sample	Loading (mg DOX/g particle)	Cumulative release at 24 hours (%)	Estimated dox concentration (ug/mL)	Maximum dox concentration (ug/mL)
MCM-41	14	21	1.5	7
WO	16	16	1.3	8
Fe_3O_4@WO	15	6	0.45	7.5

4.3.2. Comparison of Toxicity among Cell Lines

Given the low concentration of doxorubicin released from the particles, comparisons of toxicity between bare and doxorubicin-loaded particles as well as between cell lines is most clearly demonstrated by the 500 µg/mL particle treatment. A

comparison of the cytotoxicity of the 500 µg/mL nanoparticle treatment among the three cell lines is shown in Figure 4-3. The cell viability of A549 cells remained high, at approximately 90% for bare nanoparticle treatments (Figure 4-3A). The doxorubicin-loaded nanoparticles decreased the cell viability by 10-15%, but cell viability remained above 70%.

Generally, the impact of particle treatments is greater for HEC50CO cells than A549 cells, and an even greater impact is seen for CT26 cells. Unloaded WO and Fe_3O_4@WO particles (Figure 4-3, solid red and blue columns) do not impact HEC50CO cells significantly more than A549 cells, but the cell viability of CT26 cells is greatly reduced for each, by approximately 35 percent for WO and 25 percent for Fe_3O_4@WO versus A549 ($p < 0.0001$ for both). CT26 cells are known to be more sensitive than a variety of other cancer cells to an assortment of perturbations of the culture conditions aside from anti-cancer therapeutics [46, 93].

Additionally, while A549 cells displayed no increased sensitivity toward Fe_3O_4 nanoparticles versus the silica-coated Fe_3O_4@WO particles, both the HEC50CO and CT26 cells show a significantly higher toxicity of uncoated Fe_3O_4 nanoparticles with cell viabilities for each below 50 percent (Figure 4-3, magenta and blue columns). Cell viability was reduced by 40 percent for HEC50CO cells ($p < 0.0001$) and approximately 20 percent for CT26 cells ($p = 0.0002$). Coating the Fe_3O_4 nanoparticles with mesoporous silica imparts increased biocompatibility of the drug delivery host in addition to the increased surface area and ease of functionalization. This is useful to note for the continued development of Fe_3O_4 nanoparticles for biomedical applications. Specifically,

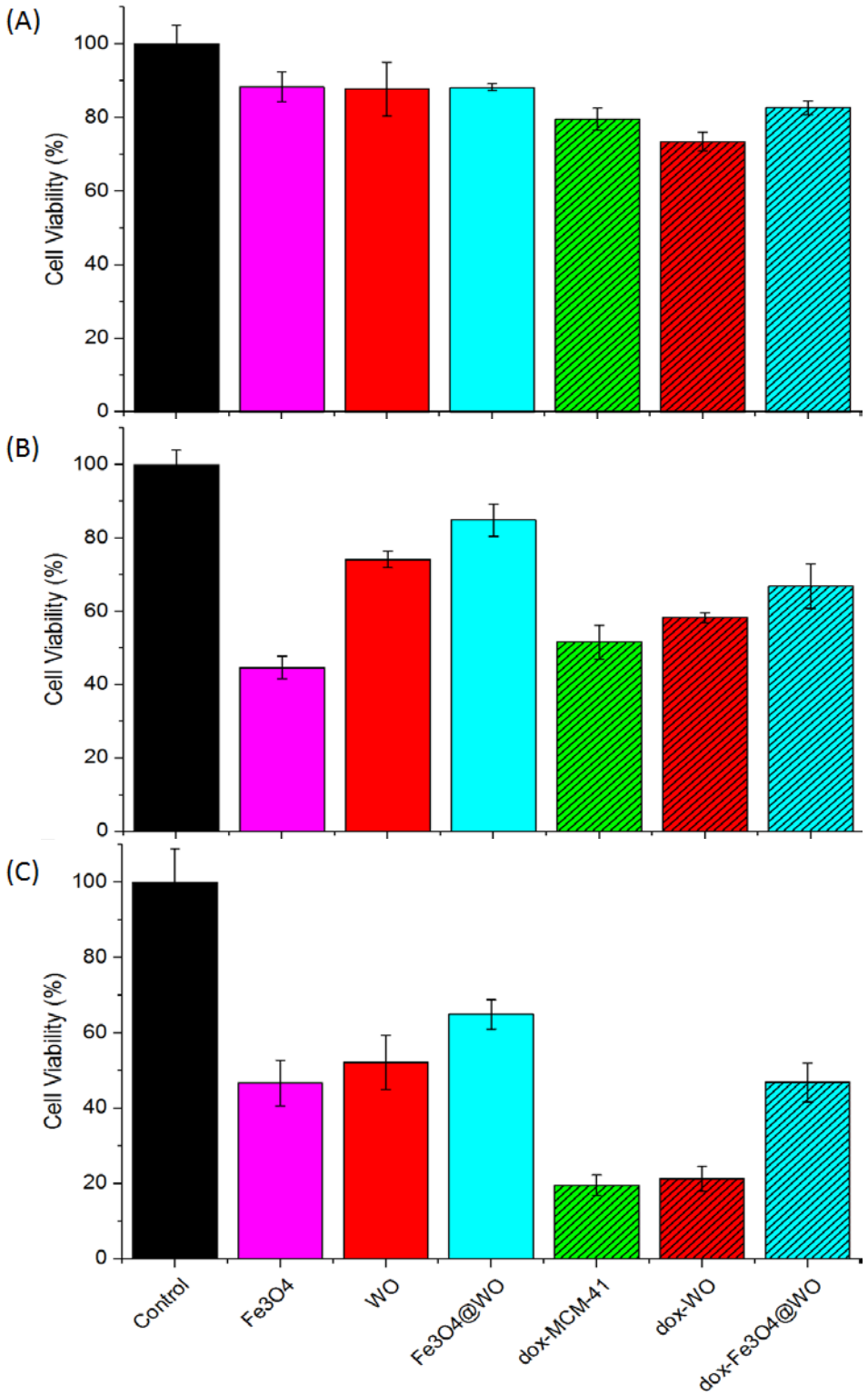

Figure 4-3. Cell viability results for the 500 µg/mL particle treatment level for (A) A549 cells, (B) HEC50CO cells, and (C) CT26 cells. Doxorubicin-loaded particle treatments are indicated by the striped columns. Error bars indicate standard deviation of 6 trials.

the toxicity effects of bare magnetite is of concern in the evaluation of other types of constructs, e.g. porous Fe_3O_4 shells and raspberry-like structures, for imaging and diagnostics, which leave the Fe_3O_4 surface open to cellular interactions [94, 95].

Although loading the particles with doxorubicin had a minimal effect on A549 cell viability, the impact was much more pronounced on the HEC50CO and CT26 cells. Doxorubicin loading decreased cell viability by approximately 15 percent for WO particles and 20 percent for Fe_3O_4@WO particles ($p < 0.0001$ and $p = 0.0002$, respectively) for HEC50CO cells, and the influence was even greater for CT26 cells, reducing cell viability by approximately 30 percent for WO particles and 20 percent for Fe_3O_4@WO particles ($p < 0.0001$ for both).

These results are expected when taken into context with the trend of susceptibility of each cell line to free doxorubicin. Particularly at low concentrations, A549 cells are nearly unaffected by doxorubicin (Figure 4-4, purple circles) with the onset of significant toxicity occurring at doxorubicin concentrations above 50 µg/mL. Although some low-concentration resistance was expected from A549 cells, the fact

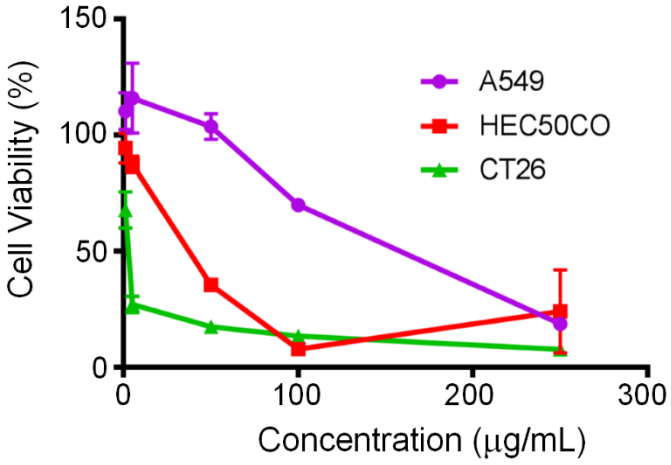

Figure 4-4. Toxicity of free doxorubicin at 1, 5, 50, 100, and 250 µg/mL against each of three cell lines. Error bars indicate standard deviation of 6 trials.

that the resistance to free doxorubicin extends to about 50 µg/mL is somewhat surprising given that many studies show an approximate 40% reduction in A549 cell viability at doxorubicin concentrations around 20 µg/mL [91, 96, 97].

In contrast, doxorubicin imparts approximately 10 percent toxicity against HEC50CO cells at 5 µg/mL, and even the lowest concentration applied, 1 µg/mL of free doxorubicin, reduced the cell viability of CT26 cells by almost 40 percent. These cell viabilities against free doxorubicin are typical of the HEC50CO and CT26 cell lines [87, 93, 98, 99]. The estimated release of doxorubicin from the nanoparticles is less than 10 µg/mL (Table 4-1), and the relative toxicity of the doxorubicin-loaded nanoparticle treatments across cell lines follows the trend observed for the toxicity of free doxorubicin.

Additionally, while doxorubicin-loaded WO and MCM-41 particles had similar effects within each cell line, the doxorubicin-loaded Fe_3O_4WO particles were significantly less toxic than the doxorubicin-loaded WO particles, by approximately 8 percent in the HEC50CO trials ($p = 0.0072$) and approximately 25 percent in the CT26 trials ($p < 0.0001$). Again, these results are expected in reference to the lower release of doxorubicin from Fe_3O_4-core particles compared to the no-core MSNs. Fe_3O_4@MS particle have been shown to have low toxicity against both healthy and cancerous cells [25, 100, 101] although a direct comparison to the cytotoxicity of the corresponding no-core MSN is not generally studied.

4.4. Conclusions

Mesoporous silica nanoparticles of two pore structures, WO and MCM-41, and a core-shell MSN, Fe_3O_4@WO, with and without a loaded anticancer drug doxorubicin, were investigated for their toxicity against three cancerous cell lines – A549, HEC50CO, and CT26. Additionally, the toxicity of an un-coated Fe_3O_4 nanoparticle core was investigated. A549 cells were resistant to both the bare and doxorubicin-loaded particles. Both HEC50CO and CT26 cells were more susceptible to the bare nanoparticles and the effect was increased upon doxorubicin loading, consistent with the concentration dependence of free doxorubicin toxicity for each cell line. Due to the low concentrations of doxorubicin released from the MSNs, these materials may only be of interest for continued development of treatment for cancers that are highly vulnerable to doxorubicin.

4.5. Acknowledgments

The cell experiments were performed by Angie S. Thorne, PhD, and undergraduate researchers Maria A. Castro and Kasey A. Coleman in the lab of Professor Aliasger K. Salem, PhD, in the Department of Pharmaceutical Sciences and Experimental Therapeutics at the University of Iowa.

CHAPTER 5: HYDROPHOBIC MESOPOROUS SILICA PARTICLES FOR TISSUE PHANTOM CONSTRUCTION

5.1. Fluorescent Tissue Phantoms

Tissue phantoms are synthetic imitations of biological tissue that can be used to mimic many characteristics of tissue including optical, acoustic, thermal, and mechanical properties [102-107]. These properties can be adjusted in the synthetic material to simulate disease progression for the development of diagnostic or treatment techniques [105, 108, 109]. For example, the spectroscopic properties of tissue – scattering, absorbance, and fluorescence – can be modeled in a synthetic material by incorporating a range of concentrations of cellular components with optical properties such as flavin adenine dinucleotide (FAD) and nicotinamide adenine dinucleotide (NADH) [103, 110].

FAD and NADH are endogenous fluorophores that are involved in the electron transport chain making them especially useful for monitoring metabolic activity [110, 111]. During formation of a tumor, for example, metabolism accelerates to facilitate the rapid cell division that is characteristic of cancerous tissue. Along with this increase in metabolism, there is a predictable change in the concentrations of FAD and NADH [110]. Here, the possibility arises of generating a library of tissue phantoms that mimic the fluorescent properties of cancerous tissue at several stages along the disease progression. Particles loaded with concentrations of FAD and NADH corresponding to healthy, hyperplastic, and cancerous cells could be suspended in media with healthy concentration levels of FAD and NADH. These phantoms are of particular interest for the development of an optical method of cancer detection and diagnosis that could be

applied non-invasively and provide instantaneous and quantitative results with high sensitivity [112].

An essential requirement for validating such a diagnostic technique is the ability to clearly distinguish boundaries between adjoining regions that have different spectral properties such as would be found in real tissue due to cellular membranes. Hydrophobic mesoporous silica particles provide biochemically well-defined micrometer and nanometer domains due to hydrophobic trapping of loaded molecules. Hydrophobic trapping is the ability to efficiently prevent leaking of the loaded molecules by excluding aqueous solvent from the pores when the particles are suspended in an aqueous phantom matrix such as agar [103, 113, 114]. This trapping is experimentally simple. A target molecule is loaded into these hydrophobic pores using an organic solvent which can wet the pore and transport the dissolved target molecule throughout the pores; the fluorophore partitions into the C_{18} layer; the solvent is removed and the particle is dried; and finally, the C_{18} layer prevents an aqueous suspension medium from wetting the pores keeping the target molecule trapped inside the dry pore (Figure 5-1). Importantly, in contrast with other methods of trapping – covalent bonds between the

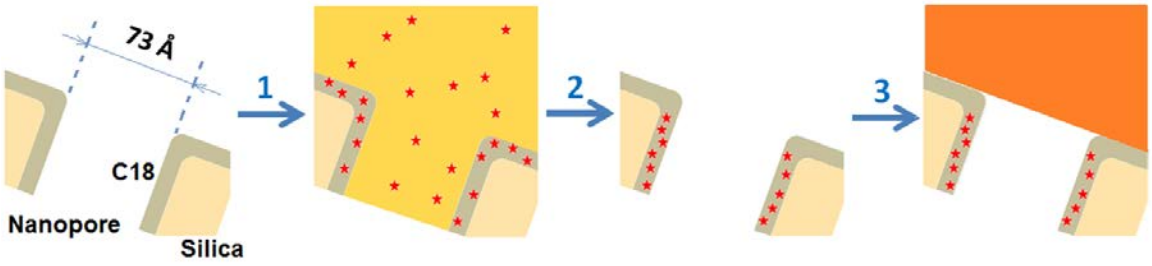

Figure 5-1. A schematic close-up of the mouth of a pore on a silica particle (beige) coated with a layer of C_{18} (gray) showing the loading and hydrophobic trapping of a fluorophore (red stars) with an organic loading solvent (yellow) and an aqueous suspension medium (orange). Modified from [113].

loaded molecule and the vessel wall or a physical plug inserted in the mouth of the pore – hydrophobic trapping is accomplished simply; no additional synthetic step is necessary, nor does trapping require chemical or mechanical means, which could alter the optical properties.

A second requirement for developing a robust optical methodology is uniformity of the tissue phantom samples that are used to calibrate an optical device. Two specific barriers to the generation of a uniform tissue phantom have been identified – distribution of loaded molecules in the mesopores and dispersal of hydrophobic particles in agar. Previously, uniform suspension of loaded hydrophobic mesoporous silica particles in agar has been difficult because of the tendency of the particles to aggregate in aqueous media [103]. Therefore, the uniform dispersal of these particles in agar is necessary as a proof of concept study for the creation of a usable tissue phantom. Here, the uniform dispersal of particles in agar is accomplished through surfactant coating versus attempts with various combinations of sonication and vortex mixing.

5.2. Tissue Phantom Construction

5.2.1. Fluorescent Labeling of Hydrophobic Mesoporous Particles

C_{18} LUNA chromatography resin was purchased from Phenomenex. The resin particles are silica, 10 µm in diameter, with a disordered, interconnected network of pores that are 10 nm in diameter. The surface area (400 m^2/g) is covalently coated with an octadecyl (C_{18}) moieties which also line the pores, and remaining silanols are trimethylsilyl (TMS) endcapped to yield an entirely non-polar surface. The particles were

loaded with rhodamine 6G (R6G, Sigma-Aldrich) by mixing 1 g of particles with 3 mL of a 20 µM R6G solution in 200 proof ethanol on a rotatory shaker for 12 hours. The mixture was allowed to settle for several hours; the supernatant was removed; and the wet particles were dried at 40 °C for 3 days.

5.2.2. Particle Dispersal in Agar via Sonication and Vortex Mixing

All prepared phantoms were made with 0.25 g of loaded particles and 25 mL of a 1% (w/w) solution of agar in Millipore water (18.2 MΩ cm) at 50 °C. Sonication was performed in a sonic bath at 50 °C to prevent gelling of the agar. The tissue phantom 1 (TP-1) mixture of particles and hot agar was immediately sonicated for 10 minutes then poured into a mold. The TP-2 mixture was vortex mixed for 15 seconds then sonicated for 10 minutes before being poured into a mold. The TP-3 mixture was prepared with two repetitions of alternately vortex mixing for 15 seconds and sonicating for 3 minutes before being poured into a mold. The TP-4 mixture was prepared with four repetitions of alternately vortex mixing for 15 seconds and sonicating for 1 minute before being poured into a mold. All molds were allowed to solidify at 5 °C for 12 hours to form the tissue phantom.

5.2.3. Particle Dispersal in Agar via Surfactant Coating

A 12.5 mM solution of sodium dodecyl sulfate (SDS) surfactant was used for the phantom preparations with surfactant-coated particles. Loaded particles (0.25 g) were added to 2 mL of SDS solution and immediately vortex mixed for 10 or 30 minutes. The resulting foam was allowed to settle for eight hours to form a dense layer on top of the liquid. The foam was gently resuspended in the SDS solution, and 1 mL of the foam

suspension was added to 25 mL of agar solution. The mixture was swirled by hand for 30 seconds then poured into a mold. The sample prepared with 10 minutes of vortex mixing the particles with SDS formed TP-5, and the sample prepared with 30 minutes of vortex mixing the particles with SDS formed TP-6. The molds were allowed to solidify at 5 °C for 12 hours.

5.2.4. Confocal Fluorescence Microscopy of Tissue Phantoms

The images of the tissue phantoms were collected on a Bio-Rad Radiance 2100MP confocal microscope with 514 nm excitation from an argon laser and detection band formed with an HQ590/70 band pass filter (555 nm – 625 nm) using a dry 20x lens. Phantoms were imaged whole with optical sections starting at the surface and extending 50-200 micrometers into the phantom body. Images were prepared using ImageJ software (freeware from the National Institutes of Health).

5.3. Qualitative Analysis of Tissue Phantoms

5.3.1. Rhodamine 6G Labeling of C_{18} LUNA

The materials utilized for construction of these tissue phantoms have a number of advantageous properties. The 10 µm-diameter C_{18} LUNA particles provide a microscopic domain with a size on the same order of magnitude as a cancer cell. The essential requirement of an optical tissue phantom to maintain a target molecule within the boundary of that domain is easily achieved due to the hydrophobic surface. Once a molecule of interest is loaded into the particles and the particles are dried, the aqueous agar solution used for the body of the matrix cannot wet the pores [114]. With no solvent available to the loaded molecules, the molecular composition inside the particle

domain is maintained. Rhodamine 6G (Figure 5-2 inset) was used to label the C_{18} LUNA particles because it is a highly fluorescent dye (Figure 5-2) is photochemically stable in a wide variety of solvents [115, 116], and the spectral properties are consistent across a wide range of concentrations and solvent polarities [117]. Additionally, the background

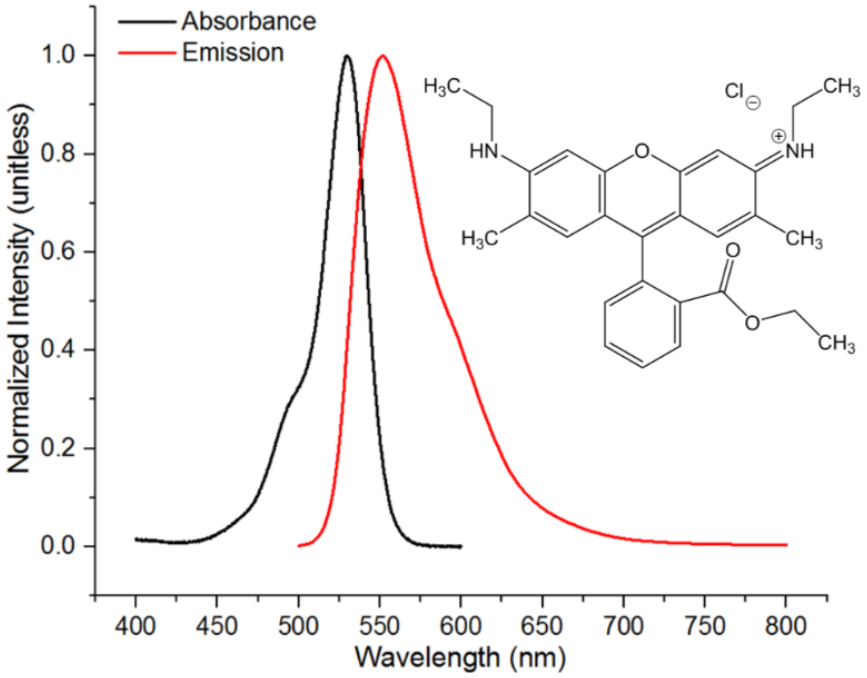

Figure 5-2. Absorbance and emission spectra for rhodamine 6G (R6G). Inset: molecular structure of R6G.

signal generated by the other phantom materials – C_{18} LUNA, SDS, and agar – is negligible, approximately 65 times lower than the signal from R6G-loaded particles (Figure 5-3).

The loading process is simple, using ethanol to wet the pores and transport R6G throughout the particle for partitioning into the C_{18} layer in the pores. Removing the surplus solution before drying prevents excess deposition of R6G on the particles during the evaporation of the solvent. Fluorophore molecules adsorbed to the exterior surface of the particles could be removed via a washing step with water. However, because the

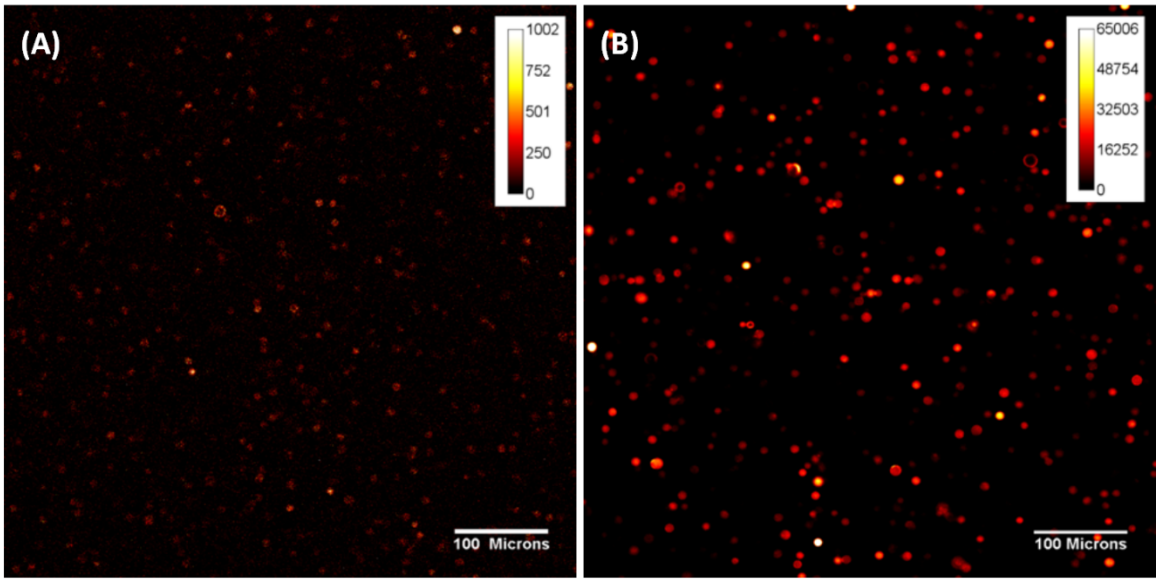

Figure 5-3. Confocal microscopy images showing (A) the background signal from a TP-6 phantom without R6G-labeled particles, maximum intensity 1002 counts and (B) the signal a TP-6 phantom with R6G-lableled particles, maximum intensity of 65006 counts.

outer surface area comprises a miniscule portion of the total surface area of each particle, removing the externally adsorbed R6G was determined to be unnecessary. As the ethanol in the pores evaporates during the drying step, the R6G is redistributed inside the particles. This redistribution manifests as a variation of fluorescence intensity across the particle (Figure 5-4A). The variation can be observed using a cross-sectional intensity profile of the particle (Figure 5-4B). The range of average intensities per particle and the assortment of intensity profiles across each particle indicate that the partitioning of R6G into the C_{18} layer and redistribution during drying is highly variable particle-to-particle.

The two most commonly observed profiles are (1) a generally increasing fluorescence intensity toward the center of the particle and (2) a generally flat intensity across the particle. The first profile with the highest intensity at the center has been previously reported for flavin adenine dinucleotide (FAD) loaded into C_{18} LUNA with an

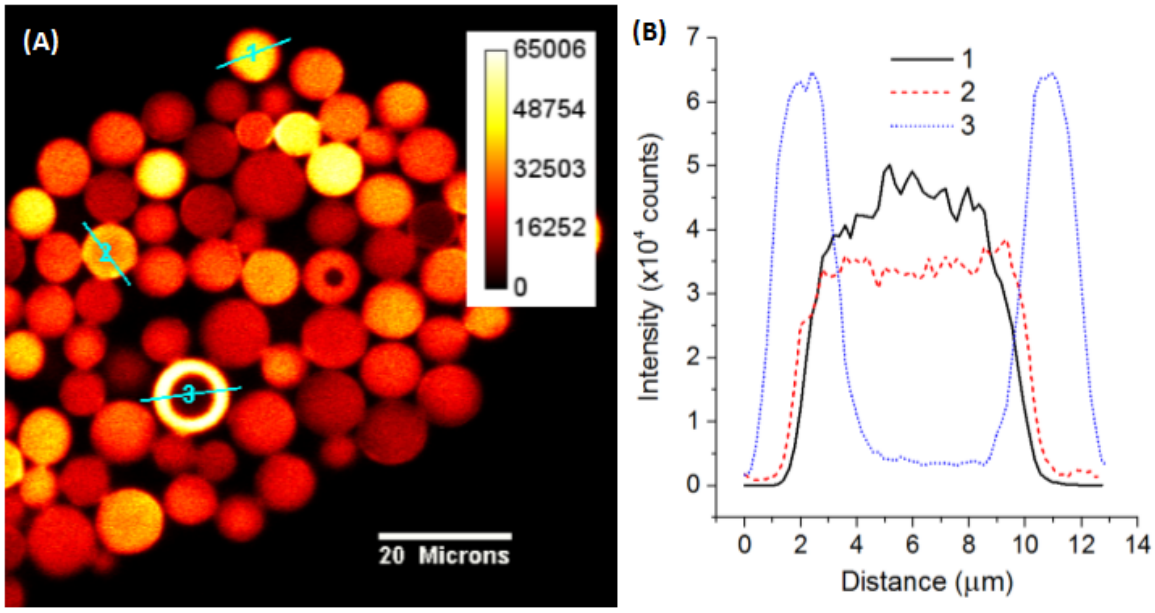

Figure 5-4. (A) Confocal microscopy image of R6G-loaded C_{18} LUNA suspended in agar with cross-sections of three selected particles. (B) Cross-sectional fluorescence intensity profiles corresponding to each of the selected particles.

acetonitrile/water solvent mixture [103]. As solvent evaporation progresses from the pore opening into the pores toward the center of the particle, the ethanol-soluble R6G is carried along with the solvent front. The result is a higher concentration of fluorophore in the middle of the particle.

The gradients observed from edge to center for R6G-loaded particles, however, are considerably less pronounced than for FAD. This is likely due to the much higher polarity of FAD. The partitioning of FAD into the C_{18} phase from the acetonitrile/water solvent is much lower than R6G from ethanol. Consequently, the majority of FAD in the particle pores prior to solvent evaporation was more strongly associated with the liquid rather than the C_{18} layer. During drying, the receding solvent front pulled the majority of the loaded FAD farther toward the center of the particle. Conversely, R6G is much less polar and interacts much more readily with the C_{18} layer. Consequently, the receding

solvent front has less impact on the redistribution of R6G. This reduced redistribution of R6G may also result in the many particles displaying a generally flat fluorescence intensity profile.

Less commonly observed are “loop” profiles with high intensity at the outer edges of the particle and low intensity at the center (Figure 5-4B-3). There are two possible causes for this pattern. First, the entire particle may not have been wetted during the loading step. Second, the structure of the particle may have prevented solution from reaching the center. It is possible that the particle has a solid silica core with a mesoporous shell, and only the porous portion of the particle would come into contact with the R6G solution. Although the R6G-labeling varies particle-to-particle, this proof of concept requires only that each particle is identifiable by fluorescence in order to determine location. Uniform distribution of R6G throughout the particle is not necessary.

5.3.2. Particle Dispersal via Sonication and Vortex Mixing

The general extent of particle incorporation based on each preparation method can be clearly seen upon a visual inspection of the tissue phantoms (Figure 5-5). Sample TP-1, which was treated with sonication only, shows large aggregates of particles that

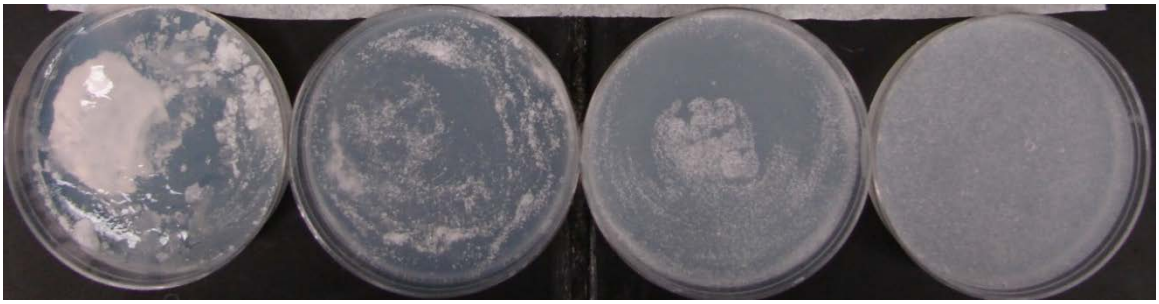

Figure 5-5. Picture of tissue phantoms generated via sonication and vortex mixing. From left to right: TP-1, TP-2, TP-3, and TP-4. Molds are 5 cm in diameter.

formed at the boundaries of the phantom body, along the bottom and sides of the mold as well as on the surface of the agar with sizable volumes of translucent, particle-free agar. Samples TP-2 through TP-4, which were both vortex mixed and sonicated, show significantly increased incorporation of particles into the phantom body with fewer and fewer aggregates remaining at the surface of the agar. During the vortex mixing process, many large clusters of particles were mixed into the viscous agar solution. Upon sonication, these masses appeared to burst almost immediately, leaving much smaller aggregates and individual particles within a similar volume of the phantom as the original large cluster. Subsequent vortex mixing and sonication further disseminated and dispersed the smaller aggregates, resulting in the increasingly opaque appearance of the phantom.

Confocal microscopy imaging enables the compilation of a three-dimensional image to further assess location and aggregation of the particles at the surface and in the body of the tissue phantom. Several areas of each phantom, which were visibly heterogeneous, were investigated to provide a representative view of the entire mold. Samples TP-1 and TP-2 contained large volumes of particle-free agar. Because the agar contained no fluorescent label, these images appeared entirely blank. Conversely, samples TP-3 and TP-4 contained particles in all investigated regions in varying numbers and degrees of dispersal. Selected images of each tissue phantom, which display a representative region of particle incorporation for each sample, are shown in Figure 5-6 through Figure 5-9.

The image of TP-1 (Figure 5-6) displays an extended cluster of particles on the surface of the phantom along with some individual particles and small aggregates. A small number of particles and aggregates have been incorporated into the matrix body with only a few being observed within the 100 micron image depth. This image of TP-1 indicates that sonication alone was not sufficient to incorporate many of the particles into the body of the tissue phantom. This result is consistent with previous phantom construction techniques utilizing the same C_{18} LUNA particles and 1% agar phantom matrix [103, 118].

By combining sonication with vortex mixing, the incorporation of particles into the body of the matrix is greatly increased (Figure 5-7 through Figure 5-9). Vortex mixing breaks the surface of the agar solution to allow large clusters of particles to reach the interior. Subsequent sonication further divides those large aggregates. The image of TP-2 (Figure 5-7) shows both small aggregates and individual particles incorporated and dispersed within the body of the phantom. Here, it is important to evaluate this image in context with the macroscopic visual inspection of TP-2. TP-2 is visibly heterogeneous (Figure 5-5). Although portions of TP-2 display the desired individual particle dispersal, spectroscopic measurements of tissue phantoms prepared according to this method – 15 seconds of vortex mixing and 10 minutes of sonication – would be strongly influenced by sampling location. Consequently, the TP-2 preparation method is not appropriate for constructing tissue phantoms for either disease simulation or instrument calibration.

Treatment of the particle-liquid agar mixture with alternating periods of vortex mixing and sonication decreased the visible heterogeneity of TP-3 and TP-4 (Figure 5-5). Indeed, all 600 µm by 600 µm by 100-200 µm (length by width by depth) portions of TP-3 and TP-4 investigated by confocal microscopy displayed a combination of clusters and individual particles (Figure 5-8 and Figure 5-9). Interestingly, recurrent vortex mixing also generated air bubbles in the agar solution that were not eliminated by sonication. As can be seen in Figure 5-8 and Figure 5-9, some of the air bubbles are lined, partially or fully, with particles. Additionally, some bubbles are not associated with any particles. The particle-free bubbles were only observed by transmitted light because no fluorophore was used to label the matrix.

The air bubbles retained in TP-3 were mostly spherical (Figure 5-8) whereas those retained in TP-4 were irregularly shaped (Figure 5-9). This is likely due to increased viscosity of the agar solution as it cooled. Although the sonication bath was maintained at 50 °C, vortex mixing occurred at room temperature, allowing the temperature of the agar solution to decrease during the mixing step. Agar solution (1% w/w) begins to gel when the solution cools to approximately 35 °C and will not subsequently melt unless the temperature is raised above approximately 80 °C [119]. Additionally, prolonged exposure to temperatures above the melting point degrade the mechanical stability of the agar gel formed once the temperature is lowered [120]. These temperature effects place a practical limit on the number and duration of alternating vortex mixing and sonication treatments that can be applied to the liquid mixture. Although alternating treatments allow a much greater number of particles to be incorporated into the

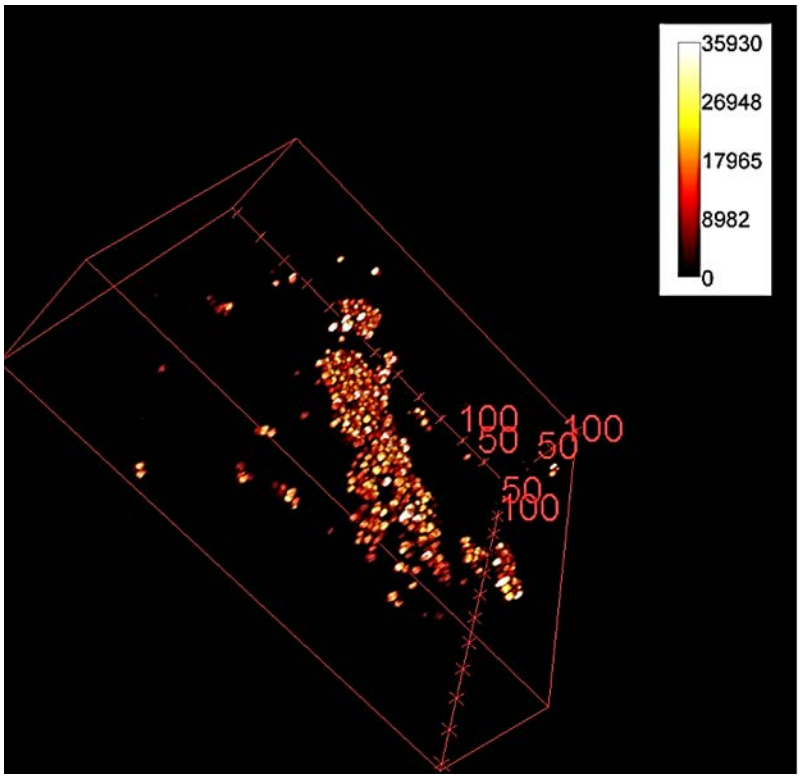

Figure 5-6. Three dimensional confocal microscopy image of TP-1 showing the surface and several micrometers into the phantom body. Crosshatches denote 50 micrometers.

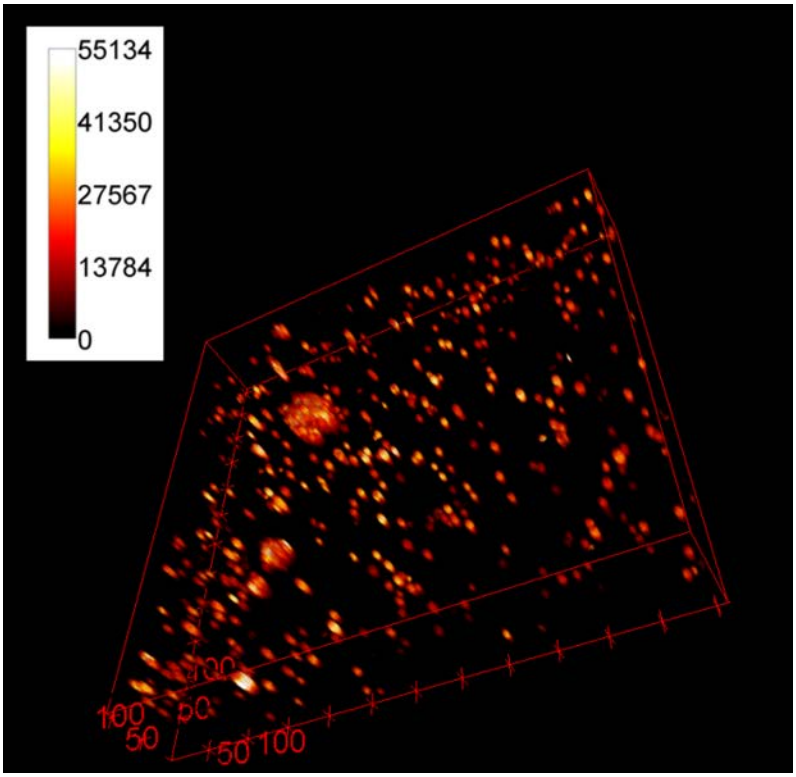

Figure 5-7. Three dimensional confocal microscopy image of TP-2 showing the surface and several micrometers into the phantom body. Crosshatches denote 50 micrometers.

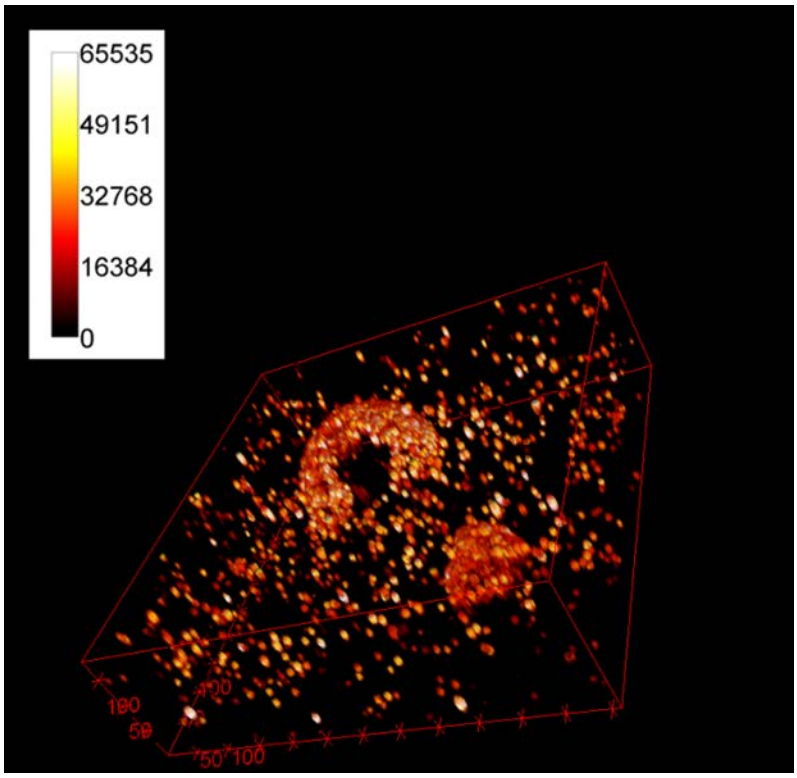

Figure 5-8. Three dimensional confocal microscopy image of TP-3 showing the surface and several micrometers into the phantom body. Crosshatches denote 50 micrometers.

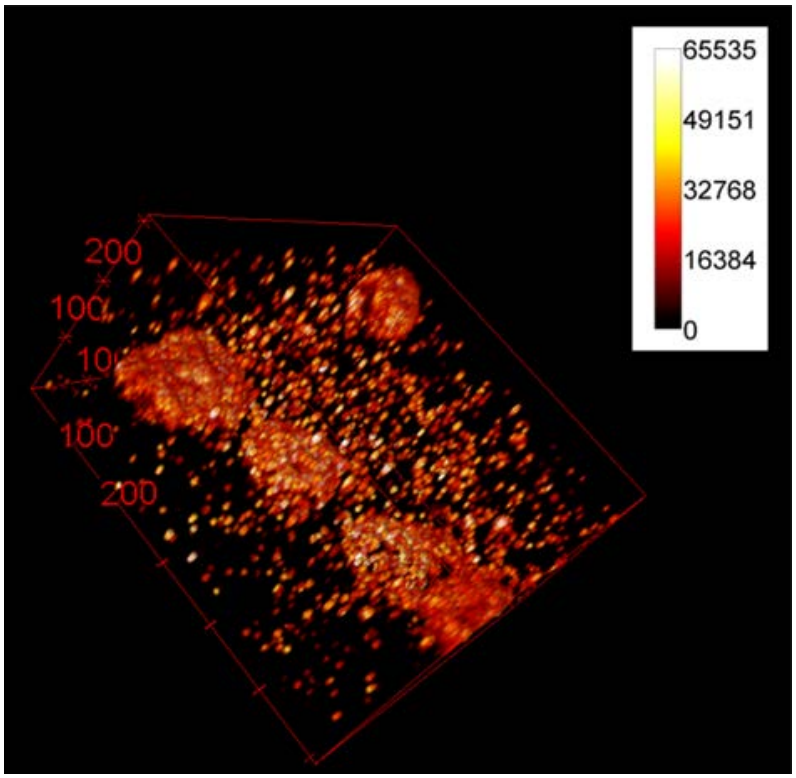

Figure 5-9. Three dimensional confocal microscopy image of TP-4 showing the surface and several micrometers into the phantom body. Crosshatches denote 100 micrometers.

phantom matrix of TP-3 and TP-4 compared to TP-1 and TP-2, the dispersal of those particles is not sufficient for building a tissue phantom library with this preparation method.

5.3.3. Particle Dispersal via Surfactant Coating

To overcome the hydrophobic nature of the outer surface of the particles without releasing the loaded molecules, loaded particles were coated with sodium dodecylsulfate (SDS), selectively solubilizing the outer surface while keeping the pores dry. Immediate vortex mixing upon addition of the particles to SDS solutions in concentrations near the critical micellar concentration, 8 mM, generated a thick foam layer that incorporated the particles and accumulated on top of the liquid [113]. This foam layer remained stable even on the time scale of months and could be reformed multiple times after resuspension in the SDS solution. The vortex mixing method is contrasted with sonication of the particles in an SDS solution which induces wetting of the pores, and subsequently, the particles in those samples sediment out of suspension (Figure 5-10).

Both the concentration of the SDS solution and the immediate initiation of vortex mixing is critical to the formation of the foam layer [113]. Surfactant concentrations higher than approximately 20 mM induce pore wetting and cause the particles to sediment. Additionally, if vortex mixing is not immediately applied to the mixture, particles in contact with the solution surface become fully wetted and sediment within a few minutes. The velocity of vortex mixing is believed to induce a kinetic effect in which the SDS molecules arrange around the mouth of the pores, and

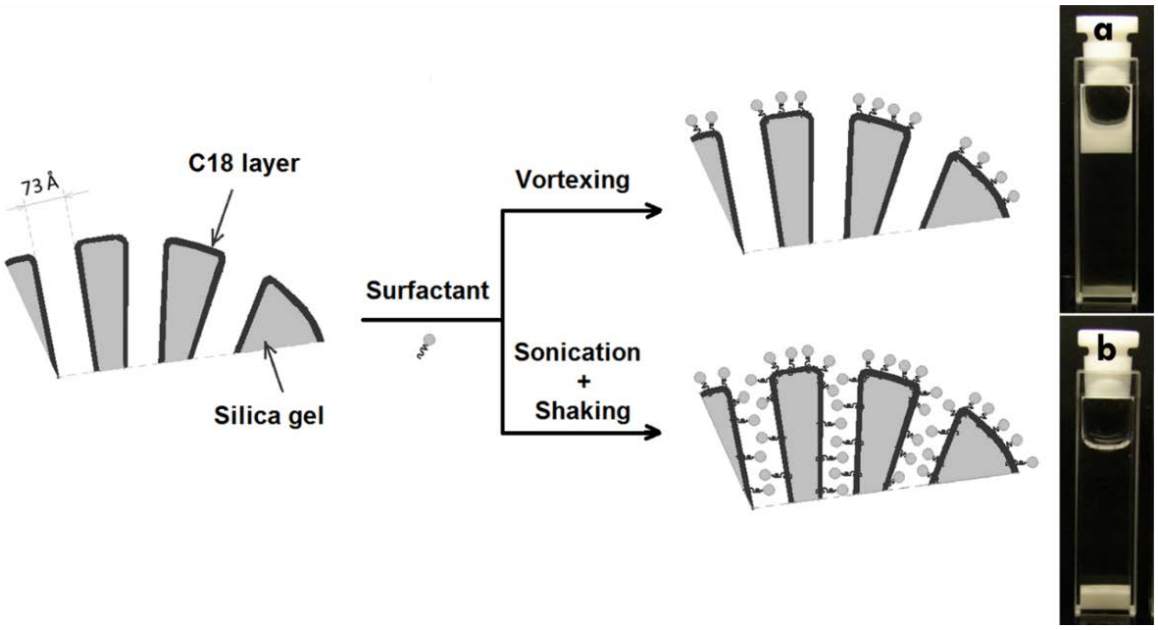

Figure 5-10. Schematic representation of the surfactant-particle interactions achieved via different treatment methods which resulted in (a) a foam layer of particles with dry pores or (b) a sedimented layer of particles with wetted pores [113].

the charged head groups generate an electrostatic repulsion barrier, preventing other SDS molecules from entering the pores. Conversely, sonication accelerates the migration of SDS molecules into the pores, inducing particle wetting very quickly.

The foam layer of R6G-loaded particles was formed with two durations of vortex mixing, 10 and 30 minutes, as a preliminary investigation of the effect of vortex mixing time on the extent of SDS-coating. Visually, the resulting foam layers were indistinguishable. Both were semi-rigid which necessitated resuspension into a small volume of SDS solution for quantitative transfer to the agar solution. Upon introducing the foam suspension to the agar solution, the particles appeared to disperse throughout the solution quickly without remaining at the solution surface or aggregating within the bulk solution. The surfactant molecules interact with the hydrophobic C_{18} layer on the particle surface with their hydrophobic C_{12} tail moieties while extending the charged

sulfate head groups into the aqueous phantom matrix [121], selectively solubilizing the outer surface and preventing particle aggregation. Gentle agitation by hand was sufficient to achieve visual homogeneity (Figure 5-11).

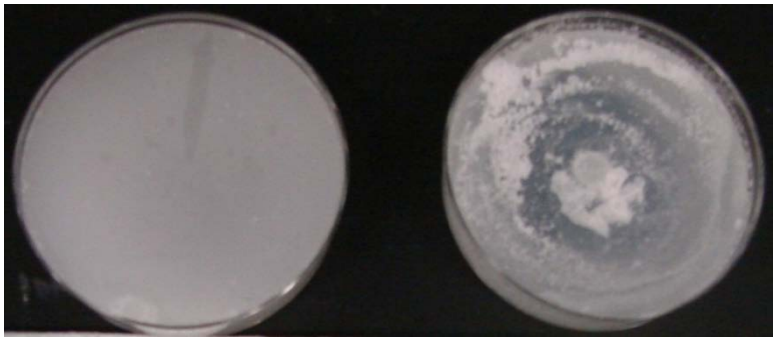

Figure 5-11. Picture of tissue phantoms generated by SDS-coating of particles (left, TP-5) versus sonication and vortex mixing (right, TP-3). Molds are 5 cm in diameter.

Confocal microscopy imaging shows that tissue phantoms generated with SDS-coated particles result in a much more uniform distribution of individual particles throughout the matrix (Figure 5-12 and Figure 5-13). However, TP-5, generated from ten minutes of vortex mixing the particles with SDS solution, still contained small aggregates of particles (Figure 5-12). Utilizing transmitted light, a visual search of the entirety of each phantom produced under TP-5 conditions revealed two to five small aggregates per phantom with each cluster containing tens of particles. Promisingly, TP-6 showed complete dispersal of individual particles throughout the phantom body (Figure 5-13). A transmitted light visual search of the tissue phantoms generated under TP-6 conditions revealed no aggregates in any sample. Qualitative observation, on both the macroscopic and microscopic levels, of TP-6 phantoms indicate that surfactant coating of C_{18} LUNA particles is an effective method for uniformly dispersing hydrophobic particles in aqueous media.

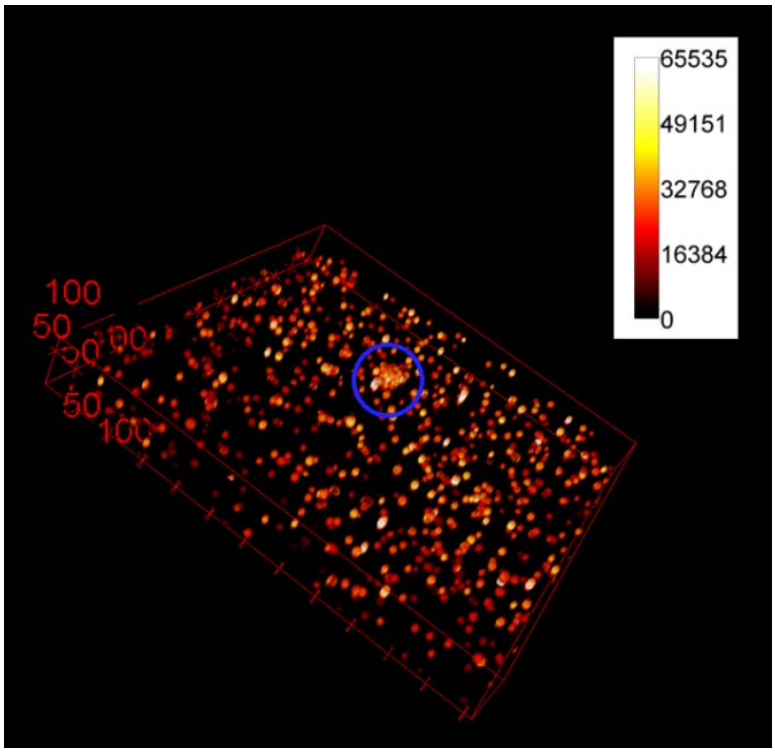

Figure 5-12. Three dimensional confocal microscopy image of TP-5 showing the surface and several micrometers into the phantom body. The blue circle indicates an aggregate. Crosshatches denote 50 micrometers.

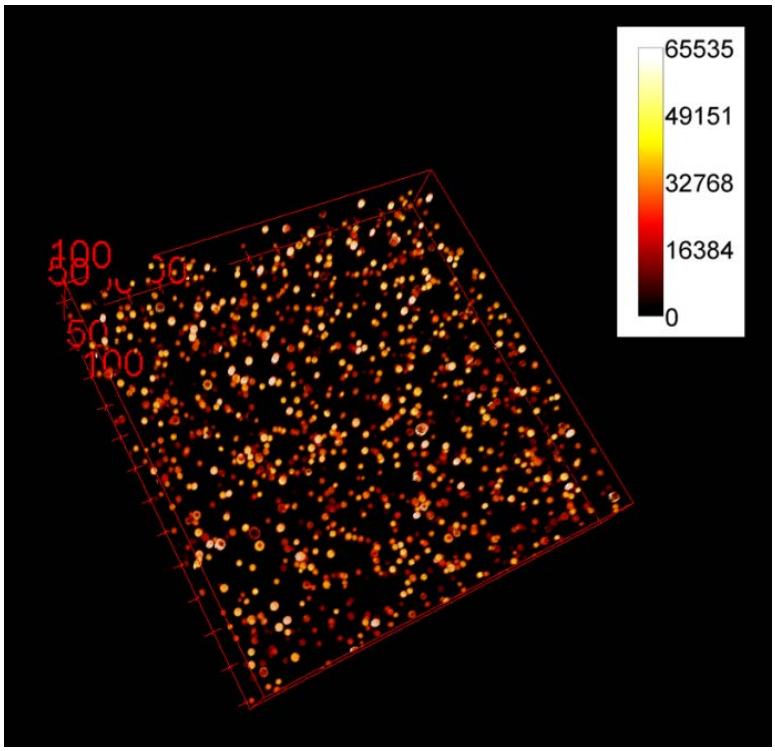

Figure 5-13. Three dimensional confocal microscopy image of TP-6 showing the surface and several micrometers into the phantom body. Crosshatches denote 50 micrometers.

5.4.Conclusions

Several preparation methods for generating tissue phantoms by dispersing hydrophobic mesoporous silica particles in aqueous agar have been investigated. Purely physical means of dispersal, sonication and vortex mixing, did not sufficiently incorporate and disperse particles throughout the phantom body. However, using a surfactant to selectively solubilize the outer layer of the particles using a surfactant allows for simple and, by visual examination, complete dispersal of the particles while maintaining the hydrophobicity of the pores. Consequently, loaded molecules are retained within the particles and the optical boundary between the particle and the suspension medium is maintained. Therefore, the surfactant coating preparation method enables the further development of hydrophobic mesoporous silica particles for constructing tissue phantoms loaded with endogenous cellular fluorophores for disease simulation and instrument calibration.

CHAPTER 6: DEVELOPMENT OF AN EXTENT OF CLUSTERING FACTOR FOR THE ANALYSIS OF PARTICLE DISPERSAL IN TISSUE PHANTOMS

6.1. Particle Dispersal

Particle dispersal is of primary concern for many particle compositions and applications. Clustering of particle substrates can prevent even or complete surface modification due to reduced contact with the synthesis solvent, and in the case of tissue phantoms, particle aggregation can contribute to wide variability in the detected signal based on sampling location within the phantom. Because tissue phantoms are designed to mimic one particular state in the progression of a disease, uniformity throughout the material is essential for providing a reference point for comparison against a real tissue sample.

Although a visual analysis of tissue phantoms produced with various techniques has indicated a reliable preparation method, a quantitative assessment is necessary to evaluate each phantom and lend weight to the distinction between images of clustered and dispersed particles. The ideal assessment would provide an indicator of clustering that is clear and without exceptions. Several analysis methods were investigated for their potential to yield a statistical distinction between clustered and dispersed systems.

6.2. Methods

6.2.1. Space Correlation Analysis

Using ImageJ software (National Institutes of Health), confocal microscopy images were converted to text images, 1024 x 1024 matrices composed of pixel

intensities (pixel length = 0.596 µm). Using MATLAB software (MathWorks), images were divided into 100 x 100 pixel sections, and ten sections along the diagonal from pixel coordinates 1, 1 to 1000, 1000 were analyzed with the space correlation function (SCF)

$$g(r) = k\langle\sum_i [I(p_i) * I(p_i + r)]\rangle \qquad \textit{Equation 6-1}$$

where k is a normalization factor, $I(p_i)$ is the fluorescence intensity of the pixel p_i, and $I(p_i + r)$ is the fluorescence intensity of a pixel at a distance r from p_i. The SCF function returns the probability of finding a pixel of high intensity at a distance r from a pixel of interest, summed over all pixels. The MATLAB code used for SCF analysis can be found in Appendix A. Output is a 5 column matrix 'G' in which

- column 1 is the integer distance, in pixels, between two pixel points
- column 2 is a count of the number of pixel pairs analyzed at that distance
- column 3 is the sum of the intensity products of each pixel pair at that distance
- column 4 is the average intensity product per pixel pair at that distance and
- column 5 is the normalized space correlation function.

6.2.2. Defining Particles in Images

Using ImageJ software, confocal microscopy images were converted to binary black and white images by thresholding; intensities at least 5 times the noise level were defined as 100 percent intensity, black, and lower intensities were defined as 0 percent, white. Particles with "loop"-style fluorescence labeling were filled using the Fill Holes function (Process menu, Binary submenu). Particles in contact with other particles were separated using the Watershed function (Process menu, Binary submenu). Particles

were defined using the Analyze Particles function (Analyze menu) using a size range of 100-1000 pixel units and circularity measure of 0.50-1.00. Output measurements of Center of Mass (x- and y-coordinates) and Feret's Diameter were saved as a text file in a three-column matrix.

6.2.3. Pair Correlation Analysis

Using MATLAB software, the center of mass coordinates of the defined particles were analyzed with the pair correlation function (PCF)

$$g(r) = k\langle \sum_i \sum_j \delta(r - r_{ij}) \rangle \qquad \textit{Equation 6-2}$$

where k is a normalization factor and r_{ij} is the distance between two particles i and j. The PCF function returns the probability of finding another particle at a distance r from a particle of interest, summed over all particles. MATLAB code used for PCF analysis can be found in Appendix B. Output is a 3 column matrix 'G' in which

- column 1 is the distance, in pixels, between two particle centers
- column 2 is the number of particle pairs at that distance
- column 3 is the normalized pair correlation function

6.2.4. Particle Dispersal Simulations

Using MATLAB software, simulation images were generated with particles of uniform radii and particles of Gaussian distributed radii with relative standard deviations ranging from 0.1 to 15 percent. The MATLAB code used to generate Gaussian distributed radii can be found in Appendix C. A variety of particle dispersal patterns were simulated ranging from randomly dispersed to entirely clustered, including arrangements in a single line, multiple small clusters, and mixed systems of some clusters and some

dispersed particles (Table 6-1). Randomly dispersed particles were placed by defining the x- and y- coordinates of the particle centers with random number generation. Particles with center coordinates closer than the sum of their two radii were removed. All simulations were generated 10 times.The MATLAB code used to generate randomly dispersed particles can be found in Appendix D. The MATLAB code used to generate clusters via the MATLAB optimization toolbox can be found in Appendix E. The MATLAB code used to randomly place multiple clusters can be found in Appendix F.

Table 6-1. Particle characteristics of each simulation generated for PCF/EC analysis.

Total Number of Particles	RSD of Particle Radii (%)	Number of Randomly Dispersed Particles	Number of Clusters	Number of Particles per Cluster
50	-	50	-	-
50	-	-	1 (line)	50
50	-	-	1	50
50	-	-	2	25
50	-	-	5	10
50	-	25	1	25
50	-	40	1	10
100	-	100	-	-
100	-	-	10	10
50	10	-	1 (line)	50
50	10	-	1	50
50	10	-	2	25
50	10	-	5	10
50	0.1	-	1	50
50	0.5	-	1	50
50	1	-	1	50
50	2.5	-	1	50
50	5	-	1	50
50	15	-	1	50

6.2.5. Extent of Clustering Analysis

Two features of the histogram of inter-particle distances (PCF matrix, column 2), the self-correlation peak (SCP) and the nearest neighbor peak (NNP), were used to develop the extent of clustering (EC) value. First, an experimentally determined ratio (R_{exp}) was calculated by

$$R_{exp} = I_1/I_0 \qquad \textit{Equation 6-3}$$

where I_1 is the integration of the NNP and I_0 is the integration of the SCP. Next, the maximum ratio (R_{max}) available to the system was calculated by

$$R_{max} = (6I_0 - 12n - 6)/I_o \qquad \textit{Equation 6-4}$$

where I_0 is the integration of the NNP and n is the number of shells – layers of hexagonally close packed particles surrounding a central particle in a cluster. The number of shells (n) is related to the number of particles in the system (N_p) by

$$N_p = 1 + 3n(n+1) \qquad \textit{Equation 6-5}$$

Finally, the EC value was calculated by

$$EC = R_{exp}/R_{max} \qquad \textit{Equation 6-6}$$

Output is a single value.

6.2.6. Coefficient of Clustering Analysis

Using MATLAB software, images were divided into 25 equal sections. The number of particles with a center of mass in each section was tallied, and the coefficient of clustering (CC) value was determined by

$$CC = s^2/\bar{x} \qquad \textit{Equation 6-7}$$

where s is the standard deviation of the number of particles in each section and $\bar{x}$ is the average number of particles in each section. The MATLAB code used for CC analysis can be found in Appendix G. Output is a single value.

6.3.Results and Discussion

6.3.1. Space Correlation Analysis

Due to the required input of intensity data, the space correlation function was an attractive method for analyzing particle clustering in confocal microscopy images using the raw fluorescence signal without the need for preprocessing the image. However, due to the large number of pixel-to-pixel calculations required to generate a SCF for the entire 1024x1024 pixel image, ten representative sections of each image – with dimensions 100x100 pixels – were selected along the diagonal from pixel coordinate 1,1 to pixel coordinate 1000,1000. The individual SCFs for each section were summed to provide a representative SCF for the image.

The selected sections of an image of TP-1 display a variety of particle dispersals (Figure 6-1). The first section (inset denoted by the blue circle) contains several particles separated by agar. The next five sections show particles in varying degrees of clustering, and the last four sections contain no particles or only partial particles (magenta crosshatches). The SCF corresponding to the dispersed particles (blue circles) displays two particular features. The first feature is the self-correlation peak, which has a width approximately equal to the particle radii; the full-width half-maximum value of the self-correlation peak is approximately 8 pixels or 4.5 µm. C18 LUNA particles have radii of approximately 5 µm conforming well to the self-correlation peak width. The second

feature of the dispersed particle SCF is the peaks that appear at distances of approximately 25, 40, and 50 pixels. These longer distance peaks appear at positions that correspond to the inter-particle distances.

Clustered particles introduce additional features to the SCF. The SCF of image sections that only contain clustered particles (red, black, and magenta circles) display an indicator of clustering in the advent of a shoulder on the self-correlation peak. The shoulder center is at approximately 16 pixels, corresponding to a two-radius distance between particles within a cluster. The SCF of image sections that contain both clustered and individual particles (green circles and blue crosshatches) display features of both dispersed and clustered SCFs with a shoulder on the self-correlation peak and peaks at longer distances.

Image sections that contain no particles (red, black, magenta, and green crosshatches) generate SCFs that display a different set of features. These sections only contain background signal, and the background has random variation and low signal intensity. Therefore, the SCF self-correlation peaks are much narrower, and no peaks appear at longer distances.

Due to the variety of particle dispersal patterns in the component sections of the TP-1 image, the sum of all ten section SCFs (black squares) shows a general smoothing effect. The self-correlation peak is still clearly distinguished. However, both the shoulder – indicative of clustered particles – and the longer distance peaks – indicative of individually dispersed particles – show diminished definition.

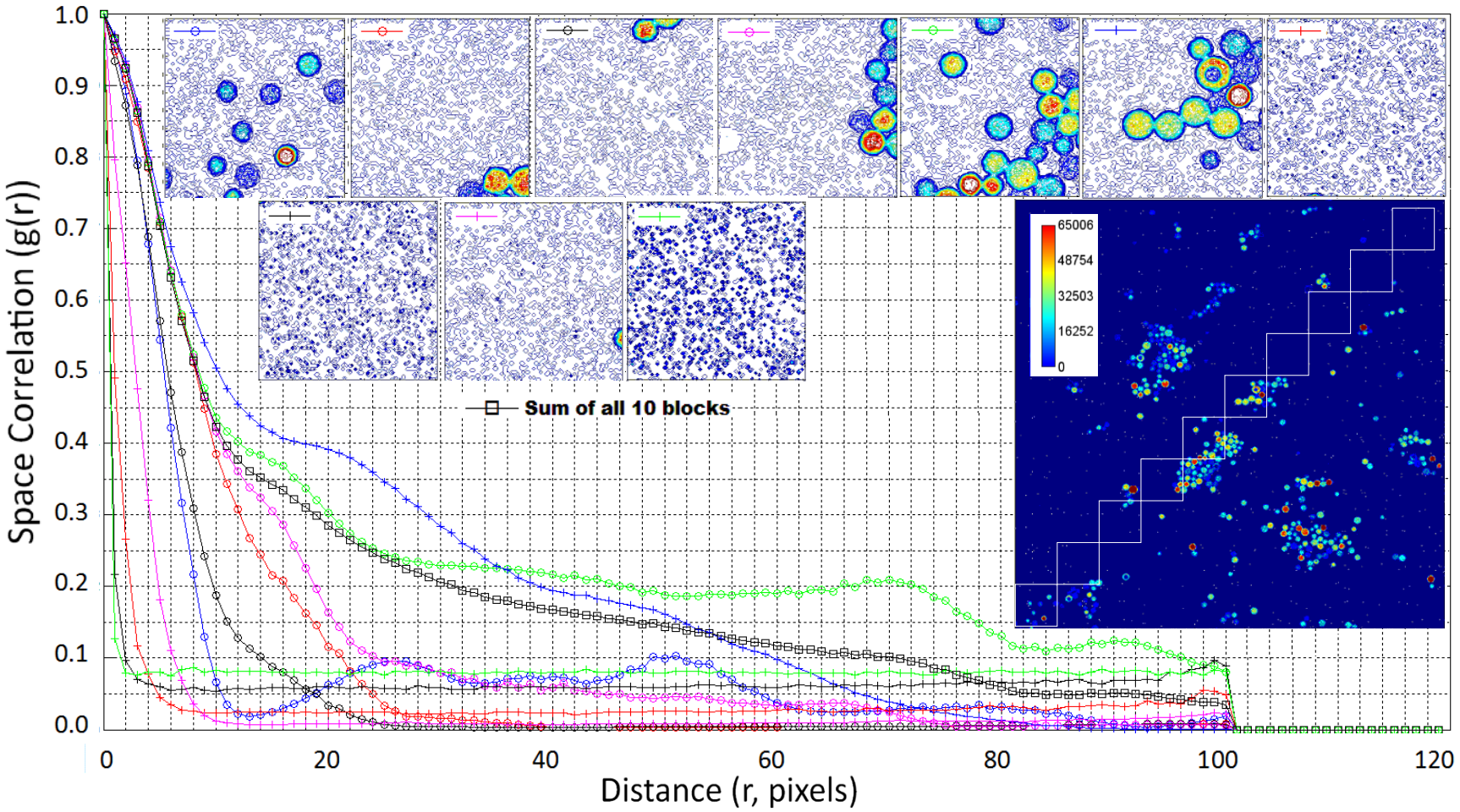

Figure 6-1. Space correlation results of selected 100x100 pixel sections (small inserts, topographical) of a confocal microscopy image of TP-1. X-axis grid lines denote 2 pixels. Sections were selected along the diagonal of the original image as indicated by the white boxes (large insert). Original image dimensions are 610.30x610.30 µm and 1024x1024 pixels (1 pixel = 0.596 µm).

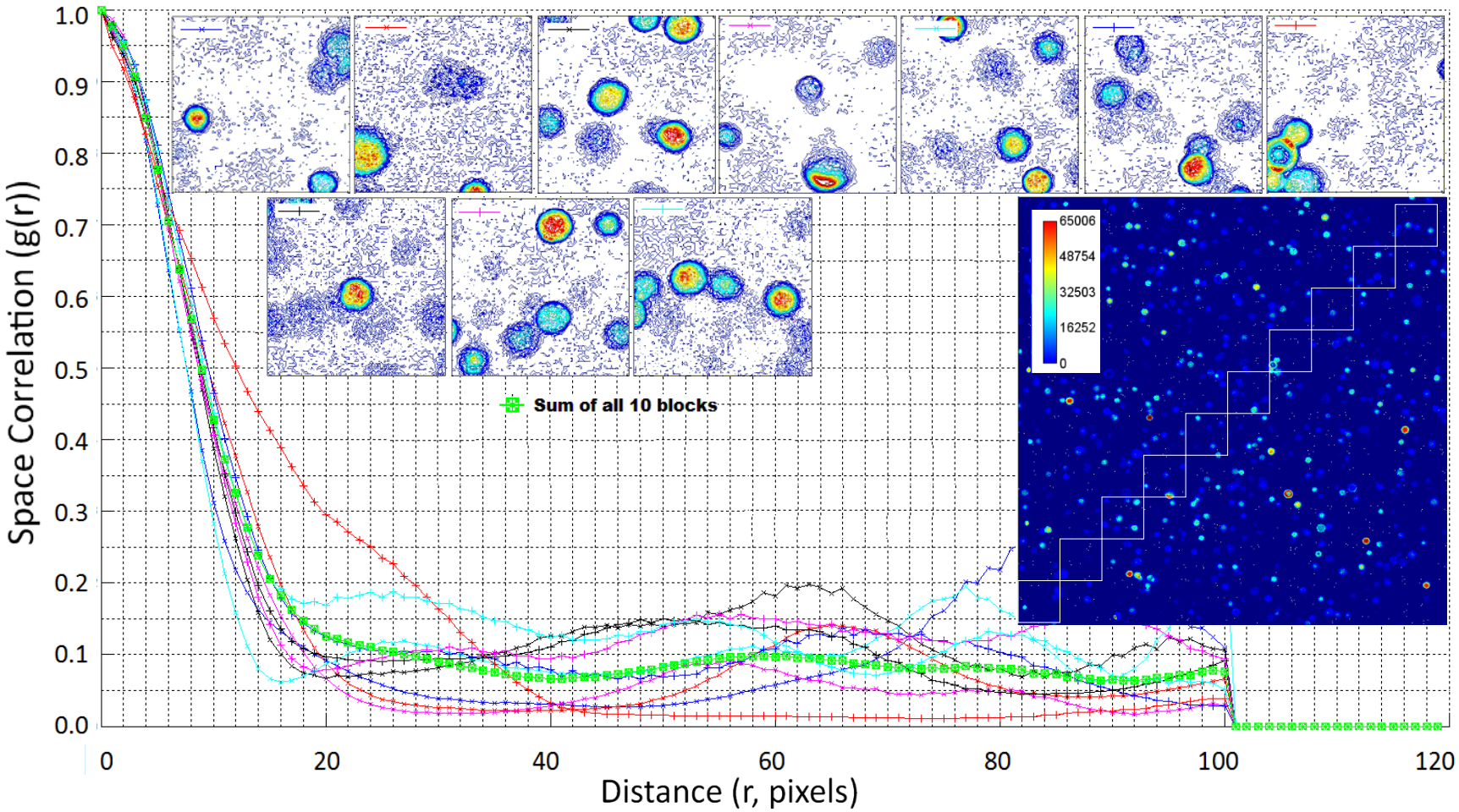

Figure 6-2. Space correlation results of selected 100x100 pixel sections (small inserts, topographical) of a confocal microscopy image of TP-1. Sections were selected along the diagonal of the original image as indicated by the white boxes (large insert). Original image dimensions are 610.30x610.30 µm and 1024x1024 pixels (1 pixel = 0.596 µm).

In contrast to the wide variation among sections for the TP-1 image, each of the sections of the TP-6 image contain at least one full particle (Figure 6-2). The majority of sections show dispersed particles; only a few sections display particles in close proximity; and only one section contains particles that are clearly in contact (red crosshatches). Correspondingly, each SCF contains a self-correlation peak with a width of approximately 8 pixels and peaks at longer distances denoting inter-particle distances. The section containing clustered particles (red crosshatches) shows a shoulder on the self-correlation peak that is indicative of clustering. Again here, the sum of all ten section SCFs (green squares) shows the self-correlation peak with a smoothed set of peaks at longer distances due to the variations in inter-particle distances among the sections.

While space correlation analysis of tissue phantom images is attractive because image pre-processing is not necessary, the SCF has several disadvantages. Most importantly, the feature that is characteristic of clustering – the shoulder on the self-correlation peak – is somewhat obscured by the self-correlation peak, particularly for images that contain both clustered and dispersed particles. Additionally, the calculation is incredibly time consuming. The calculation of the SCF for a 100x100 pixel section requires approximately 260 seconds (almost 4.5 minutes). Due to the nested 'for' loops in the calculation code (Appendix A), image analysis time (t_{SCF}) of larger sections can be estimated by

$$t_{SCF} = \left(\frac{dim}{100}\right)^4 \cdot 260\ seconds \qquad \textit{Equation 6-8}$$

where dim is the dimension of the image in pixels. Consequently, the SCF a full 1024x1024 pixel image would require more than 30 days. Furthermore, while dividing the image into smaller sections reduces the analysis time, sectioning the image also limits the range of inter-particle distances that can be observed. For less populated images, smaller sections may not provide the necessary size to observe representative inter-particle distances.

6.3.2. Defining Particles in Images

In order to improve upon the space correlation analysis, two strategies were devised. First, thresholding the image background to a flat, zero intensity could eliminate the self-correlation peak for background-background pixel pairs. Second, reducing the particle to a single point defined by its center would eliminate the width of the self-correlation peak, allowing nearest neighbor distances in clustered systems to appear as a self-contained peak instead of a shoulder on the self-correlation peak.

Using ImageJ software, images were thresholded at 5 times the noise level with everything below the threshold defined as white and everything at and above the threshold defined as black. At this threshold level, some clustered particles were not completely separated. In order to allow the Analyze Particles algorithm to identify individual particles, clustered particles were separated using the Watershed function. The Watershed function generated a pixel-wide barrier of background along "watershed" lines – where irregularities in the outline of a shape, such as a cluster of particles, would allow incursions, similar to the way a crack in a rock would allow water

to erode and widen the crack. Subsequently, loop-style labeled particles were filled using the Fill Holes function.

The Analyze Particles function was then used to identify particles. Size and circularity parameters were defined to exclude minute areas of high intensity and particles on the edges as well as prevent any clusters not separated by the watershed function from being defined as single particles. This method of defining particles included some errors – some clusters were not fully separated and some loop-style labeled particles were irreversibly fragmented by the Watershed function (Figure 6-3). However, in comparison with the number of particles identified manually, this more automated method identified greater than 98% of the same particles. Moreover, the processing time required to identify particles was significantly reduced versus manual selection.

6.3.3. Pair Correlation Analysis

Upon thresholding the background to a value of 0 and defining particles by their center of mass (essentially defining the pixel coordinates with a value of 1), the space correlation function simplifies to the pair correlation function. This is because all pixel pair intensity products are either 0 – for pixel pairs of which at least one is a background pixel – or 1 – for pixel pairs which include two particle centers. It is, therefore, unnecessary to include any background pixels in the analysis, and an entire image can be analyzed without sectioning because the calculation is reduced to include only particle-particle pairs.

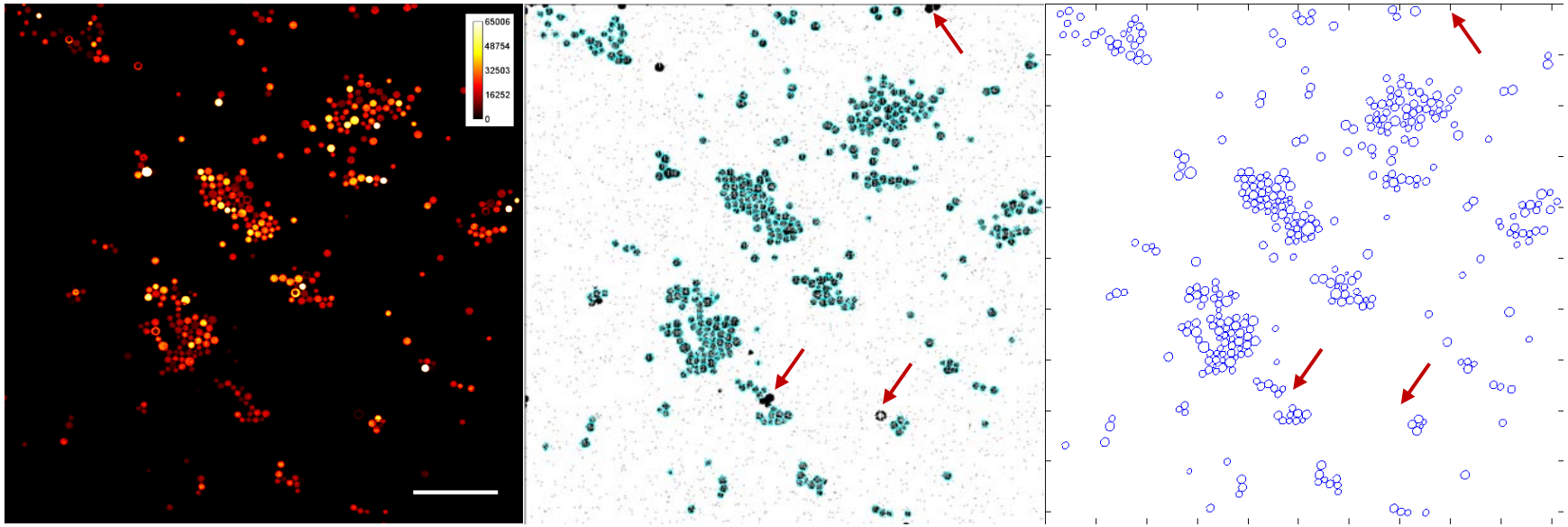

Figure 6-3. Confocal microscopy image of TP-1 (left, scale bar denotes 100 µm = 168 pixels), image showing analyzed particles after thresholding and watershedding in ImageJ (middle), and image transferred to MATLAB for analysis (right). Arrows indicate excluded particles.

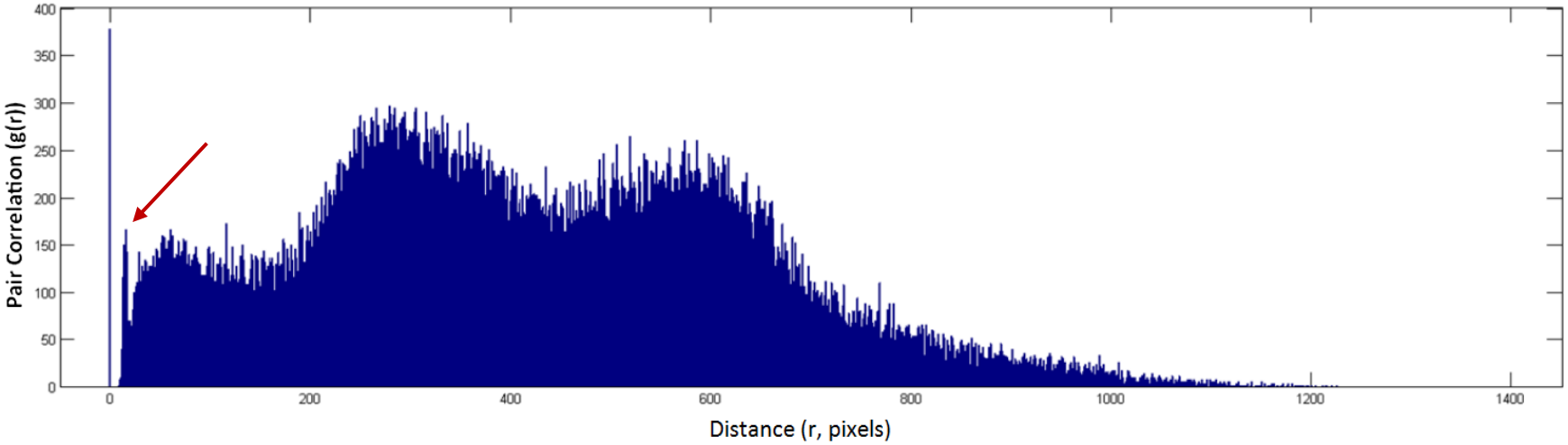

Figure 6-4. Pair correlation function of TP-1. Arrow indicates nearest neighbor peak (NNP). 1 pixel = 0.596 µm.

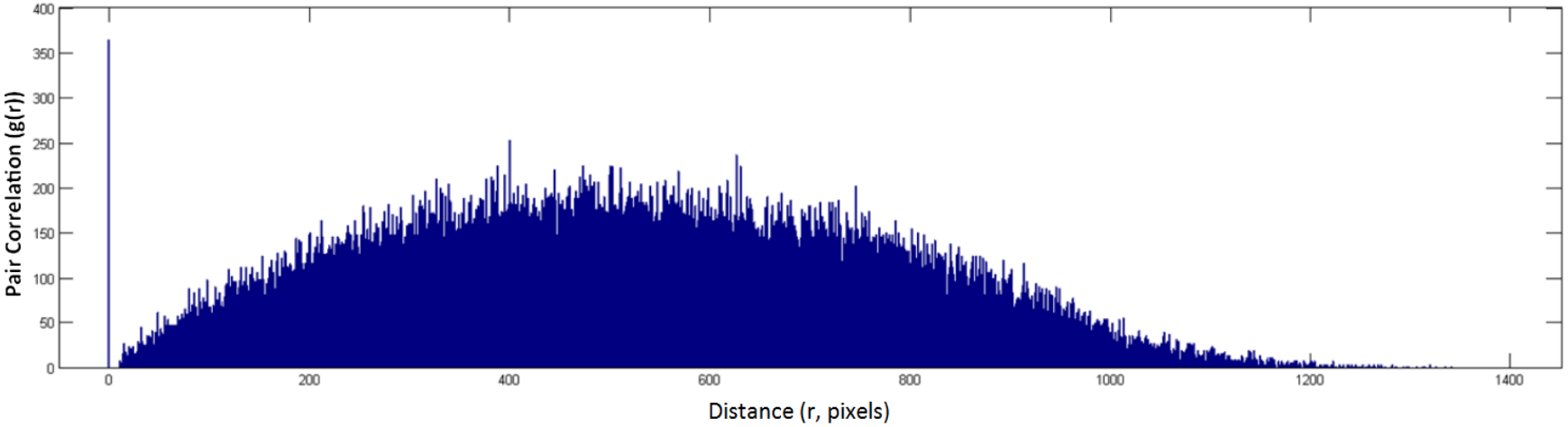

Figure 6-5. Pair correlation function of TP-6. 1 pixel = 0.596 µm.

The non-normalized pair correlation function of TP-1 (Figure 6-4) shows a self-correlation peak at a distance of zero. The PCF self-correlation peak is infinitely narrow, and the integration is equal to the number of particles analyzed ($I_0 = N_p$). Importantly, the feature indicative of clustering – which, for the SCF, was a poorly defined shoulder on the self-correlation peak – is clearly distinguished from the self-correlation peak (Figure 6-4, red arrow). This feature is termed the nearest neighbor peak (NNP) and appears at the distance of two radii. The PCF of TP-1 also displays peaks at longer distances indicative of multiple clusters located at various positions in the image.

The pair correlation function of TP-6 (Figure 6-5) also shows a self-correlation peak. However, where several peaks can be identified in the PCF of the clustered particles in TP-1, the dispersed particles in TP-6 result in a single broad peak across a large range of inter-particle distances.

6.3.4. Particle Dispersal Simulations

The applicability of the pair correlation function to the phantom images utilizing characteristic features was established via simulations of images with particles of uniform radii (Figures 6-6 and 6-7). All systems which include clustered particles provides a clear indication of that clustering via the nearest-neighbor peak (NNP), which appears at the distance of two radii. For a system of randomly dispersed particles (Figure 6-6 top), the PCF displays a broad peak over a large range of inter-particle distances. Mixed systems of clustered and randomly distributed particles generate a PCF that displays the features of both arrangements (Figure 6-7, bottom), an NNP and a broad peak. Additionally, for system with multiple clusters (Figure 6-7 top and middle),

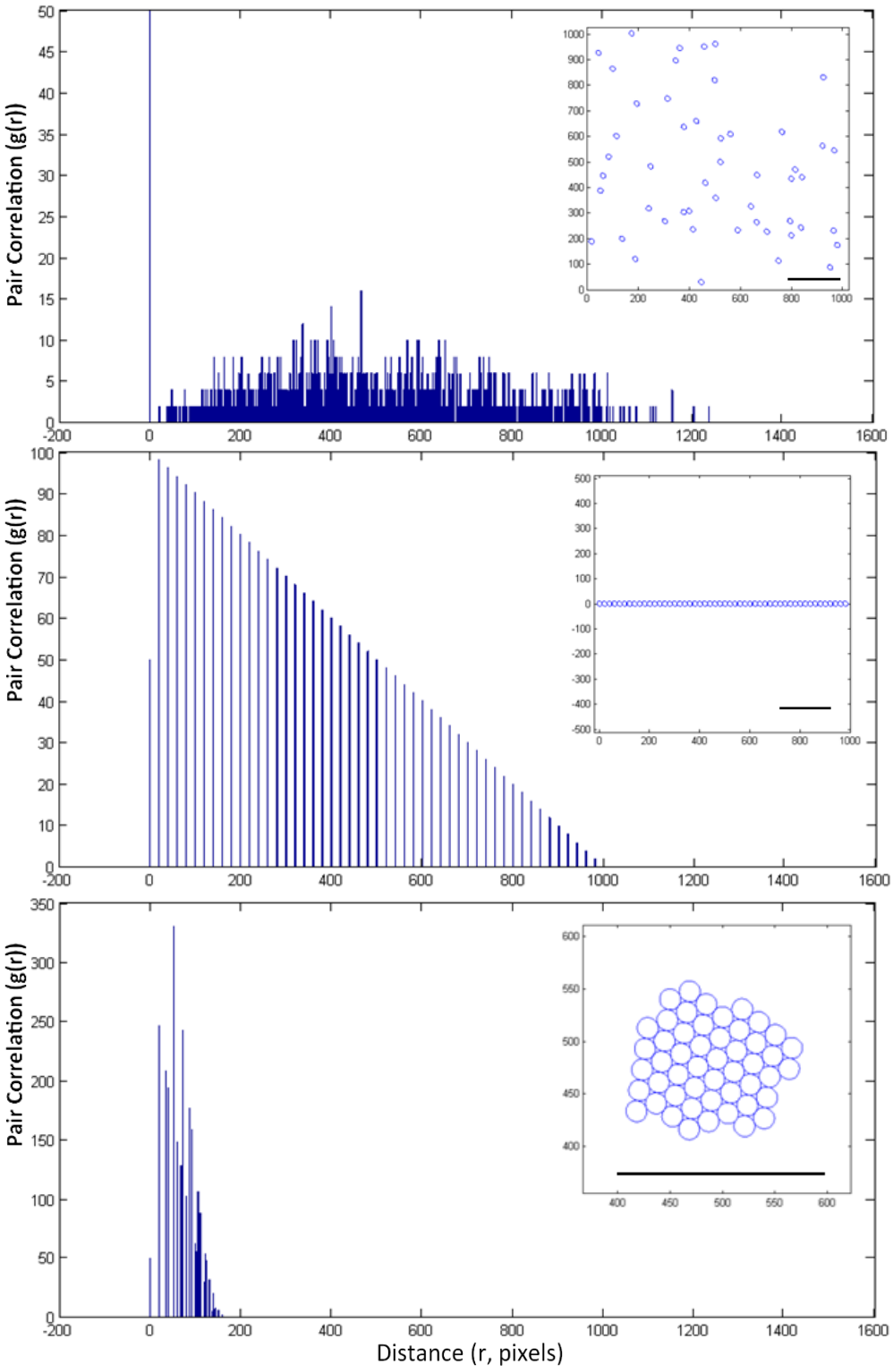

Figure 6-6. Pair correlation functions for randomly dispersed (top), lined up (middle), and clustered (bottom) particles. Scale bars denote 200 pixels (120 µm).

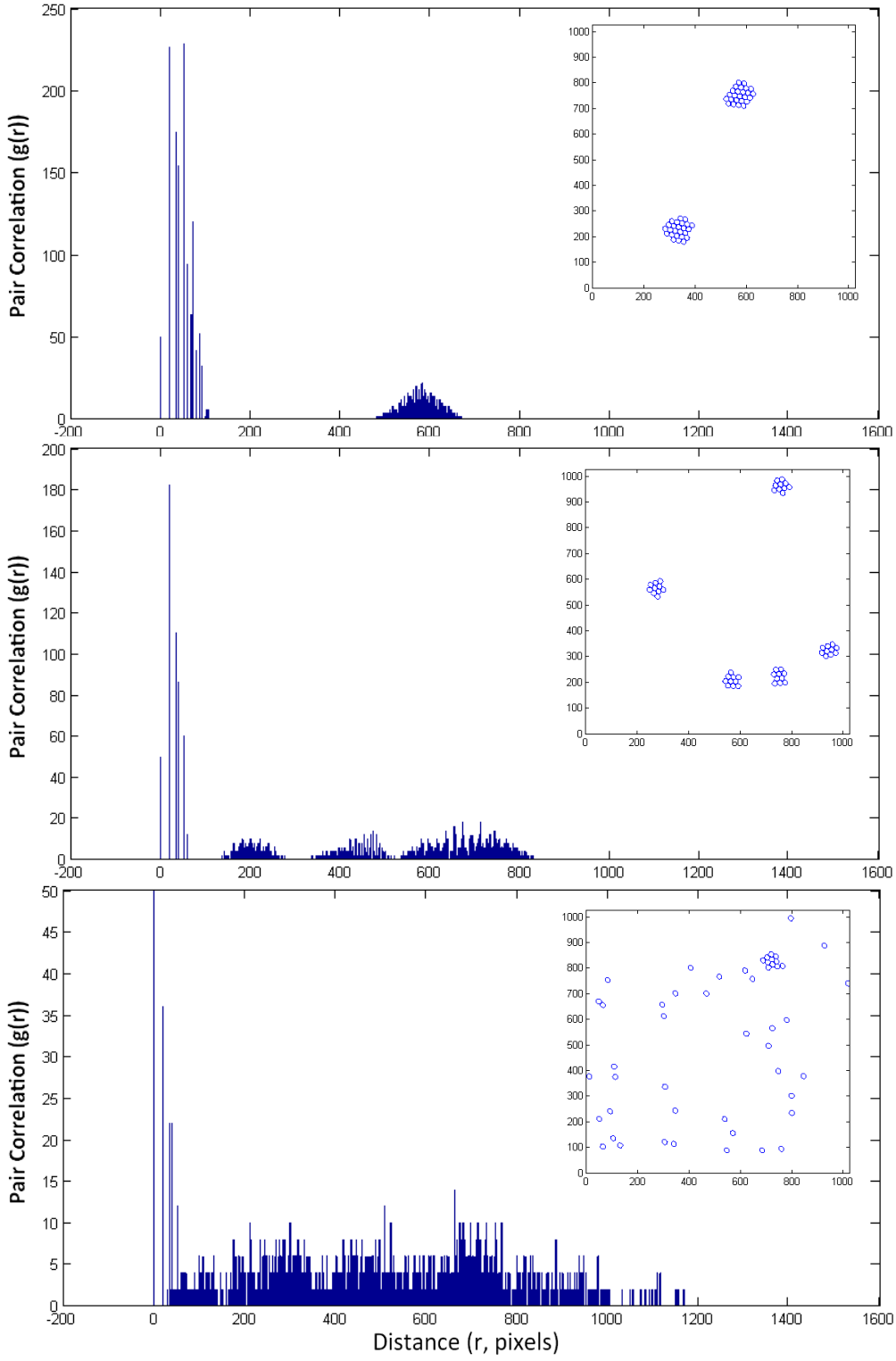

Figure 6-7. Pair correlation functions for multiple clusters – 2 clusters of 25 particles (top) and 5 clusters of 10 particles (middle) – and a mixed system of a single cluster of 10 particles with 40 randomly dispersed particles (bottom). Simulated images are 1024x1024 pixels (610.3x610.3 µm).

localized peaks at long distances are observed. The number of long distance peaks (N_{ldp}) can be predicted by

$$N_{ldp} \leq N_c(N_c - 1)/2 \qquad \textit{Equation 6-9}$$

where N_c is the number of clusters.

The simulations of clustered systems also demonstrated that the NNP is sensitive to a range of cluster and particle characteristics. Based on the uniform radii simulations, it was determined that the integration of the NNP is indicative of both number of clustered particles and the morphology of the cluster. Higher numbers of particles included in the cluster translate to a larger NNP integration (comparison among Figure 6-6 bottom, Figure 6-7 top, and Figure 6-7 middle); and more tightly packed clusters translate to a larger NNP integration (comparison between Figure 6-6 middle and Figure 6-6 bottom).

Upon introducing a distribution of particle radii, the strict hexagonal close packing of clusters with uniform particle radii becomes more disordered. As a result, the NNP gains width due to the concomitant distribution of inter-particle distances within the cluster (Figure 6-8). The theoretical relationship between the relative standard deviation of the particle radii ($radii_{RSD}$) and the NNP width (w_{NNP}) is

$$w_{NNP} = {\sqrt{2}}/{5} \cdot radii_{RSD} \qquad \textit{Equation 6-10}$$

where w_{NNP} is defined as 2σ of the Gaussian fit of the NNP. The simulation data confirm this relationship (Figure 6-9). The fit line of 80 cluster simulations (50 particles each) with relative standard deviations in particle radii ranging from 0% (uniform radii)

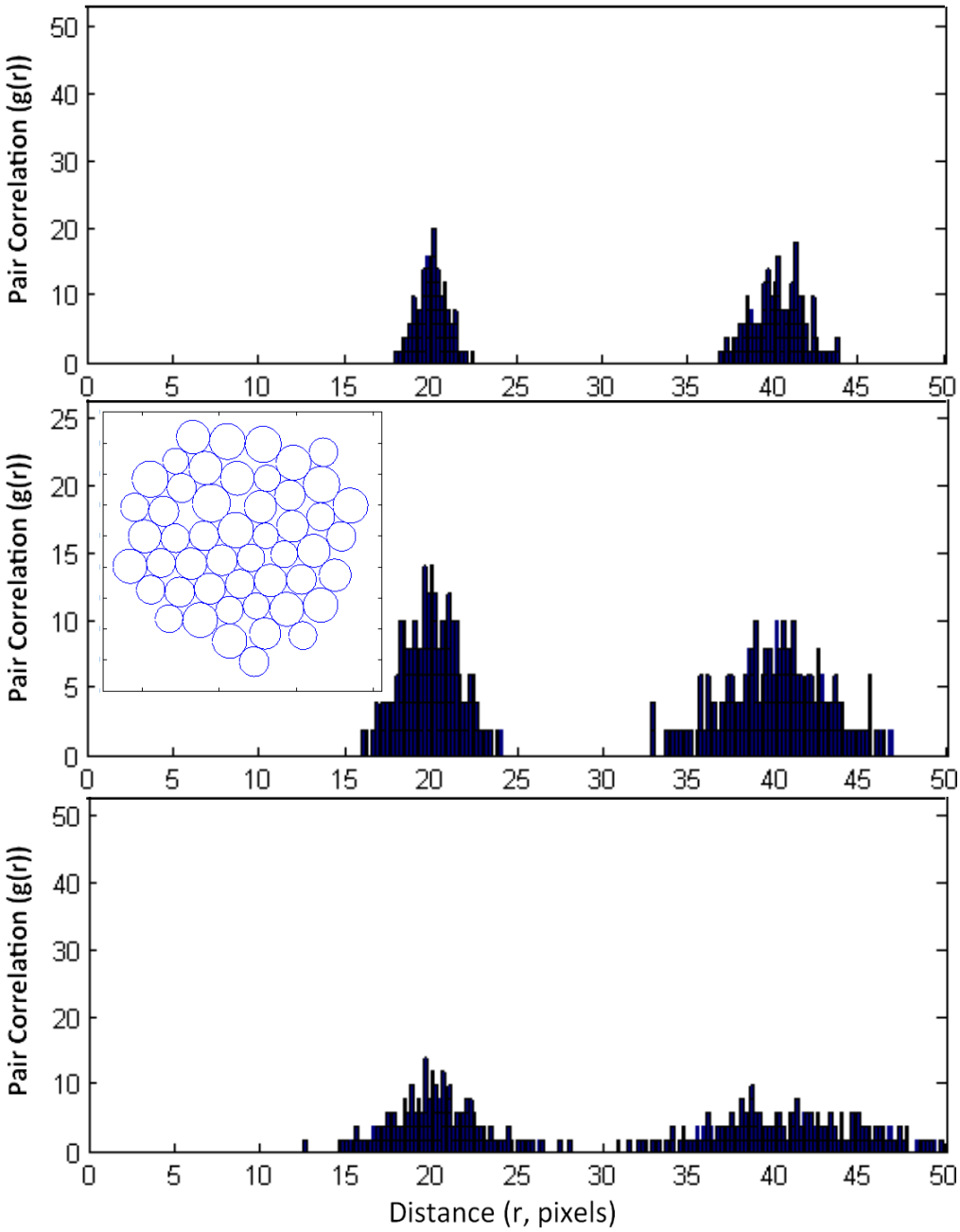

Figure 6-8. Pair correlation functions for single clusters of 50 particles with relative standard deviations in particle radii of 5% (top), 10% (middle), and 15% (bottom). Inset shows a representative cluster of 50 particles with 10% RSD in particle radii. Inset x-axis ticks indicate 50 pixels, inset y-axis ticks indicate 20 pixels.

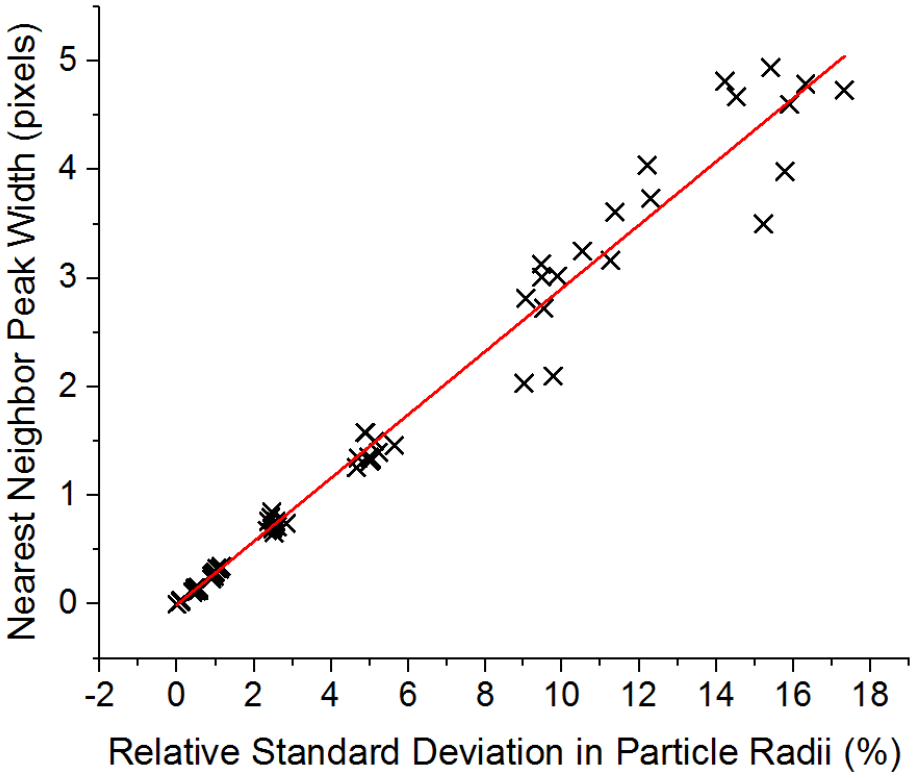

Figure 6-9. Simulation data of 50-particle clusters composed of particles with varying RSD in particle radii. NNP width determined by 2σ of Gaussian fit of NNP. Fit line (red) equation is $y = 0.291(\pm 0.005) \cdot x + 0.00(\pm 0.03)$. R^2 of fit is 0.979.

to 15% (Gaussian distributed radii). The fit line shows an insignificant intercept (0.00 ± 0.03) and a slope (0.291 ± 0.005) that is not significantly different from the theoretical slope.

6.3.5. Extent of Clustering Analysis

Given that the NNP is a clear indicator of clustering as well as the wealth of information it contains, a numerical indicator of clustering based on the NNP could provide both a concise and comprehensive gauge for a statistical comparison of images. Because the NNP integral is indicative of cluster size and morphology and comparisons among images would likely require comparisons of different numbers of particles, the first step in the development of a single numerical indicator of clustering is to normalize

the NNP integral by the total number of particles in the system. Based on the PCF, an experimentally determined ratio (R_{exp}) can be calculated by Equation 6-3. The self-correlation peak integral is equal to the number of particles in the system ($I_0 = N_p$) because this is a count of all particle pairs at a distance of 0 pixels. This R_{exp} is the same for all systems that have the same size and morphology of clusters no matter how many clusters are in the system (e.g. 5 clusters of 10 uniform particles and 10 clusters of 10 uniform particles). However, a greater degree of clustering is available to a system with more particles if all particles are in a single cluster. Therefore, in order to distinguish between two systems with different numbers of the same clusters, a maximum ratio (R_{max}) must be determined.

In the simplest case of uniform particles, the cluster would form in a hexagonally close packed arrangement. In an infinite cluster, each particle would have six nearest neighbors, and the NNP integral would be calculated by $I_1 = 6 \cdot I_0$ and $R_{exp} = R_{max} = I_1/I_0 = 6$. However, discrete clusters have edge particles that do not have 6 nearest neighbors. The every shell around a central particle has 6 "vertex" particles that have 3 nearest neighbors. The first shell only has vertices, but subsequent shells also have "side" particles that have 4 nearest neighbors.

Additionally, with every subsequent shell, the previous shell becomes "inner" particles that have 6 nearest neighbors. A summary of these relationships is presented in Table 6-2. In a hexagonally close packed cluster, the relationship between N_p and the number of shells (n) around a central particle is given by Equation 6-5. Also shown in

Table 6-2 is the numerical relationship among I_1, I_0, and n. This relationship can be simplified to

$$I_1 = 6I_0 - 12n - 6 \qquad \textit{Equation 6-11}$$

and substituting I_1 in the R_{max} calculation yields Equation 6-4. After both R_{exp} and R_{max} are known for a system, an extent of clustering (EC) value can be determined by Equation 6-6.

Table 6-2. Summary of particle locations and nearest neighbor interactions in hexagonally close packed clusters of different sizes.

Shell (n)	$N_p = I_0$	Inner	Vertex	Side	I_1	R_{max}
0	1	0	0	0	0	0
1	7	1	6	0	24	3.429
2	19	7	6	6	84	4.421
3	37	19	6	12	180	4.865

This novel numerical indicator of clustering has several advantageous characteristics. First, because the value is normalized by both the number of particles in the system and the maximum clustering available to the system, comparisons can be made across systems with different numbers of particles. Second, the EC value has theoretical limits; the lower bound is zero for a completely uniform system; randomly dispersed systems have EC values below 0.1; and the upper bound is 1 for a fully clustered system. Additionally, subtle differences in degree of clustering yield statistically significant differences in EC values, for example, the difference between 5 clusters of 10 particles and 10 clusters of 10 particles (Table 6-3) have, statistically, very significant differences in their EC values (0.727 ± 0.009 and 0.689 ± 0.006, respectively, $p < 0.0001$).

Table 6-3. Comparison of numerical indicators of clustering for uniform radii simulations and two tissue phantom images. For simulation systems, "r" denotes randomly distributed particles, "l" denotes lined up particles, and "c" denotes clustered particles. Errors indicate standard deviation of 10 trials.

System/Image	EC value	CC value
50r	0.014 ± 0.009	0.95 ± 0.04
100r	0.026 ± 0.009	0.91 ± 0.03
1x50l	0.3902	2.521
1x50c	0.98 ± 0.01	5.7 ± 0.1
2x25	0.894 ± 0.006	5.0 ± 0.3
5x10c	0.727 ± 0.009	3.9 ± 0.2
10x10c	0.689 ± 0.006	3.7 ± 0.2
1x25c + 25r	0.46 ± 0.01	3.0 ± 0.2
1x10c + 40r	0.16 ± 0.01	1.5 ± 0.2
TP-1	0.409	3.3
TP-6	0.056	0.90

6.3.6. Coefficient of Clustering Analysis

To provide an evaluation of the developed numerical analysis, the coefficient of clustering (CC) was calculated for each system via Equation 6-7. The CC value is a commonly used metric to provide an indicator of clustering in diverse contexts. Although the numerical value assigned to a system can provide a general idea of clustering, the calculation method requires a user-defined division of the data set, e.g. dividing the image into 25 equal portions. The resulting CC value is strongly dependent upon the number of divisions, particularly for clustered systems. While the CC value contains some theoretical limits – 0 for completely uniform dispersal and 1 for completely random dispersal – there is no global upper bound. Consequently, comparisons across systems with different numbers of particles or varying degrees of

clustering are limited, for example, the CC values for 5 clusters of 10 particles and 10 clusters of 10 particles (3.9 ± 0.2 and 3.7 ± 0.2, respectively) are statistically indistinguishable.

6.4.Conclusions

The pair correlation function is an information-rich analysis tool that is a significant advancement over the space correlation function for assessing dispersal of hydrophobic mesoporous silica particles in tissue phantoms. The practical considerations of analysis time is improved and sampling from within the data set is not necessary. Different particle dispersal patterns – clustered, random, and mixed systems – can be distinguishable based on characteristic features. For systems that contain even small degrees of clustering, the nearest neighbor peak provides a clear indicator of clustering. The nearest neighbor peak is sensitive to the size and morphology of clusters as well as the distribution of particle sizes. Using a combination of the self-correlation peak integral and the nearest neighbor peak integral as well as a theoretical maximum nearest neighbor peak integral enables the calculation of an extent of clustering (EC) value with bounds of 0 and 1 for the limiting cases of uniform dispersal and completely clustered. The development of this EC analysis is an improvement over the previously established use of coefficient of clustering analysis

CHAPTER 7: CONCLUSIONS AND FUTURE DIRECTIONS

7.1. Conclusions

7.1.1. MSN synthesis and drug delivery suitability

Mesoporous silica nanoparticles with sub-100 nm diameters were synthesized in two pore topologies, MCM-41 and WO. Utilizing a 1-pot synthesis method, Fe_3O_4 nanoparticle cores were successfully incorporated into WO MSNs also with sub-100 nm particle diameters. Fe_3O_4@MCM-41 MSNs were synthesized, but initial samples showed poor centralization of the Fe_3O_4 cores and subsequent variations failed to produce particles with sub-100 nm diameters. The MCM-41, WO, and Fe_3O_4@WO MSNs were loaded with doxorubicin at comparable levels per mass. However, the loading per surface area for Fe_3O_4@WO particles was significantly higher than the no-core MSNs. Korsmeyer-Peppas fits of the doxorubicin release curves indicated a diffusion controlled Fickian release mechanism with slight kinetic differences due to pore structure a much lower and slower release due to the iron oxide core. The application of a static magnetic field had very little effect on the drug release from Fe_3O_4@WO MSNs. Additionally, while all nanoparticle treatments of A549 cells induced approximately the same effect, the Fe_3O_4@WO particles induced less reduction in the cell viability of HEC50CO and CT26 cells in comparison to the no-core MSNs.

The simple synthesis, higher loading per surface area, and potential for synergistic therapy or theranostic applications of Fe_3O_4@WO MSNs make these particles attractive for further development as drug delivery systems. Furthermore, the slower

release of doxorubicin from Fe_3O_4@WO particles and lower cytotoxicity against HEC50CO and CT26 cells make these MSNs prime candidates for stimulated release studies.

7.1.2. Tissue phantom generation and analysis

Tissue phantoms generated by attempting to suspend hydrophobic C_{18} LUNA in agar gel via sonication and vortex mixing display a wide range of clustering motifs. However, selectively solubilizing the outer surface of the particles with SDS allows for significant visual dispersal in the aqueous agar gel. While space correlation analysis requires no preprocessing of phantom images before analysis, the time required for analysis of a whole image is prohibitive and smaller sections limit the usefulness of the result. Additionally, the indicative feature of clustering is obscured by the inherent width of the self-correlation peak. Consequently, shrinking the particles to a single point at their center of mass and eliminating the background is a significant advancement. Processing the image with ImageJ commands, while not perfect, produces results with high conformity to results from processing by hand. The simplified pair correlation produces an extremely information-rich output. Using the infinitely narrow self-correlation peak and the nearest neighbor peak, as well as a theoretical maximum nearest neighbor peak, a novel single numerical indicator of clustering was developed.

The extent of clustering (EC) value represents a significant advancement over another numerical indicator of clustering, the coefficient of clustering (CC) because the bounds, 0 and 1, of the EC encompass all possible conformations of particles from

uniformly dispersed through randomly dispersed, to mixed systems of dispersed and clustered particles, and all the way to a single all-inclusive cluster. While the CC has values which correspond to cases of uniform and random dispersal, the comparison of clustered systems is lacking. Additionally, the EC can distinguish between similar cluster patterns from differently populated systems. Although developed for the assessment of physical dispersal of particles in phantom images, the EC statistical value could extend beyond the natural sciences to social sciences, e.g. describing the saturation of a market or assessing resource location and distribution in a community.

7.2. Future Directions

7.2.1. MSN one-pot synthesis

The previous development of a one-pot synthesis method for Fe_3O_4@WO MSNs could be adapted to Fe_3O_4@MCM-41 as well as other core materials and pore structures to provide more facile syntheses for core-shell MSNs. Given the abundance of research investigating diverse applications of core-shell MSNs [28, 30, 49, 65], and the layering of materials on the surface to expand the multifunctionality of an individual particle [122-124], the synthetic step to achieve the starting material is sometimes a barrier to further development. A one-pot method of particle synthesis is both a desirable and achievable goal [125].

7.2.2. Stimulated drug release

Although the study of drug release from a DDS at physiological pH is a necessary component of evaluating the encapsulation efficiency, the drug delivery of a chemotherapeutic can be triggered by lower pH. Tumors, due to the enhanced

permeability and retention effect, accumulate a variety of generally undesirable conditions; large molecules and particulates from the blood, waste products; hypoxic and acidic conditions, etc [26]. Lower pH release media has been shown to enhance drug release from unmodified MSNs [126]. The difference in pH from physiological pH related to the enhancement of drug release could also provide insight into the interactions between an adsorbed drug molecule and the MSN surface.

The presence of an Fe_3O_4 core in a DDS also generates the possibility of triggering drug release via the application of an oscillating magnetic field [44]. The assessment of the enhanced release in correlation with a change in temperature due to the particle vibration could help identify the contribution of each component: temperature and physical vibration. Additionally, a combined study of pH and the application of an alternating magnetic field could define an optimal environment for stimulating drug release inside a tumor.

7.2.3. MSN surface modification

Although many studies have investigated MSNs for drug delivery applications using the bare silica surface [20, 34], modification of the surface with an amine group has been shown to reduce cytotoxicity against immune cells [56]. While negatively charged drug molecules may interact more strongly with an amine-functionalized surface, the loading of positively charged doxorubicin may be detrimentally affected.

7.2.4. Tissue phantom analysis

Optical slices of tissue phantoms imaged using a confocal microscope can be compiled into three-dimensional images. Defining a spherical region of interest rather

than simply a circular one could allow pair correlation function analysis of 3D images, providing a true center-of-mass to center-of-mass calculation of inter-particle distance rather than relying on the possibility that a single optical slice includes the true particle centers for multiple particles.

Because confocal microscopy can provide optical slices at a depth of at least 200 µm below the surface of a phantom, it is possible to assess not only overall clustering, but also gradients in particle distribution from the phantom top to bottom. Three dimensional analysis of inter-particle distances would increase the portion of the phantom analyze and reduce the possibility of sampling error which can arise when selecting a single optical slice for pair correlation analysis. Corresponding 3D simulations and 3D cluster minimization would provide a more comprehensive picture of true particle dispersal within the phantom.

Appendix A. MATLAB code for space correlation analysis

```
image=image_01;                                % define image for analysis (must be square)
bkgd=mat2str(image(1:400,300:550));                    % select section of background
avgbkgd=mean(bkgd);
stdbkgd=std(bkgd);
threshold=avgbkgd+5*stdbkgd;                                    % set threshold level

size=length(image(:,1));
imagethresh=zeroes(size,size);

for i=1:size
        for j=1:size
                if image(i,j)<=threshold
                        imagethresh(i,j,)=0          % remove background below threshold
                        else
                        imagethresh(i,j)=image(i,j);
                end
        end
end

data=imagethresh(1:100,1:100)              % select square section of thresholded image
dimension=length(data(:,1));
dsqrd=round(sqrt(2*dimension^2))+100;
G=zeros(dsqrd,5);
G(:,1)=0:1:dsqrd-1;

for i=1:dimension                                       % x-coordinate of original pixel
        for j=1:dimension                               % y-coordinate of original pixel
                for iprime=1:dimension                % x-coordinate of comparison pixel
                        for jprime=1:dimension        % y-coordinate of comparison pixel
                                delta=ceil(sqrt((i-iprime)^2+(j-jprime)^2))+1;
                                G(delta,2)=G(delta,2)+1;
                                G(delta,3)=G(delta,3)+data(i,j)*data(iprime,jprime);
                        end
                end
        end
end

for i=1:dsqrd-1                                         % account for edge effects
        if (G(i,2)-G(1,2))*(G(i+1,2)-G(1,2))<0
```

```
                icount=i
        end
end

for k=1:icount
        G(k,4)=G(k,3)/G(k,2);
end

for m=1:icount
        G(m,5)=G(m,4)/max(G(:,4));
end

data_image_0=data;                                  % define to save
G_image_0=G;                                        % define to save
```

Appendix B. MATLAB code for pair correlation analysis

```
Locations=image_particles_01;                          % select particle coordinates matrix
n=length(Location(:,1))                                % identify number of particles
D=zeros(n^2,1);

for i=1:n
        a=Locations(:,1)-Locations(i,1)*ones(n,1);     % calculate x-coordinate distances
        b=Locations(:,2)-Locations(i,2)*ones(n,1);     % calculate y-coordinate distances
        distance=sqrt(a.^2+b.^2);                      % calculate inter-particle distances
        D((i-1)*n+1:i*n)=distance;                     % record all inter-particle distances
end

HistD= histc(D,[0:1:1449]);                            % histogram inter-particle distances
G=zeros(length(HistD),3);
G(:,1)=[0:1:1449];                                     % match to bin size of histogram
G(:,2)=HistD;
G(:,3)=HistD/n;
G_01=G;                                                % define to save
```

Appendix C. MATLAB code for Gaussian distributed radii

```
avg_rad=8;                                  % set average radius in pixels
rsd_rad=0.10;                               % set relative standard deviation of radius
std_rad=avg_rad*rsd_rad;
n=50;                                       % set number of particles
radii=randn(n,1)*std_rad+avg_rad;

radii01=radii;                              % define to save
```

Appendix D. MATLAB code for randomly dispersed particles

```
n=50;                                          % set number of particles in simulation
Location_Temp=rand(n,3)*1024;                  % random coordinates from 0 to 1024
Location_Temp(:,3)=radii01;                    % defined by matrix of values or single value

Location_Add=zeros(n,3);                       % remove overlapping particles
count=0;

for i=1:n
        a=Location_Temp(i,1);
        b=Location_Temp(i,2);
        Test=sqrt((a-Location_Temp(:,1)).^2+(b-Location_Temp(:,2)).^2);
        Test(i)=10*average_radius;
        if min(Test-(Location_Temp(i,3)+Location_Temp(:,3)))>=0
                count=count+1;
                Location_Add(count,:)=Location_Temp(i,:);
        end
end

Location_Random_All=Location_Temp;
clear Location_Temp
Location_Temp=Location_Add;
clear Location_Add
Location_Add=Location_Temp(1:count,:);         % remove extra zeros in Location_Add

length(Location_Add)                           % check actual number of particles

LRandom01=Location_Add;                                % define to save
```

Appendix E. MATLAB code for forming clusters

```
Locations=LRandom01;                                % select particle coordinates/radii matrix
image_size=1024;                                    % set simulation image dimension
n=length(Locations(:,1));                           % identify number of particles
k=5;                                                %set number of clusters
PC=n/k                                              % calculate number of particles per cluster

LCluster=zeros(n,3);

for j=1:k
        Loc=Locations((((j-1)*PC)+1):j*PC,:);
        N=length(Loc(:,1));
        LInit=reshape(Loc,3*N,1);
        LFinal=zeros(3*N,1);
        ub=LInit;                                   % set upper bound
        ub(1:2*N)=image_size;
        lb=LInit;                                   % set lower bound
        lb(1:2*N)=0;
        [LFinal,feval,exitflag,output]=fmincon(@myfun,LInit,[],[],[],[],lb,ub,@mycon)
                for i=1:3
                        LocationA(:,i)=LFinal(N*(i-1)+1:i*N);   % reform N-by-3 matrix
                end
        LCluster((((j-1)*PC)+1):j*PC,:)=LocationA;
end

LCluster01=LCluster;                                % define to save
```

Appendix F. MATLAB code for random placement of clusters

```
% generate a matrix with random locations for clusters

cl_rad=50;                                          % define cluster radius in pixels
k=5;                                                % identify number of clusters
Location_Temp=rand(k,3)*(1024-(2*cl_rad))+cl_rad;   % random coordinates, no edges
Location_Temp(:,3)=cl_rad;    % 3rd column: radii

Location_Add=zeros(k,3);                            % remove overlapping clusters
count=0;
for i=1:n
        a=Location_Temp(i,1);
        b=Location_Temp(i,2);
        Test=sqrt((a-Location_Temp(:,1)).^2+(b-Location_Temp(:,2)).^2);
        Test(i)=10*cl_rad;
        if min(Test-(Location_Temp(i,3)+Location_Temp(:,3)))>=0
                count=count+1;
                Location_Add(count,:)=Location_Temp(i,:);
        end
end
Location_Random_All=Location_Temp;
clear Location_Temp
Location_Temp=Location_Add;
clear Location_Add
Location_Add=Location_Temp(1:count,:);          % remove extra zeros in Location_Add
length(Location_Add(:,1))                       % check number of clusters matches k
Location2=Location_Add;
Location2(1:k,1:2)=Location_Add(1:k,1:2)-cl_rad;

% move clusters to defined locations

Loc_Init=LCluster01;                                % select multicluster matrix
k=5;                                                % identify number of clusters
n=length(Loc_Init(:,1));
PC=n/k;

LMove=Location2;                                    % select cluster location matrix
LMClust=zeros(n,3);

for j=1:n
        xmove=min(Loc_Init((((j-1)*PC)+1):j*PC,1))-LMove(j,1);
        ymove=min(Loc_Init((((j-1)*PC)+1):j*PC,2))-LMove(j,2);
```

```
        LMClust((((j-1)*PC)+1):j*PC,1)=Loc_Init((((j-1)*PC)+1):j*PC,1)-xmove;
        LMClust((((j-1)*PC)+1):j*PC,2)=Loc_Init((((j-1)*PC)+1):j*PC,2)-ymove;
        LMClust((((j-1)*PC)+1):j*PC,3)=Loc_Init((((j-1)*PC)+1):j*PC,3);
end

LCluster01R=LMClust;                                        % define to save
```

Appendix G. MATLAB code for coefficient of clustering analysis

```
Locations=image_particles_01;                % select particle coordinates matrix
image_size=1024;                             % indicate side dimension of image
n=length(Locations(:,1))                     % identify number of particles
divisions=5;                                 % select number of divisions per side
C=zeros(divisions, divisions);
section=image_size/divisions;                % calculate side dimension of division

for i=1:n
        ix=ceil(Locations(i,1)/section);     % locate x-coordinate section
        iy=ceil(Locations(i,2)/section);     % locate y-coordinate section
        C(ix,iy)=C(ix,iy)+1;                 % count particle in section
end

Cvector=reshape(C,divisions^2,1);            % convert matrix to single column

CC_01=std(Cvector)^2/mean(Cvector)           % define to save
```

REFERENCES

1. Xue, X.Y., J.F. Stebbins, M. Kanzaki, P.F. McMillan, and B. Poe, *Pressure-Induced Silicon Cooridination and Tetrahedral Structural-Changes in Alkali Oxide-Silica Melts up to 12 GPA - NMR, RAMAN, and Infrared-Spectroscopy.* American Mineralogist, **1991**. 76(1-2): p. 8-26.
2. Stober, W., A. Fink, and E. Bohn, *Controlled Growth of Monodisperse Silica Spheres in Micron Size Range.* Journal of Colloid and Interface Science, **1968**. 26(1): p. 62-&.
3. Kresge, C.T., M.E. Leonowicz, W.J. Roth, J.C. Vartuli, and J.S. Beck, *Ordered Mesoporous Molecular-Sieves Synthesized by a Liquid-Crystal Template Mechanism.* Nature, **1992**. 359(6397): p. 710-712.
4. Zhuravlev, L.T., *The surface chemistry of amorphous silica. Zhuravlev model.* Colloids and Surfaces a-Physicochemical and Engineering Aspects, **2000**. 173(1-3): p. 1-38.
5. Hizal, J. and R. Apak, *Modeling of copper(II) and lead(II) adsorption on kaolinite-based clay minerals individually and in the presence of humic acid.* Journal of Colloid and Interface Science, **2006**. 295(1): p. 1-13.
6. Mueller, P.S., C.P. Parker, and S.C. Larsen, *One-pot synthesis of iron oxide mesoporous silica core/shell nanocomposites.* Microporous and Mesoporous Materials, **2015**. 204: p. 173-179.
7. Vallet-Regi, M., A. Ramila, R.P. del Real, and J. Perez-Pariente, *A New Property of MCM-41: Drug Delivery System.* Chemistry of Materials, **2001**. 13(2): p. 308-311.
8. Slowing, I.I., J.L. Vivero-Escoto, C.W. Wu, and V.S.-Y. Lin, *Mesoporous silica nanoparticles as controlled release drug delivery and gene transfection carriers.* Advanced Drug Delivery Reviews, **2008**. 60(11): p. 1278-1288.
9. Li, Z.X., J.C. Barnes, A. Bosoy, J.F. Stoddart, and J.I. Zink, *Mesoporous silica nanoparticles in biomedical applications.* Chemical Society Reviews, **2012**. 41(7): p. 2590-2605.
10. Zhu, Y.F., J.L. Shi, Y.S. Li, H.R. Chen, W.H. Shen, and X.P. Dong, *Hollow mesoporous spheres with cubic pore network as a potential carrier for drug storage and its in vitro release kinetics.* Journal of Materials Research, **2005**. 20(1): p. 54-61.
11. Gao, L., J.H. Sun, L. Zhang, J.P. Wang, and B. Ren, *Influence of different structured channels of mesoporous silicate on the controlled ibuprofen delivery.* Materials Chemistry and Physics, **2012**. 135(2-3): p. 786-797.
12. Lai, C.Y., B.G. Trewyn, D.M. Jeftinija, K. Jeftinija, S. Xu, S. Jeftinija, and V.S.-Y. Lin, *A mesoporous silica nanosphere-based carrier system with chemically removable CdS nanoparticle caps for stimuli-responsive controlled release of neurotransmitters and drug molecules.* Journal of the American Chemical Society, **2003**. 125(15): p. 4451-4459.

13. Yang, Q., S.H. Wang, P.W. Fan, L.F. Wang, Y. Di, K.F. Lin, and F.S. Xiao, *pH-responsive carrier system based on carboxylic acid modified mesoporous silica and polyelectrolyte for drug delivery.* Chemistry of Materials, **2005**. 17(24): p. 5999-6003.
14. Meng, H.A., M. Xue, T.A. Xia, Y.L. Zhao, F. Tamanoi, J.F. Stoddart, J.I. Zink, and A.E. Nel, *Autonomous in Vitro Anticancer Drug Release from Mesoporous Silica Nanoparticles by pH-Sensitive Nanovalves.* Journal of the American Chemical Society, **2010**. 132(36): p. 12690-12697.
15. Rosenholm, J.M., E. Peuhu, L.T. Bate-Eya, J.E. Eriksson, C. Sahlgren, and M. Linden, *Cancer-Cell-Specific Induction of Apoptosis Using Mesoporous Silica Nanoparticles as Drug-Delivery Vectors.* Small, **2010**. 6(11): p. 1234-1241.
16. Gao, Y., Y. Chen, X.F. Ji, X.Y. He, Q. Yin, Z.W. Zhang, J.L. Shi, and Y.P. Li, *Controlled Intracellular Release of Doxorubicin in Multidrug-Resistant Cancer Cells by Tuning the Shell-Pore Sizes of Mesoporous Silica Nanoparticles.* Acs Nano, **2011**. 5(12): p. 9788-9798.
17. De Jong, W.H. and P.J.A. Borm, *Drug delivery and nanoparticles: Applications and hazards.* International Journal of Nanomedicine, **2008**. 3(2): p. 133-149.
18. Andersson, J., J. Rosenholm, S. Areva, and M. Linden, *Influences of material characteristics on ibuprofen drug loading and release profiles from ordered micro- and mesoporous silica matrices.* Chemistry of Materials, **2004**. 16(21): p. 4160-4167.
19. Bouchoucha, M., M.F. Cote, R. C-Gaudreault, M.A. Fortin, and F. Kleitz, *Size-Controlled Functionalized Mesoporous Silica Nanoparticles for Tunable Drug Release and Enhanced Anti-Tumoral Activity.* Chemistry of Materials, **2016**. 28(12): p. 4243-4258.
20. Song, S.W., K. Hidajat, and S. Kawi, *Functionalized SBA-15 materials as carriers for controlled drug delivery: Influence of surface properties on matrix-drug interactions.* Langmuir, **2005**. 21(21): p. 9568-9575.
21. Guo, R., et al., *Tuning kinetics of controlled-release in disulfide-linked MSN-folate conjugates with different fabrication procedures.* Materials Letters, **2012**. 66(1): p. 79-82.
22. Yuan, L., W.L. Chen, J.H. Hu, J.Z. Zhang, and D. Yang, *Mechanistic Study of the Covalent Loading of Paclitaxel via Disulfide Linkers for Controlled Drug Release.* Langmuir, **2013**. 29(2): p. 734-743.
23. Izquierdo-Barba, I., E. Sousa, J.C. Doadrio, A.L. Doadrio, J.P. Pariente, A. Martinez, F. Babonneau, and M. Vallet-Regi, *Influence of mesoporous structure type on the controlled delivery of drugs: release of ibuprofen from MCM-48, SBA-15 and functionalized SBA-15.* Journal of Sol-Gel Science and Technology, **2009**. 50(3): p. 421-429.
24. Patel, K., B.S. Raj, Y. Chen, and X. Lou, *Cytotoxicity of folic acid conjugated hollow silica nanoparticles toward Caco2 and 3T3 cells, with and without encapsulated DOX.* Colloids and Surfaces B-Biointerfaces, **2016**. 140: p. 213-222.

25. Zhu, Y.F., Y. Fang, and S. Kaskel, *Folate-Conjugated Fe3O4@SiO2 Hollow Mesoporous Spheres for Targeted Anticancer Drug Delivery.* Journal of Physical Chemistry C, **2010**. 114(39): p. 16382-16388.
26. Danhier, F., O. Feron, and V. Preat, *To exploit the tumor microenvironment: Passive and active tumor targeting of nanocarriers for anti-cancer drug delivery.* Journal of Controlled Release, **2010**. 148(2): p. 135-146.
27. Meng, H., M. Xue, T. Xia, Z.X. Ji, D.Y. Tarn, J.I. Zink, and A.E. Nel, *Use of Size and a Copolymer Design Feature To Improve the Biodistribution and the Enhanced Permeability and Retention Effect of Doxorubicin-Loaded Mesoporous Silica Nanoparticles in a Murine Xenograft Tumor Model.* Acs Nano, **2011**. 5(5): p. 4131-4144.
28. Liu, X.L., Y.X. Tao, H.H. Mao, Y. Kong, J. Shen, L.H. Deng, and L.S. Yang, *Construction of magnetic-targeted and NIR irradiation-controlled drug delivery platform with Fe3O4@Au@SiO2 nanospheres.* Ceramics International, **2017**. 43(6): p. 5061-5067.
29. Huang, L., L.J. Ao, D.H. Hu, W. Wang, Z.H. Sheng, and W. Su, *Magneto-Plasmonic Nanocapsules for Multimodal-Imaging and Magnetically Guided Combination Cancer Therapy.* Chemistry of Materials, **2016**. 28(16): p. 5896-5904.
30. Gai, S.L., P.P. Yang, C.X. Li, W.X. Wang, Y.L. Dai, N. Niu, and J. Lin, *Synthesis of Magnetic, Up-Conversion Luminescent, and Mesoporous Core-Shell-Structured Nanocomposites as Drug Carriers.* Advanced Functional Materials, **2010**. 20(7): p. 1166-1172.
31. Bazak, R., M. Houri, S. El Achy, S. Kamel, and T. Refaat, *Cancer active targeting by nanoparticles: a comprehensive review of literature.* Journal of Cancer Research and Clinical Oncology, **2015**. 141(5): p. 769-784.
32. Velikova, N., et al., *Broadening the antibacterial spectrum of histidine kinase autophosphorylation inhibitors via the use of epsilon-poly-L-lysine capped mesoporous silica-based nanoparticles.* Nanomedicine-Nanotechnology Biology and Medicine, **2017**. 13(2): p. 569-581.
33. He, C.B., K.D. Lu, D.M. Liu, and W.B. Lin, *Nanoscale Metal-Organic Frameworks for the Co-Delivery of Cisplatin and Pooled siRNAs to Enhance Therapeutic Efficacy in Drug-Resistant Ovarian Cancer Cells.* Journal of the American Chemical Society, **2014**. 136(14): p. 5181-5184.
34. Manzano, M., V. Aina, C.O. Arean, F. Balas, V. Cauda, M. Colilla, M.R. Delgado, and M. Vallet-Regi, *Studies on MCM-41 mesoporous silica for drug delivery: Effect of particle morphology and amine functionalization.* Chemical Engineering Journal, **2008**. 137(1): p. 30-37.
35. Ferris, D.P., J. Lu, C. Gothard, R. Yanes, C.R. Thomas, J.C. Olsen, J.F. Stoddart, F. Tamanoi, and J.I. Zink, *Synthesis of Biomolecule-Modified Mesoporous Silica Nanoparticles for Targeted Hydrophobic Drug Delivery to Cancer Cells.* Small, **2011**. 7(13): p. 1816-1826.
36. Gan, Q., D.W. Dai, Y. Yuan, J.C. Qian, S. Sha, J.L. Shi, and C.S. Liu, *Effect of size on the cellular endocytosis and controlled release of mesoporous silica nanoparticles for intracellular delivery.* Biomedical Microdevices, **2012**. 14(2): p. 259-270.

37. Lu, F., S.H. Wu, Y. Hung, and C.Y. Mou, *Size Effect on Cell Uptake in Well-Suspended, Uniform Mesoporous Silica Nanoparticles.* Small, **2009**. 5(12): p. 1408-1413.
38. Wu, W., C.Y. Ye, H. Xiao, X.W. Sun, W.H. Qu, X.H. Li, M. Chen, and J.S. Li, *Hierarchical mesoporous silica nanoparticles for tailorable drug release.* International Journal of Pharmaceutics, **2016**. 511(1): p. 65-72.
39. Horcajada, P., A. Ramila, J. Perez-Pariente, and M. Vallet-Regi, *Influence of pore size of MCM-41 matrices on drug delivery rate.* Microporous and Mesoporous Materials, **2004**. 68(1-3): p. 105-109.
40. Knezevic, N.Z., I.I. Slowing, and V.S.-Y. Lin, *Tuning the Release of Anticancer Drugs from Magnetic Iron Oxide/Mesoporous Silica Core/Shell Nanoparticles.* Chempluschem, **2012**. 77(1): p. 48-55.
41. Souza, K.C., J.D. Ardisson, and E.M.B. Sousa, *Study of mesoporous silica/magnetite systems in drug controlled release.* Journal of Materials Science-Materials in Medicine, **2009**. 20(2): p. 507-512.
42. Ruiz-Hernandez, E., A. Baeza, and M. Vallet-Regi, *Smart Drug Delivery through DNA/Magnetic Nanoparticle Gates.* Acs Nano, **2011**. 5(2): p. 1259-1266.
43. Thomas, C.R., D.P. Ferris, J.H. Lee, E. Choi, M.H. Cho, E.S. Kim, J.F. Stoddart, J.S. Shin, J. Cheon, and J.I. Zink, *Noninvasive Remote-Controlled Release of Drug Molecules in Vitro Using Magnetic Actuation of Mechanized Nanoparticles.* Journal of the American Chemical Society, **2010**. 132(31): p. 10623-10625.
44. Baeza, A., E. Guisasola, E. Ruiz-Hernandez, and M. Vallet-Regi, *Magnetically Triggered Multidrug Release by Hybrid Mesoporous Silica Nanoparticles.* Chemistry of Materials, **2012**. 24(3): p. 517-524.
45. Tao, C.L. and Y.F. Zhu, *Magnetic mesoporous silica nanoparticles for potential delivery of chemotherapeutic drugs and hyperthermia.* Dalton Transactions, **2014**. 43(41): p. 15482-15490.
46. Wydra, R.J., P.G. Rychahou, B.M. Evers, K.W. Anderson, T.D. Dziubla, and J.Z. Hilt, *The role of ROS generation from magnetic nanoparticles in an alternating magnetic field on cytotoxicity.* Acta Biomaterialia, **2015**. 25: p. 284-290.
47. Knezevic, N.Z. and J.O. Durand, *Targeted Treatment of Cancer with Nanotherapeutics Based on Mesoporous Silica Nanoparticles.* Chempluschem, **2015**. 80(1): p. 26-36.
48. Hurley, K.R., et al., *Predictable Heating and Positive MRI Contrast from a Mesoporous Silica-Coated Iron Oxide Nanoparticle.* Molecular Pharmaceutics, **2016**. 13(7): p. 2172-2183.
49. Li, J.G., H. Jiang, Z.Q. Yu, H.Y. Xia, G. Zou, Q.J. Zhang, and Y. Yu, *Multifunctional Uniform Core-Shell Fe3O4@mSiO2 Mesoporous Nanoparticles for Bimodal Imaging and Photothermal Therapy.* Chemistry-an Asian Journal, **2013**. 8(2): p. 385-391.
50. Yang, Y., Q.F. Guo, J.R. Peng, J. Su, X.L. Lu, Y.X. Zhao, and Z.Y. Qian, *Doxorubicin-Conjugated Heparin-Coated Superparamagnetic Iron Oxide Nanoparticles for Combined Anticancer Drug Delivery and Magnetic Resonance Imaging.* Journal of Biomedical Nanotechnology, **2016**. 12(11): p. 1963-1974.

51. Chen, W.H., et al., *Rational design of multifunctional magnetic mesoporous silica nanoparticle for tumor-targeted magnetic resonance imaging and precise therapy.* Biomaterials, **2016**. 76: p. 87-101.
52. Bhattacharjee, S. and D.J. Brayden, *Development of nanotoxicology: implications for drug delivery and medical devices.* Nanomedicine, **2015**. 10(14): p. 2289-2305.
53. Fadeel, B. and A.E. Garcia-Bennett, *Better safe than sorry: Understanding the toxicological properties of inorganic nanoparticles manufactured for biomedical applications.* Advanced Drug Delivery Reviews, **2010**. 62(3): p. 362-374.
54. Hudson, S.P., R.F. Padera, R. Langer, and D.S. Kohane, *The biocompatibility of mesoporous silicates.* Biomaterials, **2008**. 29(30): p. 4045-4055.
55. Frohlich, E., *Value of phagocyte function screening for immunotoxicity of nanoparticles in vivo.* International Journal of Nanomedicine, **2015**. 10: p. 3761-3778.
56. Lehman, S.E., A.S. Morris, P.S. Mueller, A.K. Salem, V.H. Grassian, and S.C. Larsen, *Silica nanoparticle-generated ROS as a predictor of cellular toxicity: mechanistic insights and safety by design.* Environmental Science-Nano, **2016**. 3(1): p. 56-66.
57. Bollu, V.S., A.K. Barui, S.K. Mondal, S. Prashar, M. Fajardo, D. Briones, A. Rodriguez-Dieguez, C.R. Patra, and S. Gomez-Ruiz, *Curcumin-loaded silica-based mesoporous materials: Synthesis, characterization and cytotoxic properties against cancer cells.* Materials Science & Engineering C-Materials for Biological Applications, **2016**. 63: p. 393-410.
58. Oberdorster, G., E. Oberdorster, and J. Oberdorster, *Nanotoxicology: An emerging discipline evolving from studies of ultrafine particles.* Environmental Health Perspectives, **2005**. 113(7): p. 823-839.
59. Wyss, P.P., L.C. Herrera, N.S. Bouteghmes, M. Sarem, W. Reichardt, J. Leupold, J. Hennig, and V.P. Shastri, *Nanoprobes for Multimodal Visualization of Bone Mineral Phase in Magnetic Resonance and Near-Infrared Optical Imaging.* Acs Omega, **2016**. 1(2): p. 182-192.
60. Zhu, J., L. Liao, L.N. Zhu, P. Zhang, K. Guo, J.L. Kong, C. Ji, and B.H. Liu, *Size-dependent cellular uptake efficiency, mechanism, and cytotoxicity of silica nanoparticles toward HeLa cells.* Talanta, **2013**. 107: p. 408-415.
61. Mo, J.B., L.Z. He, B. Ma, and T.F. Chen, *Tailoring Particle Size of Mesoporous Silica Nanosystem To Antagonize Glioblastoma and Overcome Blood-Brain Barrier.* Acs Applied Materials & Interfaces, **2016**. 8(11): p. 6811-6825.
62. Knezevic, N.Z., E. Ruiz-Hernandez, W.E. Hennink, and M. Vallet-Regi, *Magnetic mesoporous silica-based core/shell nanoparticles for biomedical applications.* Rsc Advances, **2013**. 3(25): p. 9584-9593.
63. Moller, K., J. Kobler, and T. Bein, *Colloidal suspensions of nanometer-sized mesoporous silica.* Advanced Functional Materials, **2007**. 17(4): p. 605-612.
64. Egodawatte, S., A. Datt, E.A. Burns, and S.C. Larsen, *Chemical Insight into the Adsorption of Chromium(III) on Iron Oxide/Mesoporous Silica Nanocomposites.* Langmuir, **2015**. 31(27): p. 7553-7562.

65. Deng, Y., D. Qi, C. Deng, X. Zhang, and D. Zhao, *Superparamagnetic high-magnetization microspheres with an Fe3O4@SiO2 core and perpendicularly aligned mesoporous SiO2 shell for removal of microcystins.* Journal of the American Chemical Society, **2008**. 130(1): p. 28-29.
66. Meng, H.A., M. Liong, T.A. Xia, Z.X. Li, Z.X. Ji, J.I. Zink, and A.E. Nel, *Engineered Design of Mesoporous Silica Nanoparticles to Deliver Doxorubicin and P-Glycoprotein siRNA to Overcome Drug Resistance in a Cancer Cell Line.* Acs Nano, **2010**. 4(8): p. 4539-4550.
67. Climent, E., A. Bernardos, R. Martinez-Manez, A. Maquieira, M.D. Marcos, N. Pastor-Navarro, R. Puchades, F. Sancenon, J. Soto, and P. Amoros, *Controlled Delivery Systems Using Antibody-Capped Mesoporous Nanocontainers.* Journal of the American Chemical Society, **2009**. 131(39): p. 14075-14080.
68. Knezevic, N.Z. and V.S.-Y. Lin, *A magnetic mesoporous silica nanoparticle-based drug delivery system for photosensitive cooperative treatment of cancer with a mesopore-capping agent and mesopore-loaded drug.* Nanoscale, **2013**. 5(4): p. 1544-1551.
69. Mishra, A.K., H. Pandey, V. Agarwal, P.W. Ramteke, and A.C. Pandey, *Nanoengineered mesoporous silica nanoparticles for smart delivery of doxorubicin.* Journal of Nanoparticle Research, **2014**. 16(8): p. 10.
70. Izquierdo-Barba, I., A. Martinez, A.L. Doadrio, J. Perez-Pariente, and M. Vallet-Regi, *Release evaluation of drugs from ordered three-dimensional silica structures.* European Journal of Pharmaceutical Sciences, **2005**. 26(5): p. 365-373.
71. Ishii, H., T. Ikuno, A. Shimojima, and T. Okubo, *Preparation of core-shell mesoporous silica nanoparticles with bimodal pore structures by regrowth method.* Journal of Colloid and Interface Science, **2015**. 448: p. 57-64.
72. Limnell, T., H.A. Santos, E. Makila, T. Heikkila, J. Salonen, D.Y. Murzin, N. Kumar, T. Laaksonen, L. Peltonen, and J. Hirvonen, *Delivery Formulations of Ordered and Nonordered Mesoporous Silica: Comparison of Three Drug Loading Methods.* Journal of Pharmaceutical Sciences, **2011**. 100(8): p. 3294-3306.
73. Fossati, R., C. Confalonieri, V. Torri, E. Ghislandi, A. Penna, V. Pistotti, A. Tinazzi, and A. Liberati, *Cytotoxic and hormonal treatment for metastatic breast cancer: A systematic review of published randomized trials involving 31,510 women.* Journal of Clinical Oncology, **1998**. 16(10): p. 3439-3460.
74. Kaushik, D. and G. Bansal, *Four new degradation products of doxorubicin: An application of forced degradation study and hyphenated chromatographic techniques.* J. Pharm. Anal., **2015**. 5: p. 285-295.
75. Korsmeyer, R.W. and N.A. Peppas, *Effect of the Morphology of Hydrophilic Polymeric Matrices on the Diffusion and Release of Water-Soluble Drugs.* Journal of Membrane Science, **1981**. 9(3): p. 211-227.
76. Costa, P., J. Manuel, and S. Lobo, *Modeling and comparison of dissolution profiles.* European Journal of Pharmaceutical Sciences, **2001**. 13(2): p. 123-133.

77. Papadopoulou, V., K. Kosmidis, M. Vlachou, and P. Macheras, *On the use of the Weibull function for the discernment of drug release mechanisms.* International Journal of Pharmaceutics, **2006**. 309(1-2): p. 44-50.
78. Daryasari, M.P., M.R. Akhgar, F. Mamashli, B. Bigdeli, and M. Khoobi, *Chitosan-folate coated mesoporous silica nanoparticles as a smart and pH-sensitive system for curcumin delivery.* Rsc Advances, **2016**. 6(107): p. 105578-105588.
79. Ritger, P.L. and N.A. Peppas, *A simple equation for description of solute release I. Fickian and non-fickian release from non-swellable devices in the form of slabs, spheres, cylinders or discs.* Journal of Controlled Release, **1987**. 5(1): p. 23-36.
80. Sundar, D.S., M.G. Antoniraj, C.S. Kumar, S.S. Mohapatra, N.N. Houreld, and K. Ruckmani, *Recent Trends of Biocompatible and Biodegradable Nanoparticles in Drug Delivery: A Review.* Current Medicinal Chemistry, **2016**. 23(32): p. 3730-3751.
81. Mamaeva, V., C. Sahlgren, and M. Linden, *Mesoporous silica nanoparticles in medicine-Recent advances.* Advanced Drug Delivery Reviews, **2013**. 65(5): p. 689-702.
82. Sun, T.M., Y.S. Zhang, B. Pang, D.C. Hyun, M.X. Yang, and Y.N. Xia, *Engineered Nanoparticles for Drug Delivery in Cancer Therapy.* Angewandte Chemie-International Edition, **2014**. 53(46): p. 12320-12364.
83. Guidi, P., M. Nigro, M. Bernardeschi, V. Scarcelli, P. Lucchesi, B. Onida, R. Mortera, and G. Frenzilli, *Genotoxicity of amorphous silica particles with different structure and dimension in human and murine cell lines.* Mutagenesis, **2013**. 28(2): p. 171-180.
84. Roggen, E.L., N.K. Soni, and G.R. Verheyen, *Respiratory immunotoxicity: An in vitro assessment.* Toxicology in Vitro, **2006**. 20(8): p. 1249-1264.
85. Xu, J., B.C. Zhang, X.L. Li, W.H. Xu, J. Zhou, L. Shen, and Q.C. Wei, *Chemosensitization and Radiosensitization of a Lung Cancer Cell Line A549 Induced by a Composite Polymer Micelle.* Discovery Medicine, **2016**. 22(119): p. 7-17.
86. Yin, P.H., X. Liu, Y.Y. Qiu, J.F. Cai, J.M. Qin, H.R. Zhu, and Q. Li, *Anti-tumor Activity and Apoptosis-regulation Mechanisms of Bufalin in Various Cancers: New Hope for Cancer Patients.* Asian Pacific Journal of Cancer Prevention, **2012**. 13(11): p. 5339-5343.
87. Albitar, L., G. Pickett, M. Morgan, S. Davies, and K.K. Leslie, *Models representing type I and type II human endometrial cancers: Ishikawa H and Hec50co cells.* Gynecologic Oncology, **2007**. 106(1): p. 52-64.
88. Dai, D., D.M. Wolf, E.S. Litman, M.J. White, and K.K. Leslie, *Progesterone inhibits human endometrial cancer cell growth and invasiveness: Down-regulation of cellular adhesion molecules through progesterone B receptors.* Cancer Research, **2002**. 62(3): p. 881-886.
89. O'Neal, D.P., L.R. Hirsch, N.J. Halas, J.D. Payne, and J.L. West, *Photo-thermal tumor ablation in mice using near infrared-absorbing nanoparticles.* Cancer Letters, **2004**. 209(2): p. 171-176.

90. Tesniere, A., et al., *Immunogenic death of colon cancer cells treated with oxaliplatin.* Oncogene, **2010**. 29(4): p. 482-491.
91. He, Y.J., Z.G. Su, L.J. Xue, H. Xu, and C. Zhang, *Co-delivery of erlotinib and doxorubicin by pH-sensitive charge conversion nanocarrier for synergistic therapy.* Journal of Controlled Release, **2016**. 229: p. 80-92.
92. Shen, S., H.Y. Tang, X.T. Zhang, J.F. Ren, Z.Q. Pang, D.G. Wang, H.L. Gao, Y. Qian, X.G. Jiang, and W.L. Yang, *Targeting mesoporous silica-encapsulated gold nanorods for chemo-photothermal therapy with near-infrared radiation.* Biomaterials, **2013**. 34(12): p. 3150-3158.
93. Jang, M.K., Y.I. Jeong, and J.W. Nah, *Characterization and preparation of core-shell type nanoparticle for encapsulation of anticancer drug.* Colloids and Surfaces B-Biointerfaces, **2010**. 81(2): p. 530-536.
94. Huang, S.S., Y. Fan, Z.Y. Cheng, D.Y. Kong, P.P. Yang, Z.W. Quan, C.M. Zhang, and J. Lin, *Magnetic Mesoporous Silica Spheres for Drug Targeting and Controlled Release.* Journal of Physical Chemistry C, **2009**. 113(5): p. 1775-1784.
95. Wang, C.L., J.T. Yan, X.J. Cui, and H.Y. Wang, *Synthesis of raspberry-like monodisperse magnetic hollow hybrid nanospheres by coating polystyrene template with Fe3O4@SiO2 particles.* Journal of Colloid and Interface Science, **2011**. 354(1): p. 94-99.
96. Souto, G.D., Z. Farhane, A. Casey, E. Efeoglu, J. McIntyre, and H.J. Byrne, *Evaluation of cytotoxicity profile and intracellular localisation of doxorubicin-loaded chitosan nanoparticles.* Analytical and Bioanalytical Chemistry, **2016**. 408(20): p. 5443-5455.
97. Wu, L., H.J. Zhang, M.H. Wu, Y.F. Zhong, X.W. Liu, and Z. Jiao, *Dual-templating synthesis of multi-shelled mesoporous silica nanoparticles as catalyst and drug carrier.* Microporous and Mesoporous Materials, **2016**. 228: p. 318-328.
98. Kuo, C.Y., et al., *Magnetically triggered nanovehicles for controlled drug release as a colorectal cancer therapy.* Colloids and Surfaces B-Biointerfaces, **2016**. 140: p. 567-573.
99. Lee, M.H., E.J. Kim, H. Lee, H.M. Kim, M.J. Chang, S.Y. Park, K.S. Hong, J.S. Kim, and J.L. Sessler, *Liposomal Texaphyrin Theranostics for Metastatic Liver Cancer.* Journal of the American Chemical Society, **2016**. 138(50): p. 16380-16387.
100. Chen, Y., H.R. Chen, D.P. Zeng, Y.B. Tian, F. Chen, J.W. Feng, and J.L. Shi, *Core/Shell Structured Hollow Mesoporous Nanocapsules: A Potential Platform for Simultaneous Cell Imaging and Anticancer Drug Delivery.* Acs Nano, **2010**. 4(10): p. 6001-6013.
101. Zhu, Y.F., T. Ikoma, N. Hanagata, and S. Kaskel, *Rattle-Type Fe3O4@SiO2 Hollow Mesoporous Spheres as Carriers for Drug Delivery.* Small, **2010**. 6(3): p. 471-478.
102. Page, L., S. Maswadi, and R.D. Glickman, *Optoacoustic Multispectral Imaging of Radiolucent Foreign Bodies in Tissue.* Applied Spectroscopy, **2013**. 67(1): p. 22-28.
103. Skvortsova, Y.A., R.M. Freeney, Z.M. Zhong, and M.L. Geng, *Tissue Phantoms Constructed with Hydrophobic Nanoporous Silica Particles.* Analytical Chemistry, **2010**. 82(15): p. 6712-6716.

104. Sordillo, D.C., Y. Budansky, P.P. Sordillo, L.A. Sordillo, and R. Alfano, *A Novel Approach to Paget's Disease Diagnosis and Monitoring using Near-Infrared Absorption Spectroscopy*, in *Photonic Therapeutics and Diagnostics Ix*, N. Kollias, et al., Editors. 2013, Spie-Int Soc Optical Engineering: Bellingham.
105. Staring, M., M.E. Bakker, J. Stolk, D.P. Shamonin, J.H.C. Reiber, and B.C. Stoel, *Towards local progression estimation of pulmonary emphysema using CT.* Medical Physics, **2014**. 41(2): p. 13.
106. Sujatha, N., B.S.S. Anand, K.B. Nivetha, V.B. Narayanamurthy, V. Seshadri, and R. Poddar, *Assessment of Microcirculatory Hemoglobin Levels in Normal and Diabetic Subjects using Diffuse Reflectance Spectroscopy in the Visible Region - a Pilot Study.* Journal of Applied Spectroscopy, **2015**. 82(3): p. 432-437.
107. Zhou, F.L., P.L. Hubbard, S.J. Eichhorn, and G.J.M. Parker, *Coaxially Electrospun Axon-Mimicking Fibers for Diffusion Magnetic Resonance Imaging.* Acs Applied Materials & Interfaces, **2012**. 4(11): p. 6311-6316.
108. Kong, R., R.K. Reddy, and R. Bhargava, *Characterization of tumor progression in engineered tissue using infrared spectroscopic imaging.* Analyst, **2010**. 135(7): p. 1569-1578.
109. Skvortsova, Y., G.F. Wang, and M.L. Geng, *Statistical two-dimensional correlation coefficient mapping of simulated tissue phantom data: Boundary determination in tissue classification for cancer diagnosis.* Journal of Molecular Structure, **2006**. 799(1-3): p. 239-246.
110. Skala, M.C., K.M. Riching, A. Gendron-Fitzpatrick, J. Eickhoff, K.W. Eliceiri, J.G. White, and N. Ramanujam, *In vivo multiphoton microscopy of NADH and FAD redox states, fluorescence lifetimes, and cellular morphology in precancerous epithelia.* Proceedings of the National Academy of Sciences of the United States of America, **2007**. 104(49): p. 19494-19499.
111. Huang, S.H., A.A. Heikal, and W.W. Webb, *Two-photon fluorescence spectroscopy and microscopy of NAD(P)H and flavoprotein.* Biophysical Journal, **2002**. 82(5): p. 2811-2825.
112. Masters, B.R., P.T.C. So, and E. Gratton, *Multiphoton excitation fluorescence microscopy and spectroscopy of in vivo human skin.* Biophysical Journal, **1997**. 72(6): p. 2405-2412.
113. Brumaru, C.S., *I. Hydrophobic nanoporous silica particles for biomedical applications. II. Novel approaches to two dimensional correlation spectroscopy.* PhD (Doctor of Philosophy) thesis, University of Iowa, **2013.** http://ir.uiowa.edu/etd/2446.
114. Lowry, M.A., *Studies of Capillary Electrochromatography and Retention in Reversed-Phase Chromatographic Stationary Phases Using Confocal Fluorescence Microscopy.* PhD (Doctor of Philosophy) thesis, University of Iowa, **2005.** **ProQuest Dissertations Publishing, 3172415**.
115. Fork, R.L. and Z. Kaplan, *Increased Resistance to Photodegradation of Rhodamine 6G in Cooled Solid Matrices.* Applied Physics Letters, **1972**. 20(12): p. 472-&.
116. Rosenthal, I., *Photo-Chemical Stability of Rhodamine 6G in Solution.* Optics Communications, **1978**. 24(2): p. 164-166.

117. Zehentbauer, F.M., C. Moretto, R. Stephen, T. Thevar, J.R. Gilchrist, D. Pokrajac, K.L. Richard, and J. Kiefer, *Fluorescence spectroscopy of Rhodamine 6G: Concentration and solvent effects.* Spectrochimica Acta Part a-Molecular and Biomolecular Spectroscopy, **2014**. 121: p. 147-151.
118. Skvortsova, Y.A., *Simulation of tissues for biomedical applications.* PhD (Doctor of Philosophy) thesis, University of Iowa, **2009.** http://ir.uiowa.edu/etd/436.
119. Murano, E., R. Toffanin, F. Zanetti, S.H. Knutsen, S. Paoletti, and R. Rizzo, *Chemical and Macromolecular Characterization of Agar Polymers from Gracilaria-Dura (C-Agardh) J-Agardh (Gracilariaceae, Rhodophyta).* Carbohydrate Polymers, **1992**. 18(3): p. 171-178.
120. Matsuhiro, B. and C.C. Urzua, *Agars From Chilean Gelidiaceae.* Hydrobiologia, **1991**. 221: p. 149-156.
121. Brumaru, C. and M.L. Geng, *Interaction of Surfactants with Hydrophobic Surfaces in Nanopores.* Langmuir, **2010**. 26(24): p. 19091-19099.
122. Wang, C., S.Y. Tao, W. Wei, C.G. Meng, F.Y. Liu, and M. Han, *Multifunctional mesoporous material for detection, adsorption and removal of Hg2+ in aqueous solution.* Journal of Materials Chemistry, **2010**. 20(22): p. 4635-4641.
123. Moorthy, M.S., H.B. Kim, J.H. Bae, S.H. Kim, and C.S. Ha, *Design of core-shell magnetic mesoporous silica hybrids for pH and UV light stimuli-responsive cargo release.* Rsc Advances, **2016**. 6(35): p. 29106-29115.
124. Zhang, Q., C.N. Shen, N. Zhao, and F.J. Xu, *Redox-Responsive and Drug-Embedded Silica Nanoparticles with Unique Self-Destruction Features for Efficient Gene/Drug Codelivery.* Advanced Functional Materials, **2017**. 27(10): p. 12.
125. Song, J.C., F.F. Xue, X.X. Zhang, Z.Y. Lu, and Z.Y. Sun, *Synthesis of yolk-shell mesoporous silica nanoparticles via a facile one-pot approach.* Chemical Communications, **2017**. 53(26): p. 3761-3764.
126. Zheng, H.Q., C.W. Tai, J. Su, X.D. Zou, and F.F. Gao, *Ultra-small mesoporous silica nanoparticles as efficient carriers for pH responsive releases of anti-cancer drugs.* Dalton Transactions, **2015**. 44(46): p. 20186-20192.